Microresonator frequency combs and crystals of light

Fan, Zhiwei

Award date:
2023

Awarding institution:
University of Bath

Microresonator frequency combs and crystals of light

Zhiwei Fan

Supervisor: Prof. Dmitry V Skryabin

Department of Physics
University of Bath

This dissertation is submitted for the degree of
Doctor of Philosophy

Bath, United Kingdom November 2022

Declaration

I hereby declare that all the contents are original except where specific reference is made to the work of others. Besides, the thesis has not been submitted in whole or in part for consideration for any other degree or qualification in this, or any other university.

Zhiwei Fan
November 2022

Acknowledgements

I am indebted to my supervisor, Prof Dmitry V Skryabin, for his guidance on my research, the training on my presentation skills and financial support which helped me focus on science. The accomplishment of this degree within three years cannot be separated from his prompt suggestions showing me the right route. With the help of Dmitry, I have broadened my academic horizon and interests through collaborations with European and American groups. Again, I genuinely appreciate his inspiration and support.

University of bath locates in the city of Bath in southwest England embraced by historical sites and gifted musicians. The graceful melody across the town enriched my life during the tough pandemic period. I am grateful for the joyful moments working with colleagues, Dr Danila Puzyrev, Dr Alberto Villois and Vladislav Pankratov. They helped me in many aspects, especially in program optimisation.

I acknowledge the group at the University of Freiburg supervised by Dr Ingo Breunig. During my secondment, I was lucky to work and try a lot of things in different laboratories. I have to admit this was a marvellous journey. In particular, appreciations go to Nicolas Amiune for the experimental training, and also to Dr Yannick Minet and Dr Jan Szabados for the interesting talks.

I would like to thank Ms Joanna Lucyszyn, the Marie Curie project coordinator, who guided me on the administrative rules and travel notices over the pandemic period. I am also indebted to all the members of the Microcomb community, and I wish you all good luck and success.

Most importantly, I sincerely appreciate my family: father- Rui Fan, mother- Zhijing Hu, grandma- Hongzhi Wang, and my young brother- Zhijing Fan for their love, support, and understanding and for always being my side in the tough moments. Last but not least, my heartfelt gratitude goes to Dr Shiyue Liu for her encouragement and support over the past years and also in the foreseen future.

Abstract

Microresonators, with highly compact size, strong nonlinearity and the ability to tailor the dispersion, have attracted great attention in the last decade. Microresonator-based frequency combs (microcombs) have accelerated the progress in the next-generation applications, including range sensing, quantum commutation, spectroscopy, etc. The ring structure limits the light circulating in the cavity to the resonant frequencies. The microcombs, resulting from the cascaded frequency conversions, are generated with the dual balances between nonlinearity and dispersion, as well as the gain and loss. This thesis starts with an overview of the frequency comb development and mechanism. We then report our theoretical studies of the microcomb generation and manipulation under different setups and materials. The first study focuses on the bidirectional Kerr microresonators under the high-finesse condition. It gives an averaged model with the reshaped nonlinearity dominating the microresonator detuning. Such impact on the effective detuning accounts for some interesting phenomena such as bright-dark resonances and soliton blockade. In addition, we have extended the Arnold tongue instability theory of unidirectional microresonator into the two-component case.

Observations of the soliton crystals in the above study have raised our interest and we report the topological band can be formed through the periodic sequence of dissipative Kerr solitons rotating in a ring microresonator. The soliton arrangement is like the well-known one-dimensional Sú-Schrieffer-Heeger (SSH) lattice, where the relative positioning of solitons forms the weak and strong bound pairs in a unit cell through dispersive waves. Using the Bloch theorem, we report the soliton metacrystals band structure and its topological properties. The non-trivial topology has been identified through the geometric phases flip (π step transition), the Wannier function distribution and the corresponding edge states by introducing proper defects. The chirality, induced by breaking the mirror symmetry of the crystal arrangements in the microresonator, leads to the optical frequency combs resembling butterfly-wing-like patterns.

Aside from the discussions on microcomb generations in $\chi^{(3)}$ medium, in the third topic, we expand discussions for the $\chi^{(2)}$ resonators whose merits include but are not limited to the stronger nonlinear strength and the ability to convert lights from near-IR to mid-IR

range. The phase-matched half-harmonic frequency comb at mid-IR is achieved through optical parametric oscillations (OPO). We demonstrate the ordinary and staggered spectrum patterns, where the latter spectra have been the first experimental evidence observed by our collaborators. Another significant numerical observation obtained from our numerous simulations is the soliton comb generation in the mid-IR range, with remarkable stability and bandwidth spanning over 70 free spectral ranges (FSRs).

Table of contents

List of figures

Chapter 1

Introduction

1.1 Frequency comb

Optical frequency combs operate as spectral rulers for ultrafast-process measurements. A significant application is to accurately define one second through measurements of the optical transitions in atoms with well-defined energy levels. ^{133}Cs microwave clock was first developed by L. Essen and J. Parry in 1955 at National Physical Laboratory (UK) and redefined the SI second as 9,192,631,770 oscillations between two hyperfine ground states of caesium [1]. Since the higher frequency of the transitions has a finer structure in the time discretization, the strontium-based atomic clock improved the time precision to 16 digits and the recent optical clock network system presented the ultra-high precision measurements serving as a state-of-the-art technique for probing the quantum systems [2, 3] . The challenges arise from the extreme detections of optical transitions in the order of hundreds THz which is largely beyond the most advanced detection range of electronic scope at the GHz level. Using frequency chain [4] to link such regimes as considered in the last 70s is not convenient due to the complexity until the emergence of frequency combs which serve as an optical gear bridging the radio and optical frequencies elegantly and practically [5].

An optical frequency comb is well known as the train of pulses emitted from a mode-locked laser. In the time domain, as displayed in Fig.1.1, the envelopes of each pulse are propagating in the group velocity with time spacing τ between two neighbouring pulses. It defines the repetition rate:

$$\omega_r = \frac{2\pi}{\tau} \tag{1.1}$$

Though the envelopes repeat in time, the actual fields are not due to the offset between the phase and group velocities, resulting in the carrier-envelope phase offset $\varphi_{ceo}(t)$. The sketch in Fig.1.1 shows the pulse on the right side has the phase accumulation $\Delta\varphi$. Globally, it leads

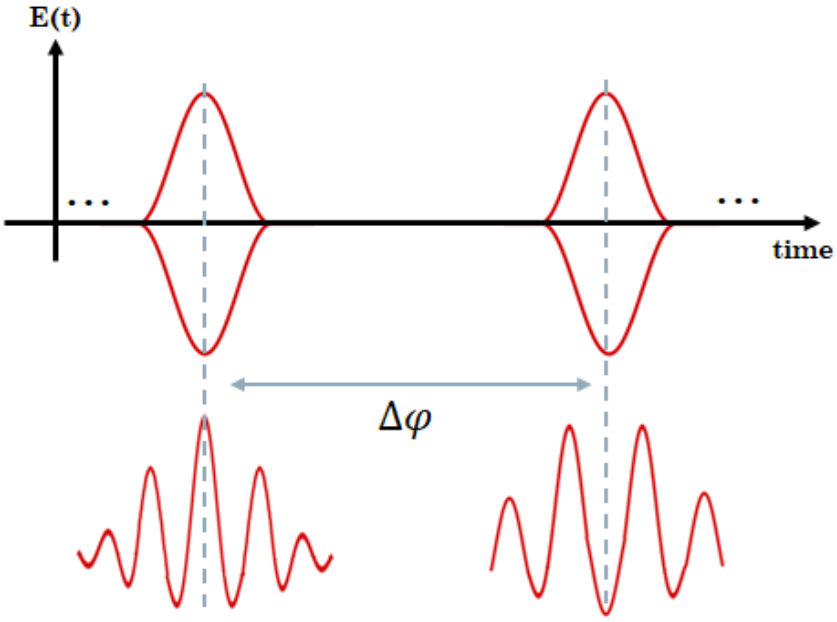

Fig. 1.1 The sketch shows the carrier-envelope offset induced by the phase and group velocity difference. The envelopes in the top row are reproduced over time, with phase difference $\Delta\varphi$ between two adjacent fields shown at the bottom.

to the offset frequency ω_o:

$$\omega_o = \frac{d\varphi_{ceo}(t)}{dt} \tag{1.2}$$

Fig.1.2 presents a typical comb structure in the spectral domain of the pulses emitted from a mode-locked laser. The frequency of each mode is determined by the longitudinal mode index n and the offset frequency ω_o. The measurement of ω_o is usually achieved by self-referencing for an octave-spanned spectrum [6–8]. The computation is based on the beatnote between two selected modes in the spectrum: mode n with frequency $n\omega_r + \omega_o$ is doubled in a periodically poled lithium niobate crystal (PPLN) and beats with the mode $2n$ at frequency $2n\omega_r + \omega_o$. Similarly, the repetition rate ω_r can be measured from the beatnote between adjacent modes n and $n \pm 1$.

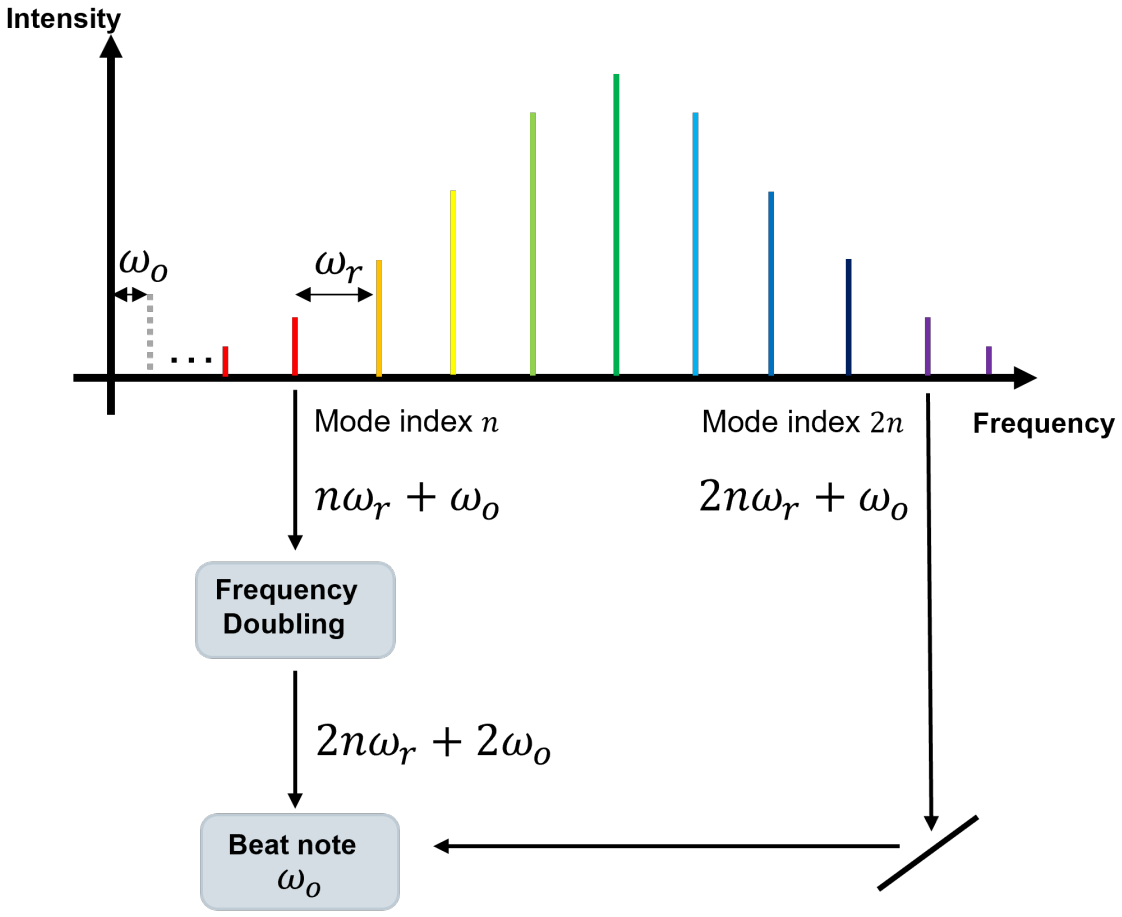

Fig. 1.2 The sketch of self-referencing. The colourful frequency comb is the frequency representation of the train of pulses emitted from a mode-locked laser. The spacing of two adjacent modes is ω_r. Mode index n and $2n$ at the left and right sides within the frequency comb are selected. The mode from the red wing is doubled through a nonlinear crystal and beating with the higher one to measure ω_o.

1.2 Microresonator-based Kerr optical frequency combs

Beyond the great merit in counting the frequencies in the challenging scope, the frequency combs have been demonstrated to embrace a wide range of solid applications in highly integrated circuits. Comb generation from the mode-locked laser is restricted to its comparatively large footprint, namely, it is challenging for integration and portable applications. In 2007, P. Del'Haye and colleagues demonstrated the frequency comb generation from the ultra-high-Q monolithic microresonator [9]. The 75μm-diameter silica toroidal microcavity on a silicon chip pumped at 1550 nm can possess a long photon storage time with the quality factor $Q > 10^8$. Due to the small spatial mode confined by the structure, such microresonators

only require a low power threshold to trigger the nonlinear optical processes. Ref [10] reported the threshold of 50 μW for the onset of the parametric frequency conversion. The cascaded nonlinear process in a microresonator made of typical centre-symmetric material (for example, silica) is illustrated in Fig.1.3. While the resonator is pumped by a CW source, the third-order nonlinearity enables two photons at pump frequency to split into two sideband photons with higher and lower energies in the course of degenerate four-wave mixing as pictured in Fig.1.3 (b). The newly generated modes trigger the non-degenerate process, which leads to the subsequent cascaded frequency conversions. One of the main ongoing challenges of the chip-based microcombs is that the output comb power is relatively low. As the soliton combs exist in the red-detuned regime, most pump powers pass through the waveguide instead of coupling into the resonator. Recent studies shed light on overcoming this challenge using different methods. For example, the group at EPFL demonstrated that a photonic integrated circuit based on an erbium amplifier could increase 100-fold the output power of soliton microcombs [11], and colleagues at Chalmers utilised an auxiliary ring to improve the efficiency [12]. Besides, by pumping the resonator with dual sources, the symmetry breaking of clockwise and counter-clockwise fields in a bidirectional resonator contributes to the next-generation optical devices, like, the nonlinear optical gyroscope and dual-comb spectroscopy, especially for the integrated photonic circuits owing to the high sensitivity in nonlinear responses. Beyond the formation of frequency combs, the study of positioning of Kerr solitons inside a microresonator has been an interesting topic, in particular, the perfect soliton crystals provide an enhanced intensity of the excited modes and a wider spectrum. We have conjectured and confirmed that the train of solitons arranged with certain periodicities in a microresonator can be taken as a Spatio-temporal topological metacrystal, and we intend to motivate the interdisciplinary topics of topological and ultrafast physics [13].

Lugiato-Lefever equation (LLE) [14] was first developed in 1987 and the microresonator system is an active topic where the longitudinal LLE formalism can be applied. It has been demonstrated to be an experienced map for the dissipative solitons generation and Turing pattern formation [15–24]. The general form of LLE in the unidirectional microresonator can be written as [25]:

$$i\partial_t \psi = \delta\psi + (-iD_1\partial_\theta - \frac{D_2}{2!}\partial_\theta^2 + i\frac{D_3}{3!}\partial_\theta^3 + \dots)\psi - \gamma|\psi|^2\psi - i\frac{\kappa}{2}(\psi - \mathscr{H}) \tag{1.3}$$

where detuning $\delta = \omega_0 - \omega_p$ is the offset of pump frequency ω_p to its nearest cavity resonance. $D_1/2\pi$ is the free spectral range, and $D_2, D_3, \dots$ are the dispersion coefficients. The nonlinear strength $\gamma \approx \frac{n_2\omega_0}{2S_0n_0}$ is calculated with the transverse mode area S_0 and the nonlinear refractive

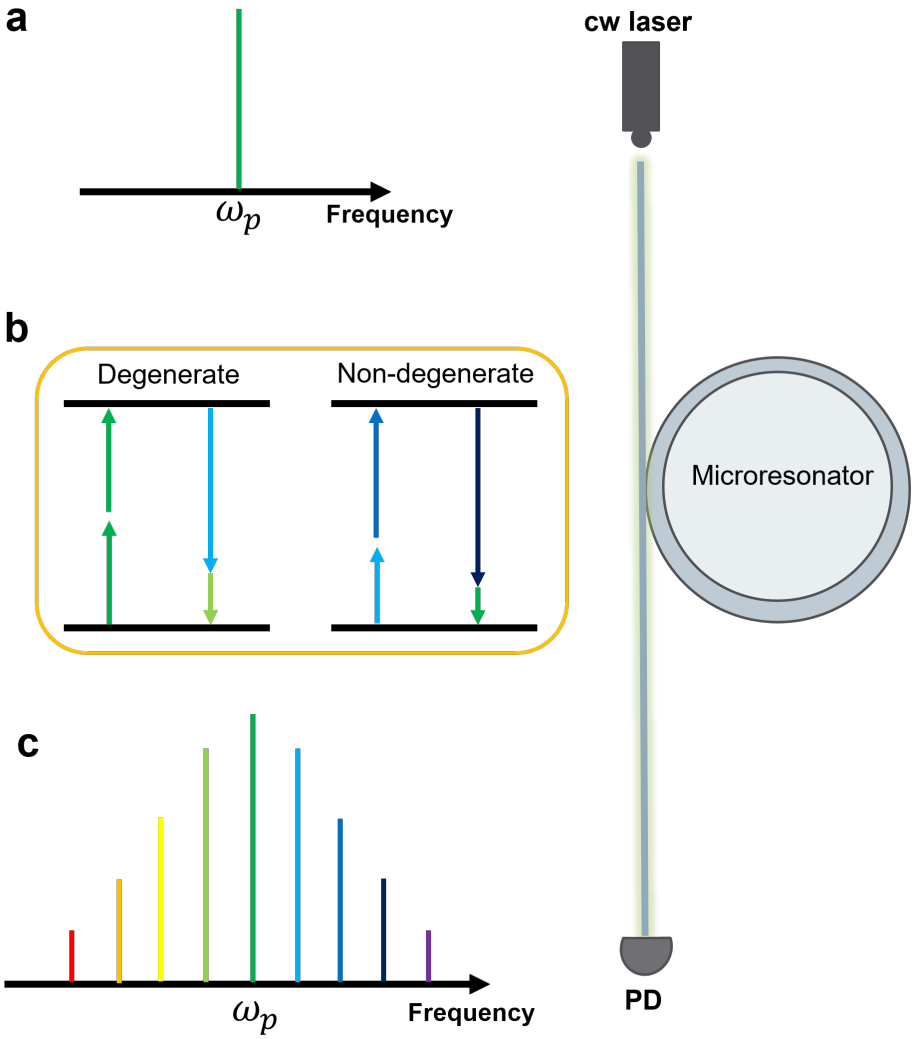

Fig. 1.3 The sketch of the CW-pumped microresonator. (a,c) Spectrums for the laser and detected from the photon detector (PD). (b) Degenerate four-wave mixing initiates with two pump photons splitting into two sideband frequencies (modes) under the momentum conservation. The non-degenerate process comes later and contributes to the cascaded frequency conversion.

index n_2. The total linewidth $\kappa = \kappa_i + \kappa_e$, where $\kappa_{i,e}$ accounts for the intrinsic (light scattering; material absorption; surface roughness) and extrinsic losses (coupling loss). The quality factor (Q factor) measures the photon lifetime in the cavity, and mathematically it is defined as the frequency-to-bandwidth ratio $Q = \omega/\kappa$ [26]. The intracavity power $\mathscr{H}^2 \sim \mathscr{W}\mathscr{F}$ is proportional to laser power $\mathscr{W}$ and resonator finesse $\mathscr{F} = \frac{D_1}{\kappa}$. The Kerr soliton comb (or DKSs) is sustained by the dual balances of dispersion versus nonlinearity and gain versus loss. The resonant frequencies counted from pump mode are ($\mu = 0$, where μ is the relative

longitudinal mode index):

$$\omega_\mu = \omega_0 + D_1\mu + \frac{D_2}{2!}\mu^2 + \frac{D_3}{3!}\mu^3 + \dots \tag{1.4}$$

where $D_1/2\pi$ is the repetition rate and dispersion coefficients $D_n = \frac{d^n\omega_\mu}{d\mu^n}$. The residual frequency for the mode μ is:

$$D_{res}(\mu) = \omega_\mu - (\omega_0 + D_1\mu) \tag{1.5}$$

D_{res} measures the deviation of the resonance from the equal-spaced grid. The decaying energy of comb lines on the left and right sides from the pump mode is caused by dispersion which moves the photon frequency away from the cavity resonance. If the high-order dispersions ($D_3\dots$) are negligible, it will be apparent that such deviation is proportional to μ^2 with coefficient D_2. When $D_2 > 0$ (anomalous dispersion), the dispersion shifts the frequencies away from the cavity resonances, which balances with the Kerr nonlinearity compensating such shifts. For $D_2 < 0$ (normal dispersion), instead of observing DKSs (i.e., bright solitons where the soliton amplitude is higher than the background), dark pulse (dark means the pulse core is lower than the background level) [27, 28] and switching waves (which links the high- and low-intensity of the bistable resonance) [29] may occur. The LLE is recognised as the detuned, damped and driven nonlinear Schrödinger equation (NLSE), where the NLSE part is solvable. When the system with the gain and loss, the DKS solutions are approximated solved with the soliton solution plus a low-intensity background [30, 31]. In 2014, T. Herr and colleagues found the temporal solitons generation and the step-like transitions to the multiple soliton states in a low linewidth ($\kappa \approx 450kHz$, $Q \approx 4\times10^8$) MgF_2 microresonator. The solitons emerge in the scan from the blue- to red-detuned regimes, where the modulation instability patterns, breather solitons and stable solitons have been demonstrated. The Bath's results regarding the pattern formations in the instability tongues provided new insights for this topic; see [32] for $\chi^{(2)}$ and [33] for $\chi^{(3)}$ microresonators.

In the presence of high-order dispersion, for instance, D_3 reshapes the residual dispersion. The sideband zero dispersion mode is estimated by setting the residual dispersion to 0:

$$D_{res} = \frac{D_2}{2!}\mu^2 + \frac{D_3}{3!}\mu^3 = 0 \tag{1.6}$$

The zero-dispersion mode will be efficiently enhanced and create the dispersive wave emissions, also known as Cherenkov radiations [34–37]. Such dispersive mode coupled with the soliton core is critical in the formation of molecule-bound states [38, 39]. Meanwhile, the enhanced mode will effectively extend the bandwidth of the combs, which raises great

interest for dispersion engineering by the geometry design of microresonators that shifts the material dispersion governed by the Sellmeier equation [40, 41].

The Kerr microcombs have been studied on various platforms owing to their merits in the broadband spectra and long-last coherence. The polished crystalline resonators (such as MgF_2, CaF_2, $LiNbO_3$) can have ultra-high Q above 10^{10} [42] with tens of GHz repetition rate. The SiN offers a much lower Q on the scale of 10^6, but it has a high refractive index and can be integrated with waveguides enabling a compact, and versatile chip [43]. Such state-of-the-art on-chip combs inspire an increasing amount of high-tech applications. For example, the equally spaced frequencies in the soliton comb serve as ideal sources for the wavelength division multiplexing in coherent telecommunications [44–46] and for quantum communications [47–49]. Meanwhile, two combs with slight frequency offset are taken for the dual-comb spectroscopy (see Fig.1.4) [50, 51]. In particular, recent studies have targeted the generation of two soliton combs in a single microresonator, which can further reduce the footprint of the integrated device. The dual combs can also be utilised in the ultrafast distance measurement (LIDAR-light detection and ranging) [52–54].

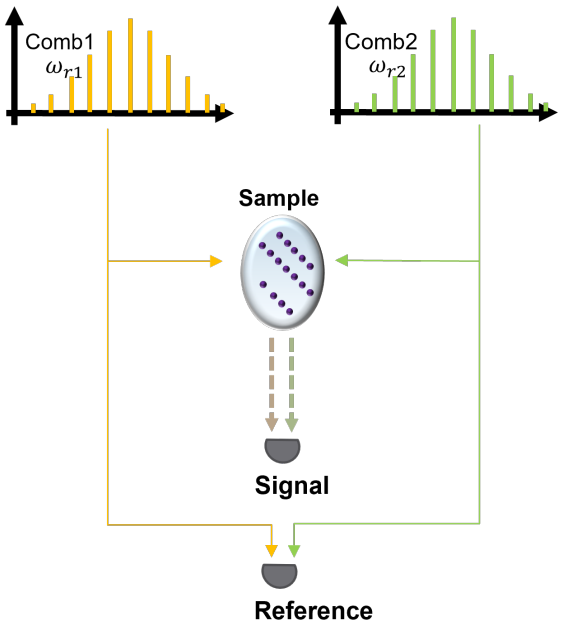

Fig. 1.4 The sketch of dual-comb spectroscopy. Two combs are sent to the sample and reference detector, where the absorption rate can be obtained from the difference between the beatnotes from the detectors.

1.3 Brief outline

We divide the topics into three major chapters. Chapter 2 discusses the bidirectional microresonators with counterrotating pumps. The state-of-the-art modelling provides a new approach to controlling counterrotating frequency combs in a high finesse microresonator through the averaged form of cross-phase modulations.

Chapter 3 focuses on the multiple soliton states, also known as soliton crystals. The periodic soliton crystals can be considered in a set of unit cells. We take the Bloch theorem for the computation of such periodic structures. By tuning the relative position of solitons in each unit cell, we confirm the nonlinear non-Hermitian system features a similar topological band spectrum compared to the SSH counterpart. Our study surrounding the topology includes the Berry phase, Wannier distribution, and the edge state formation in a defect crystal.

Chapter 4 considers the frequency comb generation in a $\chi^{(2)}$ resonator. Due to the momentum conservation in the OPO process, we separate the discussion of signal comb generation in terms of the parity of the pumping mode. We numerically observed the ordinary and staggered comb spectra and importantly, with the selection of frequency offset between the pump and signal combs, the soliton generation in the mid-IR range has been reported.

The last section summarises the thesis and forecasts future works.

References

[1] L. Essen, J. V. L. Parry, An atomic standard of frequency and time interval: a caesium resonator, Nature 176, 280 (1955).

[2] W. F. McGrew, X. Zhang, R. J. Fasano, S. A. Schäffer, K. Beloy, D. Nicolodi, R. C. Brown, N. Hinkley, G. Milani, M. Schioppo, T. H. Yoon, A. D. Ludlow, Atomic clock performance enabling geodesy below the centimetre level, Nature 564, 87 (2018).

[3] K. Beloy, M. I. Bodine, Frequency ratio measurements at 18-digit accuracy using an optical clock network, Nature 591, 7851 (2021).

[4] K. M. Evenson, J. S. Wells, F. R. Petersen, B. L. Danielson, and G. W. Day, Accurate frequencies of molecular transitions used in laser stabilization: the 3.39μm transition in CH4 and the 9.33 and 10.18μm transitions in CO2, Appl. Phys. Lett. 22, 192 (1973).

[5] S. A. Diddams, K. Vahala, T. Udem, Optical frequency combs: Coherently uniting the electromagnetic spectrum, Science 369, 267 (2020).

[6] D. E. Spence, P. N. Kean, W. Sibbett, 60-fsec pulse generation from a self-mode-locked Ti:sapphire laser, Opt. Lett. 16, 42 (1991).

[7] D. J. Jones et al., Carrier-envelope phase control of femtosecond mode-locked lasers and direct optical frequency synthesis, Science 288, 635 (2000).

[8] S. Droste, G. Ycas, B. Washburn, I. Coddington, N. Newbury, Optical Frequency Comb Generation based on Erbium Fiber Lasers, Nanophotonics 5, 196 (2016).

[9] P. DelHaye, A. Schliesser, O. Arcizet, T. Wilken, R. Holzwarth, T. J. Kippenberg, Optical frequency comb generation from a monolithic microresonator, Nature 450, 1214 (2007).

[10] S. M. Spillane, T. J. Kippenberg, K. J. Vahala, Ultralow-threshold Raman laser using a spherical dielectric microcavity, Nature 415, 621 (2002).

[11] Y. Liu, Z. Qiu, X. Ji, J. He, J. Riemensberger, M. Hafermann, R. Wang, J. Liu, C. Ronning, T. J. Kippenberg, A photonic integrated circuit based erbium-doped amplifier, arXiv:2204.02202 (2022).

[12] Ó. B. Helgason, M. Girardi, Z. Ye, F. Lei, J. Schröder and V. T. Company, Power-efficient soliton microcombs, arXiv:2202.09410 (2022).

[13] Z. Fan, D. N. Puzyrev, D. V. Skryabin, Soliton metacrystals: topology and chirality, Commun. Phys. 5, 248 (2022).

[14] L. A. Lugiato, R. Lefever, Spatial Dissipative Structures in Passive Optical Systems, Phys. Rev. Lett. 58 (21): 22092211 (1987).

[15] A. Turing, The Chemical Basis of Morphogenesis, Philosophical Transactions of the Royal Society of London B. 237 (641): 3772 (1952).

[16] Y. K. Chembo, C. R. Menyuk, Spatiotemporal Lugiato-Lefever formalism for Kerr-comb generation in whispering-gallery-mode resonators, Phys. Rev. A 87, 053852 (2013).

[17] S. Coen, H. G. Randle, T. Sylvestre, M. Erkintalo, Modeling of octave-spanning Kerr frequency combs using a generalized mean-field Lugiato-Lefever model, Opt. Lett. 38, 3739 (2013).

[18] M. Haelterman, S. Trillo, S. Wabnitz, Dissipative modulation instability in a nonlinear dispersive ring cavity, Optics Commun. 91, 401407 (1992).

[19] C. Godey C, I. V. Balakireva, A. Coillet, Y. K. Chembo, Stability analysis of the spatiotemporal Lugiato-Lefever model for Kerr optical frequency combs in the anomalous and normal dispersion regimes, Phys. Rev. A 89, 063814 (2014).

[20] N. M. Kondratiev and V. E. Lobanov, Modulational instability and frequency combs in whispering-gallery-mode microresonators with backscattering, Phys. Rev. A 101, 013816 (2020).

[21] D. C. Cole, A. Gatti, S. B. Papp, F. Prati, and L. Lugiato, Theory of Kerr frequency combs in Fabry-Perot resonators, Phys. Rev. A 98, 013831 (2018).

[22] A. J. Scroggie, W. J. Firth, G. S. McDonald, M. Tlidi, R. Lefever, L. Lugiato, Pattern formation in a passive Kerr cavity, Chaos, Solitons & Fractals, 4, 1323 (1994).

[23] K. Nozaki, N. Bekki, Low-dimensional chaos in a driven damped nonlinear Schrödinger equation, Physica D: Nonlinear Phenomena, 21, 381 (1986).

[24] S. Wabnitz, Suppression of interactions in a phase-locked soliton optical memory, Opt. Lett., 18, 601-603 (1993).

[25] D. V. Skryabin, Hierarchy of coupled mode and envelope models for bi-directional microresonators with Kerr nonlinearity, OSA Continuum 3, 1364-1375 (2020).

[26] F. Vanier, C. L. Mela, A. Hayat, and Y. Peter, Intrinsic quality factor determination in whispering gallery mode microcavities using a single Stokes parameters measurement, Opt. Express 19, 23544-23553 (2011).

[27] S. Zhang, T. Bi, G. N. Ghalanos, N. P. Moroney, L. D. Bino, and P. DelHaye, Dark-Bright Soliton Bound States in a Microresonator, Phys. Rev. Lett. 128, 033901 (2022).

[28] X. Xue, Y. Xuan, Y. Liu, P. Wang, S. Chen, J. Wang, D. E. Leaird, M. Qi , A. M. Weiner, Mode-locked dark pulse Kerr combs in normal-dispersion microresonators, Nature Photonics, 9, 594600 (2015).

[29] M. H. Anderson, A. Tikan, A. Tusnin, J. Riemensberger, R. Wang, T. J. Kippenberg, Dissipative solitons and switching waves in dispersion folded Kerr cavities, arXiv:2205.09957 (2022).

[30] T. Herr, V. Brasch, J. D. Jost, C. Y. Wang, N. M. Kondratiev, M. L. Gorodetsky , T. J. Kippenberg, Temporal solitons in optical microresonators, Nature Photonics 8, 145152 (2014).

[31] S. Wabnitz, Suppression of interactions in a phase-locked soliton optical memory. Opt. Lett. 18, 601603 (1993).

[32] D. N. Puzyrev, V. V. Pankratov, A. Villois, D. V. Skryabin, Bright-soliton frequency combs and dressed states in chi(2) microresonators, Physical Review A 104 (1), 013520 (2021).

[33] D. V. Skryabin, Z. Fan, A. Villois, D. N. Puzyrev, Threshold of complexity and Arnold tongues in Kerr-ring microresonators, Physical Review A 103 (1), L011502 (2021).

[34] N. Akhmediev, M. Karlsson, Cherenkov radiation emitted by solitons in optical fibers, Phys. Rev. A 51, 26022607 (1995).

[35] A. V. Cherenkov, V. E. Lobanov, M. L. Gorodetsky, Dissipative Kerr solitons and Cherenkov radiation in optical microresonators with third-order dispersion, Phys. Rev. A 95, 033810 (2017).

[36] C. Bao et al., High-order dispersion in Kerr comb oscillators, J. Opt. Soc. Am. B 34, 715 (2017).

[37] D. V. Skryabin, Y. V. Kartashov, O. A. Egorov, M. Sich, J. K. Chana, L. E. Tapia Rodriguez, P. M. Walker, , E. Clarke, B. Royall, M. S. Skolnick, , D. N. Krizhanovskii, Backward Cherenkov radiation emitted by polariton solitons in a microcavity wire. Nature communications, 8(1), 1554 (2017).

[38] W. Weng, R. Bouchand, E. Lucas, E. Obrzud, T. Herr , T. J. Kippenberg, Heteronuclear soliton molecules in optical microresonators, Nature Communications, 11, 2402 (2020).

[39] R. Luo, H. Liang, and Q. Lin, Multicolor cavity soliton, Opt. Express 24, 16777-16787 (2016).

[40] M. Foster, A. Turner, J. Sharping, B. S. Schmidt, M. Lipson , A. L. Gaeta, Broad-band optical parametric gain on a silicon photonic chip, Nature 441, 960963 (2006).

[41] W. Sellmeier, Ueber die durch die Aetherschwingungen erregten Mitschwingungen der Körpertheilchen und deren Rückwirkung auf die ersteren, besonders zur Erklärung der Dispersion und ihrer Anomalien (II. Theil). Annalen der Physik und Chemie. 223 (11): 386403 (1872).

[42] V. S. Ilchenko, A. A. Savchenkov, A. B. Matsko, and L. Maleki, Nonlinear Optics and Crystalline Whispering Gallery Mode Cavities, Phys. Rev. Lett. 92, 043903 (2004).

[43] V. Brasch, Q. F. Chen, S. Schiller, T. J. Kippenberg, Radiation hardness of high-Q silicon nitride microresonators for space compatible integrated optics, Opt. Express 22, 3078630794 (2014).

[44] P. Marin-Palomo et al., Microresonator-based solitons for massively parallel coherent optical communications, Nature 546, 274279 (2017).

[45] P. M. Palomo, J. N. Kemal, T. J. Kippenberg, W. Freude, S. Randel, and C. Koos, Performance of chip-scale optical frequency comb generators in coherent WDM communications, Opt. Express 28, 12897-12910 (2020).

[46] J. N. Kemal, P. M. Palomo, M. Karpov, M. H. Anderson, W. Freude, T. J. Kippenberg, C. Koos, Chapter 2 - Chip-based frequency combs for wavelength-division multiplexing applications, Optical Fiber Telecommunications VII, 51-102 (2020).

[47] G. Maltese, M. I. Amanti, F. Appas, et al., Generation and symmetry control of quantum frequency combs. npj Quantum Inf 6, 13 (2020).

[48] M. Kues, C. Reimer, P. Roztocki, L. R. Cortés, S. Sciara, B. Wetzel, Y. Zhang, A. Cino, S. T. Chu, B. E. Little, D. J. Moss, L. Caspani, J. Azaña , R. Morandotti, On-chip generation of high-dimensional entangled quantum states and their coherent control. Nature 546, 622626 (2017).

[49] M. Kues, C. Reimer, J. M. Lukens, W. J. Munro, A. M. Weiner, D. J. Moss , R. Morandotti, Quantum optical microcombs, Nature Photonics 13, 170179 (2019).

[50] I. Coddington, N. Newbury, W. Swann, Dual-comb spectroscopy, Optica 3, 414 (2016).

[51] A. Dutt, C. Joshi, X. Ji, J. Cardenas, Y. Okawachi, K. Luke, A. L. Gaeta, M. Lipson, On-chip dual-comb source for spectroscopy, Sci. Adv., 4:e170185 (2018).

[52] N. Kuse, M. E. Fermann, Frequency-modulated comb LIDAR, APL Photonics 4, 106105 (2019).

[53] E. Baumann, F. R. Giorgetta, I. Coddington, L. C. Sinclair, K. Knabe, W. C. Swann, and N. R. Newbury, Comb-calibrated frequency-modulated continuous-wave ladar for absolute distance measurements, Opt. Lett. 38, 20262028 (2013).

[54] J. Nürnberg, B. Willenberg, C. R. Phillips, and U. Keller, Dual-comb ranging with frequency combs from single cavity free-running laser oscillators, Opt. Express 29, 24910-24918 (2021).

Chapter 2

Bi-directional Kerr microresonators

2.1 Background and motivation

Bi-directional (counterrotating) micro-ring resonators are driven by dual sources circulating in the opposite, i.e., clockwise (CW) and counter-clockwise (CCW) directions, see Fig.2.1. Rich symmetry-breaking behaviours with their potential applications in velocity measurements and signal detections have been reported in recent years. One notable feature of microresonators is their high finesse which provides hundreds to millions of boosts to the circulating powers relative to the input level, making vastly enhanced nonlinear responses. The advanced gyroscope using a silica microrod microresonator (with a diameter of 2.8 mm and $Q = 2.9 \times 10^8$ coupled to a tapered optical fibre pumped with laser light at 1550 nm) has been proved to provide ultra-high rotative sensitivity (with a responsivity enhanced by a factor of around 10^4) by setting the device near the symmetry breaking threshold (i.e. exceptional points) [1].

The bright counterpropagating solitons (CP solitons) are found in a microresonator pumped by bidirectional lasers. Such CP solitons advance the next-generation design of the integrated dual-comb spectroscopy and laser ranging systems [2–7]. A variety of qualitative models have been used to map bidirectional microresonators, see [8] for an overview. Unlike the unidirectional regime, we notice the complexity brought by the opposite group velocities of CW and CCW fields where the Lorentz transformation cannot help to simplify the model. However, the high-finesse terms in the Lugiato-Lefever model can be considered in an averaged form with a reshaped form of nonlinear cross-coupling between the bidirectional fields shifting the detuning [8]. This treatment implies the manipulation of frequency combs utilising the high sensitivity of the effective detuning which relies on the nonlinear response between the bidirectional fields.

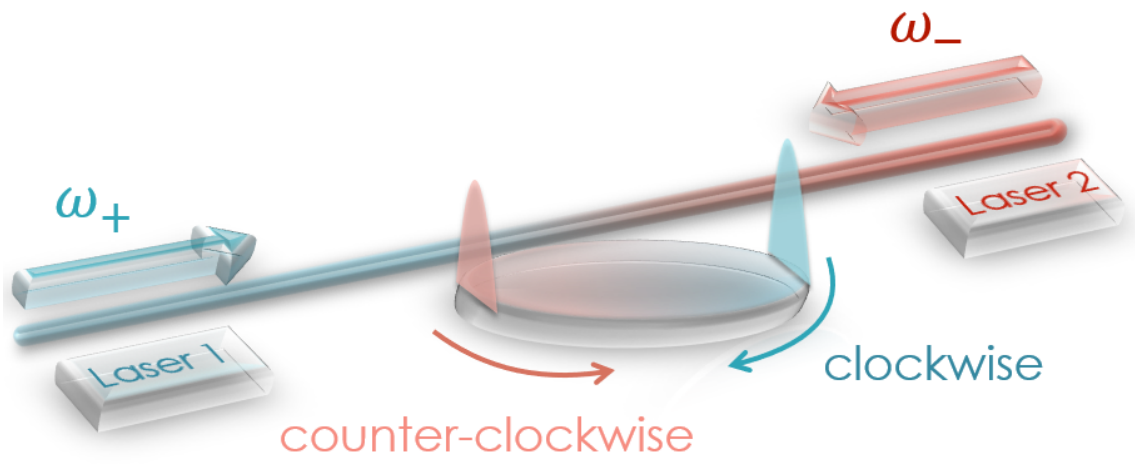

Fig. 2.1 Sketch of the bidirectional model. The microresonator is pumped by the clockwise/counter-clockwise fields with laser frequencies ω_+/ ω_-.

Microcomb generation in two-component systems has been an active area due to some unique benefits: the conversion efficiency can exceed 50% by inducing a controllable frequency shift to a selected cavity resonance [9] from an auxiliary microring. Ref.[10] reports the deterministic generation of a single soliton state in a wide spectral range spanning over 1.5 octaves (near 200THz) with the auxiliary pump. Taking the idea of controlling the resonance shift, in our model, we realised the manipulation of soliton combs through the strength of cross-phase modulations.

In the following, we first introduce the bidirectional model, in particular, we show the steps to average out the fast oscillating parts. Then, we discuss the excitation of sideband modes, i.e., the families of the homogeneous states and their stability. The soliton blockade has been observed by tuning the resonator into the ranges where no steady states exist. The management of frequency combs is further considered by tuning laser frequencies and powers. Lastly, the instability of homogeneous states has been investigated and revealed tongue-like structures.

2.2 Counterrotating waves and frequency combs in bidirectional microresonators

2.2.1 Model derivation

We start with the general model of coupled LLEs for a bidirectional microresonator and then derive the averaging form under the high finesse condition. The coupled LLEs are written as [8]:

$$i\partial_t Q_+ = \delta_+ Q_+ - iD_1\partial_\theta Q_+ - \frac{D_2}{2}\partial_\theta^2 Q_+ - i\frac{\kappa}{2}(Q_+ - \mathscr{H}_+) - \gamma(|Q_+|^2 + 2|Q_-|^2)Q_+ \quad (2.1)$$

$$i\partial_t Q_- = \delta_- Q_- + iD_1\partial_\theta Q_- - \frac{D_2}{2}\partial_\theta^2 Q_- - i\frac{\kappa}{2}(Q_- - \mathscr{H}_-) - \gamma(|Q_-|^2 + 2|Q_+|^2)Q_- \quad (2.2)$$

where $Q_\pm$ are the bidirectional wave envelopes, and $\delta_\pm = \omega_0 - \omega_\pm$ are the detunings between the laser frequencies and their nearest resonant modes. $D_1/2\pi$ is the repetition rate, for CW and CCW waves, they should have positive and negative signs due to opposite group velocities. $D_2 > 0/D_2 < 0$ accounts for the anomalous/normal dispersion; κ is the loaded linewidth. $\gamma \approx \frac{\omega_0 n_2}{2S_0 n_0}$ is the nonlinear factor inversely proportional to the transverse mode area S_0 and $n_2 = \frac{3\chi^{(3)}}{4\varepsilon_0 c n_0^2}$. The intracavity powers $|\mathscr{H}_\pm|^2$ and cavity finesse $\mathscr{F}$ are defined in the following [11]:

$$|\mathscr{H}_\pm|^2 = \frac{\eta}{\pi}\mathscr{W}_\pm\mathscr{F} \quad (2.3)$$

$$\mathscr{F} = \frac{D_1}{\kappa} \quad (2.4)$$

Here, $\eta = \kappa_c/\kappa$, where κ_c is the coupling loss, i.e.,$\eta = 0.5$ for critical coupling [12]. The diagram displayed in Fig.2.2 shows the moving reference and static reference regimes. In the former case, the Lorentz transformation can get rid of D_1 in one component, but it will lead to the double rate of $2D_1$ in the counterrotating field.

Fig. 2.2 Moving reference frame (left) and static reference frame (right) for propagating waves in a microresonator.

The transformation of the coupled-mode representation reveals the impact of high finesse D_1/κ. We define a set of auxiliary fields $B_\mu^\pm$ as:

$$Q_\pm(t,\theta) = \sum_\mu B_\mu^\pm e^{\pm i\mu\theta - i\delta_\mu t}, \;\; \delta_\mu = \delta_\pm + D_1\mu + \frac{D_2}{2}\mu^2 \tag{2.5}$$

We first deal with the CW part, and the same treatment can be applied to the CCW. The above relation transfers the model into coupled-mode regime:

$$\begin{aligned} i\partial_t B_\mu^+ + i\frac{\kappa}{2}(B_\mu^+ + \hat{\delta}_{\mu,0}\mathscr{H}_+) = -\gamma \sum_{\mu_1,\mu_2,\mu_3} \hat{\delta}_{\mu_1-\mu_2+\mu_3,\mu}(B_{\mu_1}^+ B_{\mu_2}^{+*} B_{\mu_3}^+ e^{-it(\delta_{\mu_1}-\delta_{\mu_2}+\delta_{\mu_3}-\delta_\mu)} \\ +2B_{\mu_1}^{-*} B_{\mu_2}^- B_{\mu_3}^+ e^{-it(-\delta_{\mu_1}+\delta_{\mu_2}+\delta_{\mu_3}-\delta_\mu)}) \end{aligned} \tag{2.6}$$

Note the two terms on the right side correspond to self-phase modulation (SPM) and cross-phase modulation (XPM). The expansion of the nonlinearity kernels are subjected to the Kronecker $\hat{\delta}$, which returns 1 under the momentum conversion $\mu_1 - \mu_2 + \mu_3 = \mu$:

$$\delta_{\mu_1} - \delta_{\mu_2} + \delta_{\mu_3} - \delta_\mu = \frac{D_2}{2}(\mu_1^2 - \mu_2^2 + \mu_3^2 - \mu^2) \tag{2.7}$$

$$-\delta_{\mu_1} + \delta_{\mu_2} + \delta_{\mu_3} - \delta_\mu = 2D_1(\mu_2 - \mu_1) + \frac{D_2}{2}(-\mu_1^2 + \mu_2^2 + \mu_3^2 - \mu^2) \tag{2.8}$$

The phase term with D_1 is cancelled under the Kronecker relation in SPM, but D_1 still remains in the XPM part. The XPM term implies the following two scenarios: when $\mu_1 = \mu_2$, the XPM can get rid of D_1. Meanwhile, the terms inside the brackets of D_2 can be reduced to $(\mu_3^2 - \mu^2)$. When $\mu_1 \neq \mu_2$, D_1 will keep in the exponential phase. The condition of a high finesse microresonator allows the approximation: when the scale of D_1 is much larger than other physical parameters (such as D_2, κ, etc.) in the system, for instance, the silica microresonator can have $D_1/(2\pi) \approx 20GHz$, $D_2/(2\pi) \approx 10kHz$, $\kappa/(2\pi) \approx 1.5MHz$, the fast and slow time scales can be effectively separated into the terms associated with and without D_1. The averaged model considers the time scale much larger than the roundtrip circulating time and smaller than the photon lifetime, allowing to average out the phase term oscillating at the level of D_1. Given the discussions above, we conclude that:

$$\begin{aligned} i\partial_t B_\mu^+ + i\frac{\kappa}{2}(B_\mu^+ + \hat{\delta}_{\mu,0}\mathscr{H}_+) = -\gamma \sum_{\mu_1,\mu_2,\mu_3} \hat{\delta}_{\mu_1-\mu_2+\mu_3,\mu} B_{\mu_1}^+ B_{\mu_2}^{+*} B_{\mu_3}^+ e^{-it(\delta_{\mu_1}-\delta_{\mu_2}+\delta_{\mu_3}-\delta_\mu)} \\ +2B_\mu^+ \sum_{\mu_1} |B_{\mu_1}^-|^2 \end{aligned} \tag{2.9}$$

To transfer the pair of coupled-mode equations into the spatial domain, notation A_μ is defined:

$$\psi_\mu^\pm = B_\mu^\pm e^{-it\delta_\mu\prime}, \;\; \delta_\mu\prime = \delta_\pm + \frac{1}{2}D_2\mu^2 \tag{2.10}$$

$$i\partial_t\psi_\mu^+ = \delta_+\psi_\mu^+ + \frac{D_2}{2}\mu^2\psi_\mu^+ - i\frac{\kappa}{2}(\psi_\mu^+ - \mathscr{H}_+) - \gamma\sum_{\mu_1,\mu_2,\mu_3}\hat{\delta}_{\mu_1-\mu_2+\mu_3,\mu}\psi_{\mu_1}^+\psi_{\mu_2}^{+*}\psi_{\mu_3}^+ \tag{2.11}$$
$$-2\gamma\psi_\mu\sum_{\mu_1}|\psi_{\mu_1}^-|^2$$

The spatial form $\psi^\pm$ satisfies:

$$\psi^\pm(\theta,t) = \sum_\mu \psi_\mu^\pm e^{\pm i\mu\theta} \tag{2.12}$$

The integration of $\psi_\mu^\pm$ gives: (note that the transformation of the last term takes Parseval's theorem)

$$i\partial_t\psi^+ = \delta_+\psi^+ - \frac{D_2}{2}\partial_\theta^2\psi^+ - i\frac{\kappa}{2}(\psi^+ - \mathscr{H}_+) - \gamma|\psi^+|^2\psi^+ - 2\gamma\psi^+\int_0^{2\pi}|\psi^-|^2\frac{d\theta}{2\pi} \tag{2.13}$$

The same process has been taken for the Q_- component, which finally returns the form:

$$i\partial_t\psi^- = \delta_-\psi^- - \frac{D_2}{2}\partial_\theta^2\psi^- - i\frac{\kappa}{2}(\psi^- - \mathscr{H}_-) - \gamma|\psi^-|^2\psi^- - 2\gamma\psi^-\int_0^{2\pi}|\psi^+|^2\frac{d\theta}{2\pi} \tag{2.14}$$

The pair of Eqs.(2.13, 2.14) shows the nonlinear cross-coupling between the bidirectional fields as detuning shifts. Note that the revised model compared to its original form reveals the intuitive impact from the cross-phase modulation acting on the detuning. Meanwhile, from the numerical aspect, the computational efficiency has been largely boosted by the increase in discrete time steps.

2.3 Steady states solutions

In this section, the resonances between the bi-directional fields are solved, including the studies of symmetry breaking, dark-bright resonance formation, and the manipulation of frequency combs.

2.3.1 Symmetry breaking and dark-bright resonances

The sketch of the bi-directionally pumped microresonator mapped by Eqs.(2.13, 2.14) is illustrated in Fig.2.1. The clockwise (CW) and counter-clockwise (CCW) lights $\psi^{\pm}$ are printed in blue and red, respectively. Swapping of the two lasers with the same frequencies and powers will not change the system, which implies a set of symmetric solutions. In the single-mode regime, the homogeneous (cw) states can be tracked under the condition of $\partial_t = 0, \partial_\theta = 0$. The typical symmetric family is presented by black branches in Fig.2.3(c1, c2). The asymmetric solutions $\psi^+ \neq \psi^-$ will emerge at the exceptional (symmetry-breaking) points with the laser powers above the threshold [13].

The emergence of asymmetric solutions should be associated with the stability of pump mode, where the instability makes the small fluctuations between the bidirectional lights amplified and lead to the symmetry-breaking states. The splitting of power will cause the CW and CCW lights to go through different refractive indices, as the intensity-induced variations in refractive index Δn for CW and CCW lights should be proportional to $|\psi^+|^2 + 2|\psi^-|^2$ and $|\psi^-|^2 + 2|\psi^+|^2$, separately. It reveals the counterrotating lights in the cavity have different resonant frequencies. Specifically, the maximal difference of the refractive indices is rough Δn and $2\Delta n$ in two components. When the bifurcation happens, the counterrotating lights with equal intensity will break into a pair of strong- and weak-intensity branches. The blue pair in Fig.2.3(c1, c2) is a typical case for a strong CW and weak CCW case and vice versa, displayed by the green pair. Such a strong- or weak-intensity state selection is random [14], due to the unpredictable perturbations.

The model of counterrotating fields is derived in last subsection, see Eqs.(2.13, 2.14). The integral intensity $I_{\pm}$ are defined below:

$$I^+ = \int_0^{2\pi} |\psi^+(\theta)|^2 \frac{d\theta}{2\pi} \tag{2.15}$$

$$I^- = \int_0^{2\pi} |\psi^-(\theta)|^2 \frac{d\theta}{2\pi} \tag{2.16}$$

It solves the cw-cw states (homogeneous fields in both components) in the following:

$$I^+ + \frac{4I^+}{\kappa^2}\left([\delta_+ - 2I^-] - I^+\right)^2 = \gamma {\mathscr{H}_+}^2, \tag{2.17}$$

$$I^- + \frac{4I^-}{\kappa^2}\left([\delta_- - 2I^+] - I^-\right)^2 = \gamma {\mathscr{H}_-}^2, \tag{2.18}$$

We apply a set of parameters for a typical silica microresonator: $D_2/2\pi = 10$kHz and $\gamma/2\pi = 400$kHz/W are the anomalous dispersion and nonlinear coefficients. $\kappa/2\pi = 1.5$MHz is the resonance linewidth. The intracavity pump powers are ${\mathscr{H}_\pm}^2 = \frac{\eta}{\pi}\mathscr{F}\mathscr{W}_\pm$, where $\eta = 0.5$ accounts for the critical coupling. Resonator finesse $\mathscr{F} = 13000$ relates to the enhancement of power in the cavity.

The study of the bidirectional system starts from the homogeneous states, providing significant information on sideband excitations. The controlling parameters are the laser powers$\mathscr{H}_\pm$ and frequencies $\omega_\pm$. In this section, the target is to keep equal power (the discussions of power will be included in the next section) and figure out the strong and weak nonlinear interactions between bidirectional fields during the detuning scans. Two regimes should be considered: the offset frequency between two lasers and the exact detuning between the laser and its nearest cavity resonance. For the convenience, we define the offset between two lasers as $\varepsilon = \omega_+ - \omega_-$, and the exact detuning between zero-mode resonance and clockwise laser frequency as $\delta = \omega_0 - \omega_+$. The modified model can be written as:

$$i\partial_t \psi^+ = \delta\psi^+ - \frac{D_2}{2}\partial_\theta^2\psi^+ - i\frac{\kappa}{2}(\psi^+ - \mathscr{H}_+) - \gamma|\psi^+|^2\psi^+ - 2g^-\psi^+ \tag{2.19}$$

$$i\partial_t \psi^- = \delta\psi^- - \frac{D_2}{2}\partial_\theta^2\psi^- - i\frac{\kappa}{2}(\psi^- - \mathscr{H}_- e^{i\varepsilon t}) - \gamma|\psi^-|^2\psi^- - 2g^+\psi^- \tag{2.20}$$

$$g^\pm = \frac{\gamma}{2\pi}\int_0^{2\pi} |\psi^\pm|^2 d\theta \tag{2.21}$$

$g^\pm$ are the nonlinear couplings between the bidirectional lights, serving as the shifts in detuning. Thus, the effective net detunings for $\pm$ components are $\delta - 2g^-$ and $\delta + \varepsilon - 2g^+$.

Fig.2.3(a) presents a group of nonlinear resonances between CW and CCW fields under small and large frequency offsets ε. The horizontal axis shows the scan in laser frequency. Due to the fixed ε, both lasers scan at the same speed. For a relatively large offset, the resonance in (a1, a2) shows the case of weak cross-interactions because of the feeble g^- component. Specifically, it means such a large offset decouples the two components, i.e., the

approximation $g^- \approx 0$ assumes that ψ^+ is roughly independent. The strong cross-interactions will happen at a small offset ε. With absent offset, the central panel (c1, c2) displays a pair of typical symmetry-breaking states where two identical lasers are taken. (d1, d2) and (e1, e2) possess similar manner concerning the first two cases in (b1, b2) and (a1, a2) if $\psi^\pm$ are swapped. The only difference in the shift along the horizontal axis is the consequence of the tilted resonance. To enhance the cross-coupling between bidirectional lights, the selection of δ within a well-pronounced range should be guaranteed, especially for identifying the impacts of such nonlinear shifts.

Accordingly, we fix the laser-cavity offset in the $'+'$ component near the resonance, with laser scanning along ω_-. In panels (f, g), the resonance loops are printed in different styles of lines and colours for the convenience of catching the correspondence of $g^\pm$ from the cw states. Starting from the efficient high ω_-, the weak interactions between CW and CCW waves solve the upper (black), middle (dashed blue) and lower (solid blue) branches at $\varepsilon/2\pi \approx -7MHz$. Provided that the CCW light is far away from the resonance, the strong nonlinear shifts from $g^+ \approx 5$ and 0 cannot primarily affect the intensity in g^- (see the comparison between solid blue and black line in panel (g)). When the laser is approaching the resonance by decreasing ω_-, the increasing intensity in g^- should apparently shift the detuning of CW light as per the relation $\delta - 2g^-$. The closed blue loop in panel (f) suggests the effective detuning no longer stays within the bistable range, and only the black upper branch survives. In the range $0 < \varepsilon/2\pi < 3$MHz, ω_- is approaching the resonance and maximizing the integral power, which shifts the CW component enormously, forming the dark-bright resonance, i.e., the black anti-resonant curves. The further decreasing ω_- will restore the net detuning for the CW component and create roughly the same level intensities of the multiple resonances at $\varepsilon/2\pi \approx 10$MHz. Remember that the dissipative Kerr solitons seek stable low-intensity states as a background (see discussions in Chapter 1), the interval between low-intensity states on the left and right sides strictly forbids the existence of dissipative Kerr solitons. The stability is also significant and we mark the instability threshold for $\mu = 0$ in the green dot, and sideband mode $\mu \neq 0$ in blue. According to the instability analysis, the destabilization of solitons will emerge in the process of frequency scan.

2.3.2 Soliton states

Steady-state soliton families can be divided into three broad categories of the soliton-cw, cw-soliton, and soliton-soliton states. The order of words indicates the state in CW and CCW waves, respectively. In Fig.2.4, the solutions for soliton-cw and cw-soliton states are sought

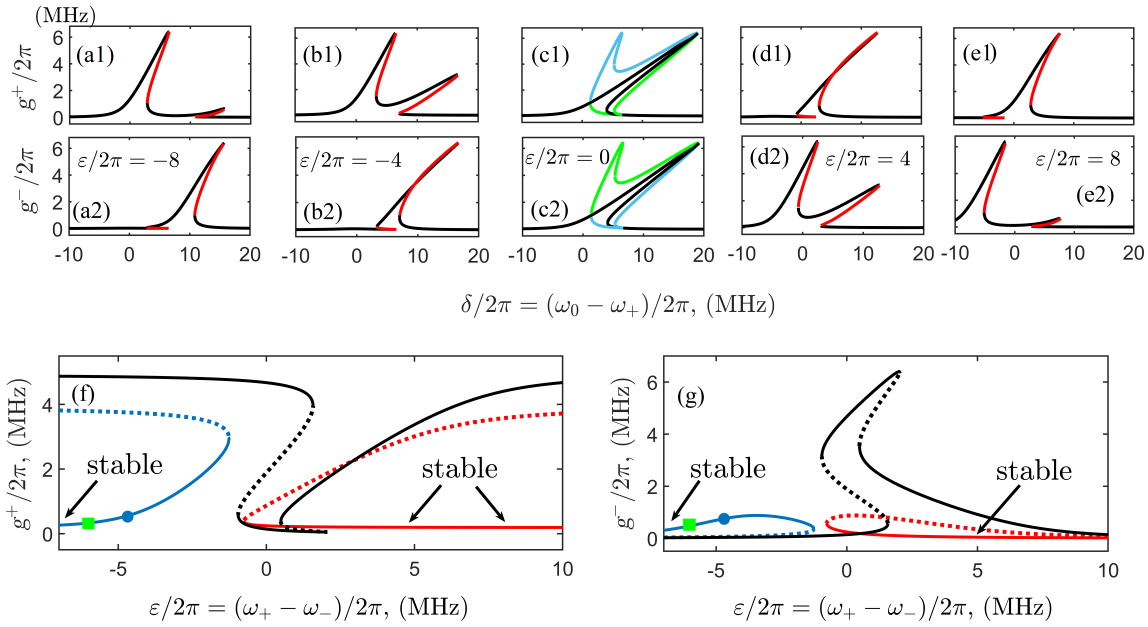

Fig. 2.3 (a-e) Strong (weak) interactions of bidirectional single-mode states with small (large) pump frequency offset ε. The colourful branches in the top and bottom panels present the pair of $g^{\pm}$ solutions. (f, g) Dark-bright resonance formation with the scan in offset frequency ε at fixed $\delta = (2\pi)4.5$MHz. Green and blue points are associated with instability of pump mode and sideband modes, respectively. Same powers are taken $\mathscr{H}_+ = \mathscr{H}_+ = 4W^{1/2}$.

in pairs below:

$$0 = \delta\psi^+ - \frac{D_2}{2}\partial_\theta^2\psi^+ - i\frac{\kappa}{2}(\psi^+ - \mathscr{H}_+) - \gamma|\psi^+|^2\psi^+ - 2g^-\psi^+ \tag{2.22}$$

$$\gamma\mathscr{H}_-{}^2 = g^- + 4g^-(\delta + \varepsilon - g^- - 2g^+)^2/\kappa^2 \tag{2.23}$$

and

$$\gamma\mathscr{H}_+{}^2 = g^+ + 4g^+(\delta - g^+ - 2g^-)^2/\kappa^2 \tag{2.24}$$

$$0 = (\delta + \varepsilon)\psi^- - \frac{D_2}{2}\partial_\theta^2\psi^- - i\frac{\kappa}{2}(\psi^- - \mathscr{H}_-) - \gamma|\psi^-|^2\psi^- - 2g^+\psi^- \tag{2.25}$$

The third-party, soliton-soliton state, should be solved with Eqs.(2.22,2.25). To keep consistency, same parameters in Fig.2.3 (f, g) are taken. We call 'soliton blockade' for the forbidden area of solitons, i.e., the grey carpet in Fig.2.4 (a). Such blockade effect can be

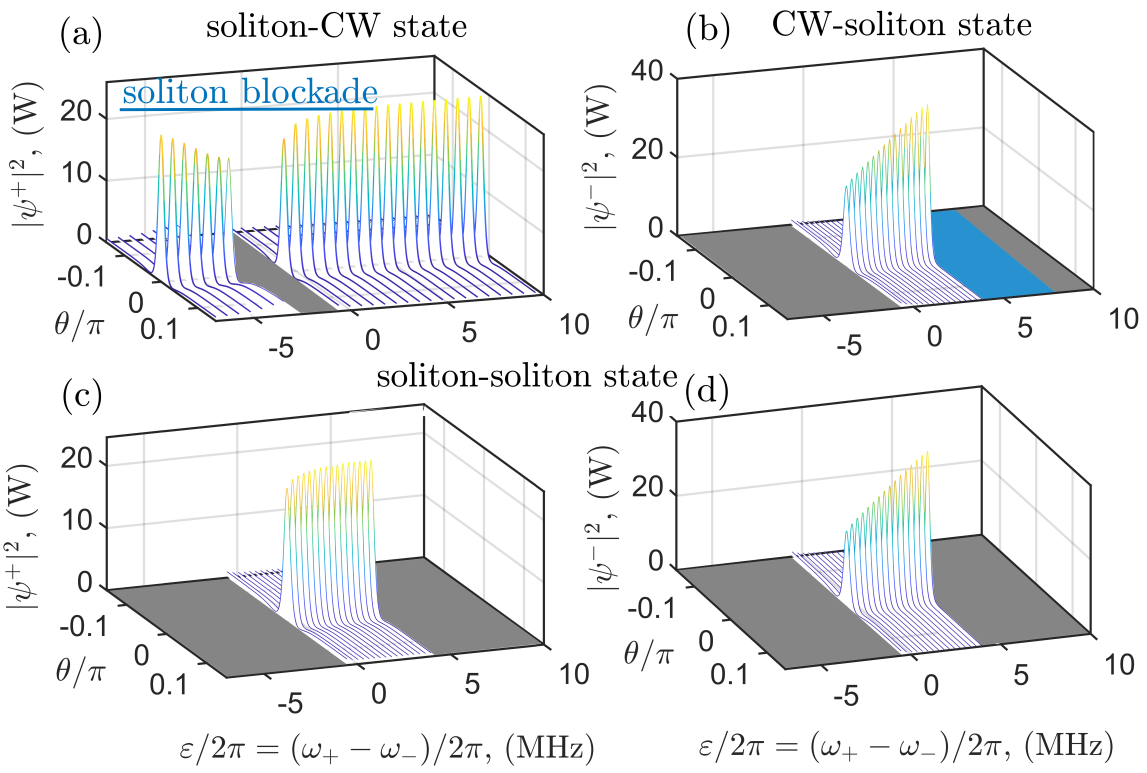

Fig. 2.4 (a, b) Soliton components of the soliton-cw and of the cw-soliton states as computed from the time-independent models. (c, d) is the soliton-soliton state. Panel (a) shows the soliton blockade. The blue colour in (b) marks the ε interval where the $'-'$ soliton is sustained by the chaotic state in the $'+'$ wave, which provides a relatively large XPM induced resonance shift, $-2g^+$, compensating for $\varepsilon > 0$ [15].

explained by the effective decreasing detuning in the soliton component when the ω_- is approaching the microresonator resonance where no stable background can be found for solitons. It also accounts for the range of the grey carpet comparable to the interval of low-intensity states in Fig.2.3 (f). The soliton profiles have determined the transition of net effective detuning in the $'+'$ wave. Observation of sharper solitons near the two edges of the 3D box indicates the wider spectrum, showing increasing frequency conversion efficiency. Panel(b) presents the soliton component in $'-'$ wave when cw state is taken in $'+'$. When the laser scans sweep from one side to the resonance, the growing intensity implies the solitons are approaching the tilted-peak resonance. Both blue and grey carpets stand for the non-existence region of the soliton family, but in the real-time dynamics, solitons can emerge in the blue carpet area when the cw state in $'+'$ is replaced with a chaotic field, as the chaotic ψ^+ field provides much larger detuning shift than cw state to compensate the

incremental detuning in $'-'$ component. The soliton-soliton state is only possible when ω_- approaches the resonance in the $'-'$ component. This condition requires $\varepsilon/2\pi > -1MHz$ where the steady-state solutions are captured in panels (c, d).

The formation of dark-bright resonance, the mechanism of soliton blockade, as well as the steady-state solitons have been discussed above. All these observations are in relation to the fixed δ. It becomes intuitive to control the detuning between ω_+ and ω_0 for the shifts of the resonance curves. The available detuning range is solved by setting $g^- = 0$, i.e., switching off the light in $'-'$. The increment of $\delta/2\pi$ from $4.5MHz$ to $6MHz$ (near the peak resonance) gives the shifted resonances in Fig.2.5. Panels(a, b) have similar contours of the dark-bright resonance. However, the interval between blue and red loops is eliminated because the increasing δ gives rise to the extra tolerance of the detuning shift from the averaged form of XPM. The purple dot marks the stability of $\mu = 0$ mode, and the round blue and red dots are associated with the emergence of steady-state solitons in (c, d). Here, we focus on the soliton-cw states, i.e. how the soliton families will react to the scan in the counterpart field. The numbers $'1,4,6'$ indicate the structure periodicity within the ring. For example, the number of $'4,6'$ marks the period of $2\pi/4, 2\pi/6$ in the resonator as displayed in Fig.2.6 (a, c) and (b, d), respectively. The black dashed curves in Fig.2.5(c, d) exhibit the soliton-cw state existence when $\varepsilon/2\pi < \varepsilon_{th}^{(1)}$ or $\varepsilon/2\pi > \varepsilon_{th}^{(2)}$, and the non-existence ranges are shaded in grey. The blue and red loops are the zoomed parts associated with Fig.2.5 (a, b), which locate the soliton-cw families. The blue and red dots marks the thresholds $\varepsilon_{th}^{(1,2)}$. Note the ending point of solutions at blue dot on the left blue loop in (d) indicates the maximal detuning shift provided by g^-. It shows for the same soliton-cw state, the g^- on the right red loop should end at the same energy level. The right-side soliton-cw state near the red curve will go through the turning point (near the red dot) due to the tilted resonance in this nonlinear system. In Fig.2.5 (e), we collect the maximal amplitude of the single-peak soliton family with both stopping points at the same level around $|\psi|^2_{max} \approx 20$ Watts. The identification of the stability for the cw-cw resonance solutions is crucial, as the frequency comb occurs in the course of sideband excitations. In Fig.2.5 (f), the positive $Re(\lambda)$ presents the maximal instability by selecting $\mu = 0$ or $\mu \neq 0$ modes (always choose the larger one). The sharp turning curves, for example, the red dashed line at $\varepsilon/2\pi \approx 3MHz$, is the consequence of the switch between maximal instability of different mode numbers. The stable region $Re(\lambda) < 0$ displays the detuning range of low-intensity cw-cw states which roughly estimate the range for soliton combs.

The stability of the soliton-cw states should be considered in a more deterministic approach by checking the MI eigenvalues where the positive number should associate with the excitation of extra modes. In Fig.2.7, when the instability exists, i.e. the blue and green

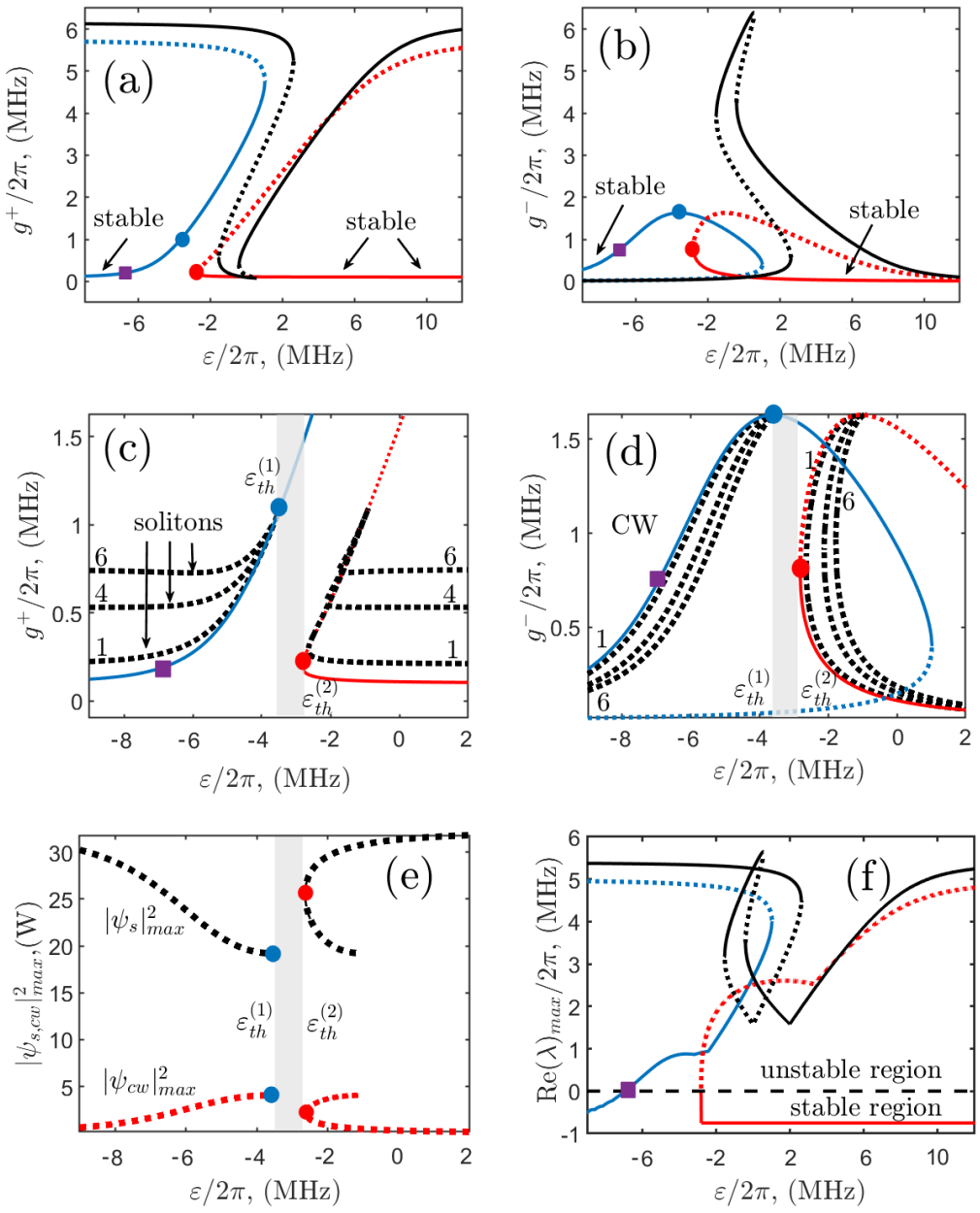

Fig. 2.5 (a, b) Nonlinear resonances are solved with fixed δ at 6MHz. The blue and red dots are associated with the soliton threshold in (c, d). The purple square is the emergence of instability in mode $\mu = 0$. (c, d) The existence of 1-, 4-, and 6-peak soliton families in the $'+'$ component. (e) The maximal intensity of 1-peak soliton solutions along the scan. (f) The full eigenvalues of the cw-cw solutions are computed by Jacobian.

points, they will certainly lead to the formation of soliton breather states with different

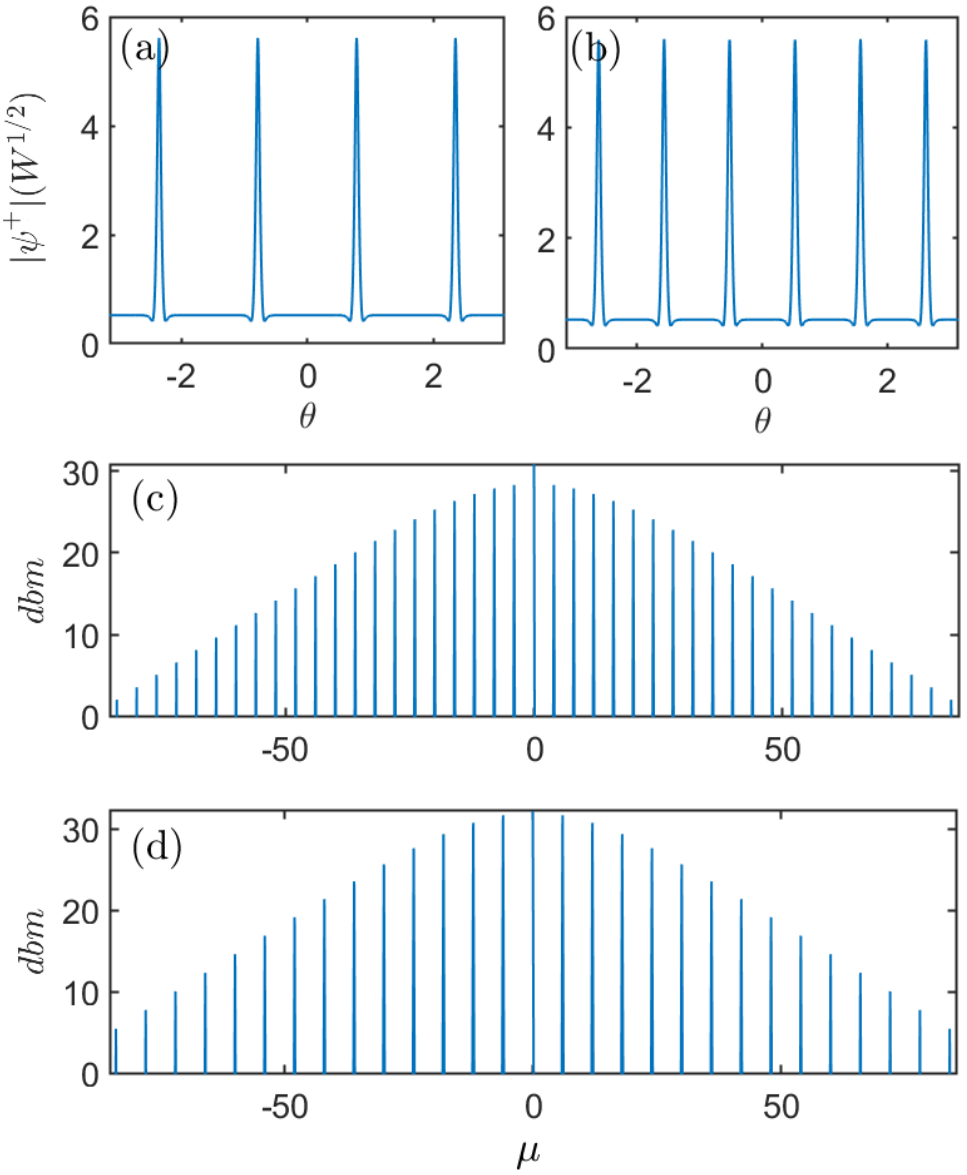

Fig. 2.6 Typical examples of 4-, 6-peak solitons are displayed in spatial profiles (a, b) and corresponding spectrums (c, d).

periods (see (c2, d2)). $\lambda = 0$ implies the self-stabilization of weakly perturbed systems (see (b2)).

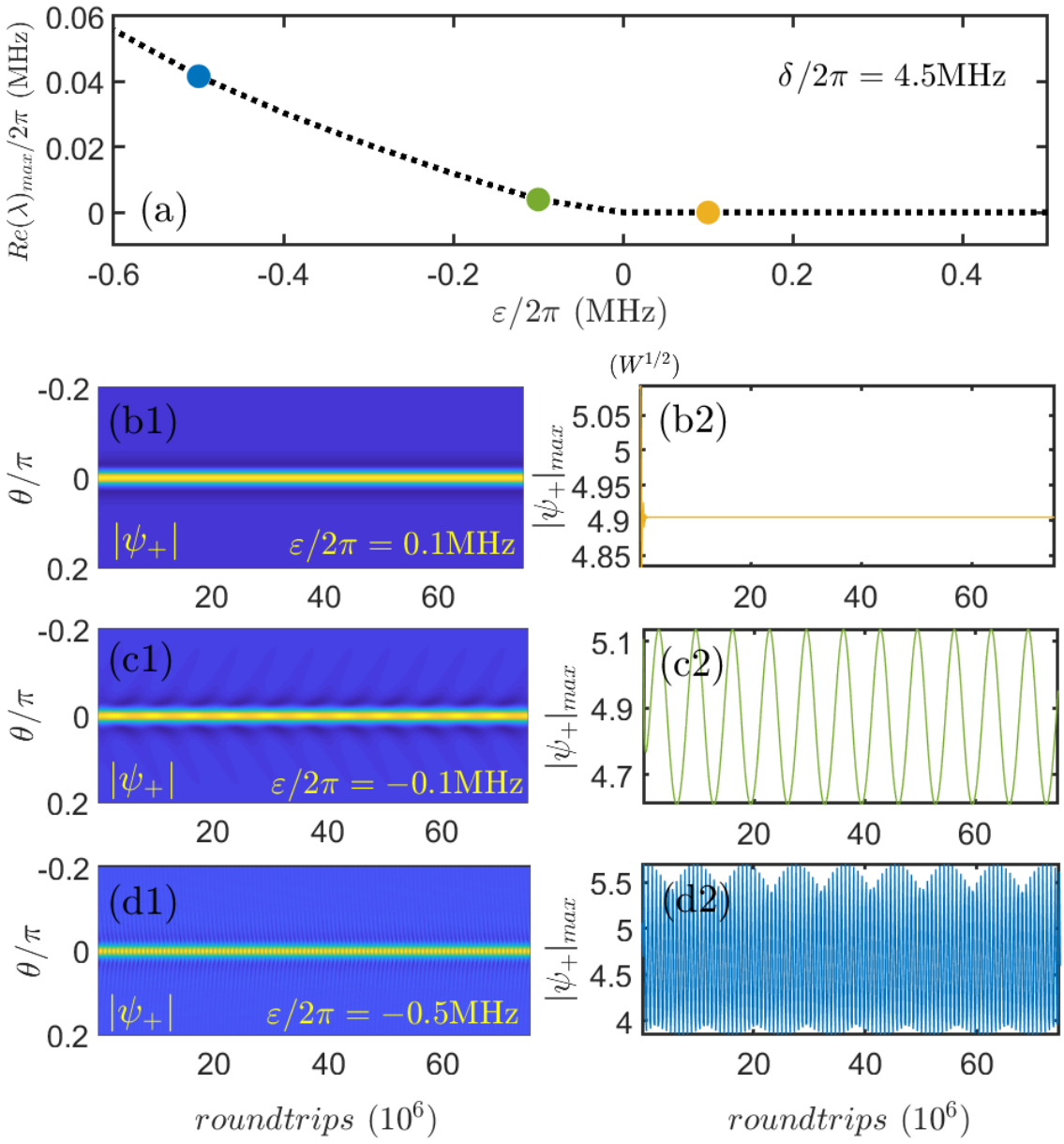

Fig. 2.7 (a) The maximal growth rates are solved for single-peak soliton. (b1, c1, d1) Dynamical simulations are checked for the yellow, green and blue dots separately. (b2, c2, d2) The maximal amplitudes are recorded with respect to the dynamics on the left side. The oscillations imply the breathers in the last two cases [16].

2.4 Soliton control by the counter-rotating field

In the previous section, we studied the soliton blockade effect impacted by nonlinear cross-coupling between the bidirectional lights. The steady-state solutions should also be captured

in real-time dynamics. In the following, the real-time scans will consolidate the observations and provide extra informations on how the instability crashes the solitons and the realization of the soliton blockade.

We start from the case with a wide blockade interval at $\delta/2\pi = 4.5MHz$. In Fig.2.8, the dynamical scan is implemented by increasing ε slowly from the negative to the positive side, crossing through the resonance in the $'-'$ field. Here, we capture the same range as in the presentation for steady states above. The solitons are generated by seeding the laser in either unstable high-intensity cw-cw states with tiny perturbations. The unstable modes will be effectively excited in the process of the cascaded frequency conversions, creating frequency combs. The solitons are generated and keep stable in Fig.2.8 (a1) when $\varepsilon/2\pi < -5MHz$. Soon, the instability of $\mu = 0$ initiates background oscillations that do not clearly impact the soliton cores. The frequency of the oscillations is measured in the order of 10 to 100kHz, and it implies the bidirectional waves are becoming unlocked from the pump frequencies. $\mu \neq 0$ instability is the deterministic factor leading to the destruction of solitons, turning the solitons into chaotic states. In Fig.2.3 (f, g), the blockade interval indicates the solitons will be forbidden due to the large nonlinear shift acts on the $'+'$ wave. In the real-time dynamics, it indeed displays such a region but with a much wider range. This should be associated with generating solitons in the $'-'$ wave as per panel (c1). It presents how the solitons emerge from cw states with the integral energy recorded in purple. Comparing the purple and blue curves $g^{\pm}$ at $\varepsilon/2\pi < -4MHz$, it demonstrates the good match between steady soliton-cw states (in Fig.2.6) and the dynamical counterpart. When ε is approaching the resonance in $'-'$ wave, the instability crashes the soliton-cw states. Therefore, the initial soliton-cw states will become chaos-soliton states, and such a regime will stop until the sweeping frequency in ω_{-} is beyond the peak of resonance where one can observe the sudden drop of the energy. The sharply declined energy will restore the effective detuning for the $'+'$ wave, which constructs the solitons at $\varepsilon/2\pi \approx 7MHz$. The above scan is implemented by decreasing ω_{-} with fixed ω_{+}. Aside from this operation, the emergence of turbulences depends on the stability of low-intensity cw states makes the opposite scans valuable. From the cw-cw states in Fig.2.3 (f, g), the low-intensity states in solid red can keep stable from $\varepsilon/2\pi \approx -1MHz$, making a narrower blockade interval from the hypothesis.

In Fig2.8(a2), the backward scan leads to the narrower blockade region due to the long existence of stable background in the soliton component. It secures the resonant detuning in soliton component from roughly $\varepsilon/2\pi \approx 0$ and above. Similarly, the soliton blockade will happen when the laser scans within the interval between left- and right-side resonant states. Both components will stabilize themselves when ε sweeps into the stable background regime; see the green dot in Fig.2.3(f, g).

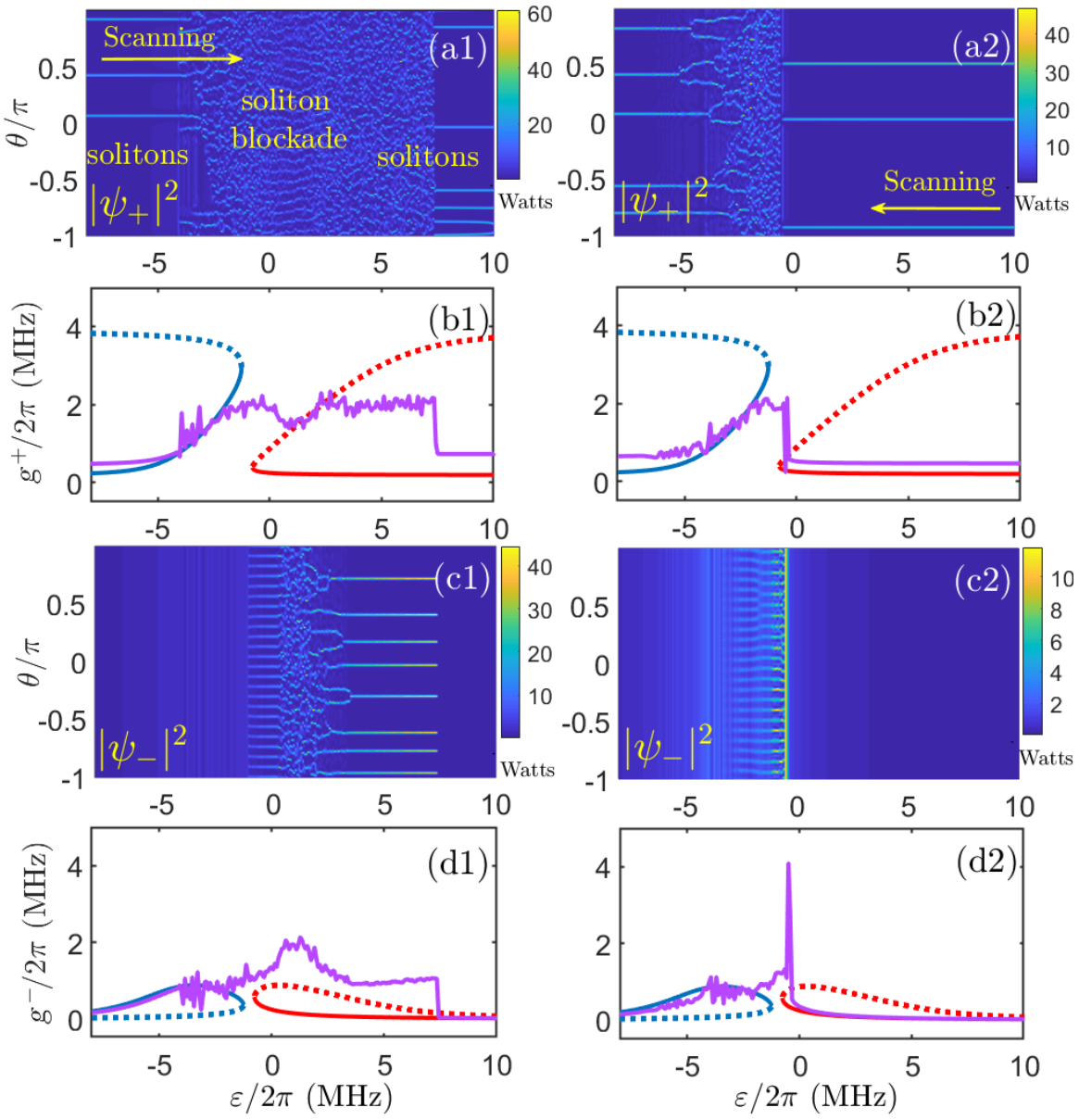

Fig. 2.8 Dynamical scans regarding the steady states are presented in Fig2.3. (a1-d1) shows the forward scan with increasing ε. The purple lines in (b1, d1) are the integral energy calculated from dynamics. The cw-cw states are marked as the label for the comparison. (a2-d2) shows the backward scan with a narrower blockade range.

The last subsection exhibits the steady cw-cw nonlinear responses when the fixed detuning δ rises to 6MHz. The blockade interval is shrinking by the decline of power in the g^- component. Fig.2.9 presents the distinctive resonances in $g^{\pm}$ with $\mathscr{H}_- = 2W^{1/2}$. The relations $\varepsilon = \omega_+ - \omega_-$ and $\delta = \omega_0 - \omega_+$, give the detuning in $'-'$ wave $\delta + \varepsilon = \omega_0 - \omega_-$. To target each pair's tip, we can focus on the net detuning $\delta + \varepsilon - 2g^+$ where the three

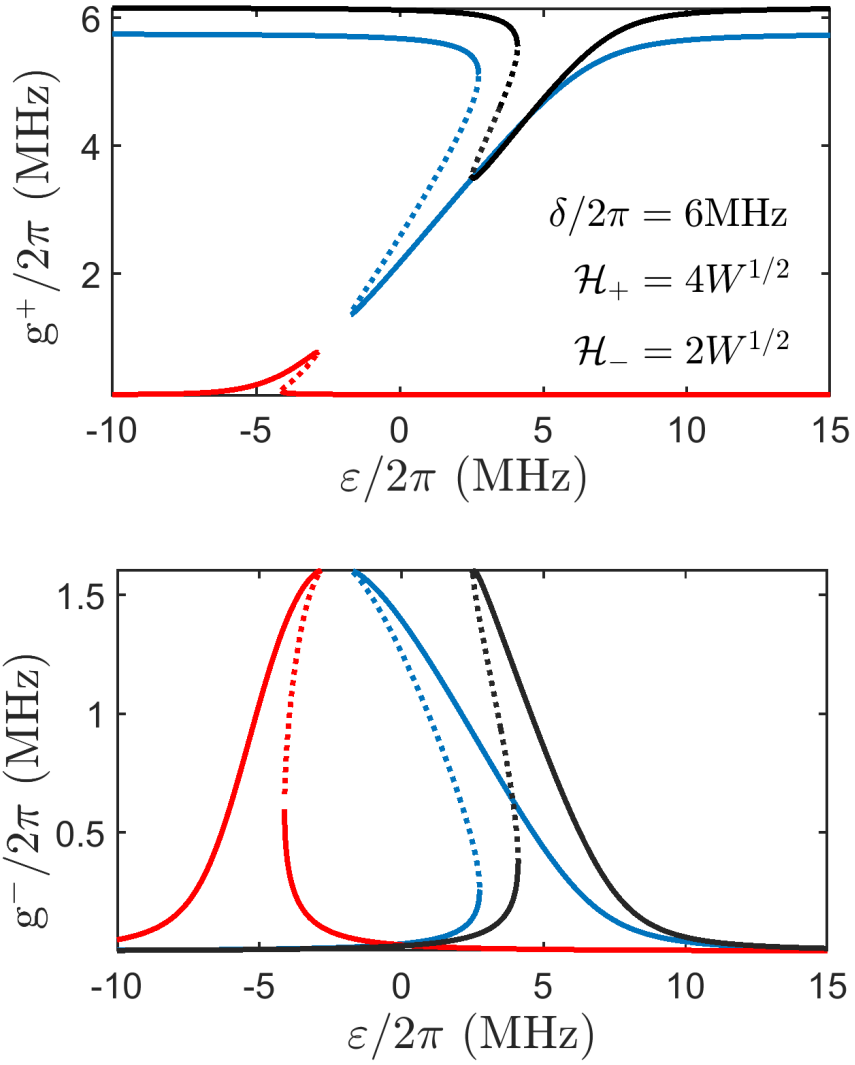

Fig. 2.9 The cw-cw states are solved under low laser power $\mathscr{H}_- = 2W^{1/2}$. The other parameters are labelled in the panels.

pairs feature the same value close to $2MHz$. Lower-intensity states are almost stable (except the short-range near $\varepsilon/2\pi \approx -5MHz$) without any interval for the soliton blockade with corresponding frequency scan in Fig.2.10. The short instability excites the periodic waves and cannot further transit into soliton states attributed to the insufficient laser power. Meanwhile, such generations with increasing power act on the $'+'$ wave, making the fade background carpet in panel(a1) near $\varepsilon/2\pi \approx -4.5$MHz.

Another non-trivial case is pumping the resonator with strong laser power of $\mathscr{H}_-$, as the extended bistability resonance in $'-'$ field will form the soliton-soliton states. The dynamical

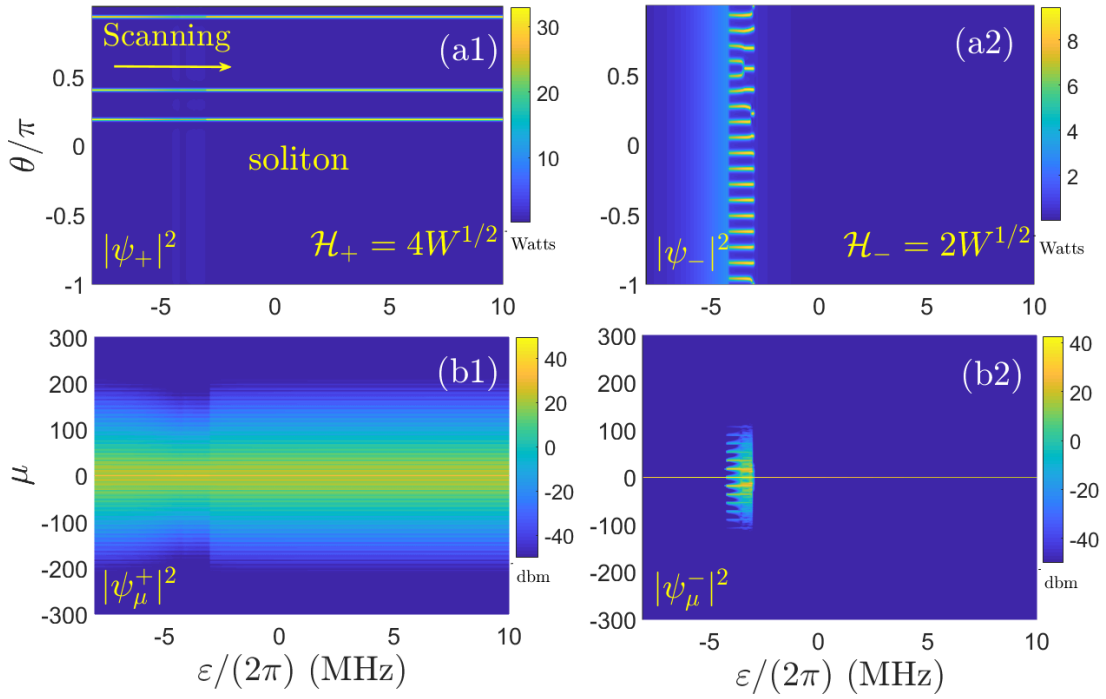

Fig. 2.10 The dynamical simulation corresponds to the case in Fig.2.9, where the soliton blockade can be avoided with decreasing laser power in the $'-'$ wave.

scan in Fig.2.11 (a1) presents the process of soliton, soliton blockade, and soliton as predicted. The CCW field displays the transition from cw states into solitons. The restoration of solitons from chaos in (a1) is achieved with the help of energy drop when solitons are formed in (a2). The blockade point $g_-^{(1)} \approx 1.2MHz$ in panel (d) is labelled. When the solitons are generated from chaos area, g_- will decrease to $1MHz$, accounting for the solitons restoration in the $'+'$ field.

The idea of controlling frequency combs in the high finesse bidirectional system emerges from the blockade effect, where the laser-cavity detuning and power are two main factors. The tolerance of XPM shift for a frequency comb should depend on the fixed detuning, and the laser power may directly control the strength of such shifts. In Fig.2.12 (a), the blockade range with equal pump powers has been addressed. The blockade interval is shrinking with growing fixed δ, and the exact detuning for the scanning laser in $'-'$ component should be $\delta + \varepsilon$. The blockade range can be justified by either of the criterion. The first path implements the forward and backward scans simultaneously and records the overlapped blockade region as the forbidden range shaded in grey. Alternatively, we can take the steady state formulas and compute the soliton families as shown in Fig.2.4 (c). Both methods are identified to be

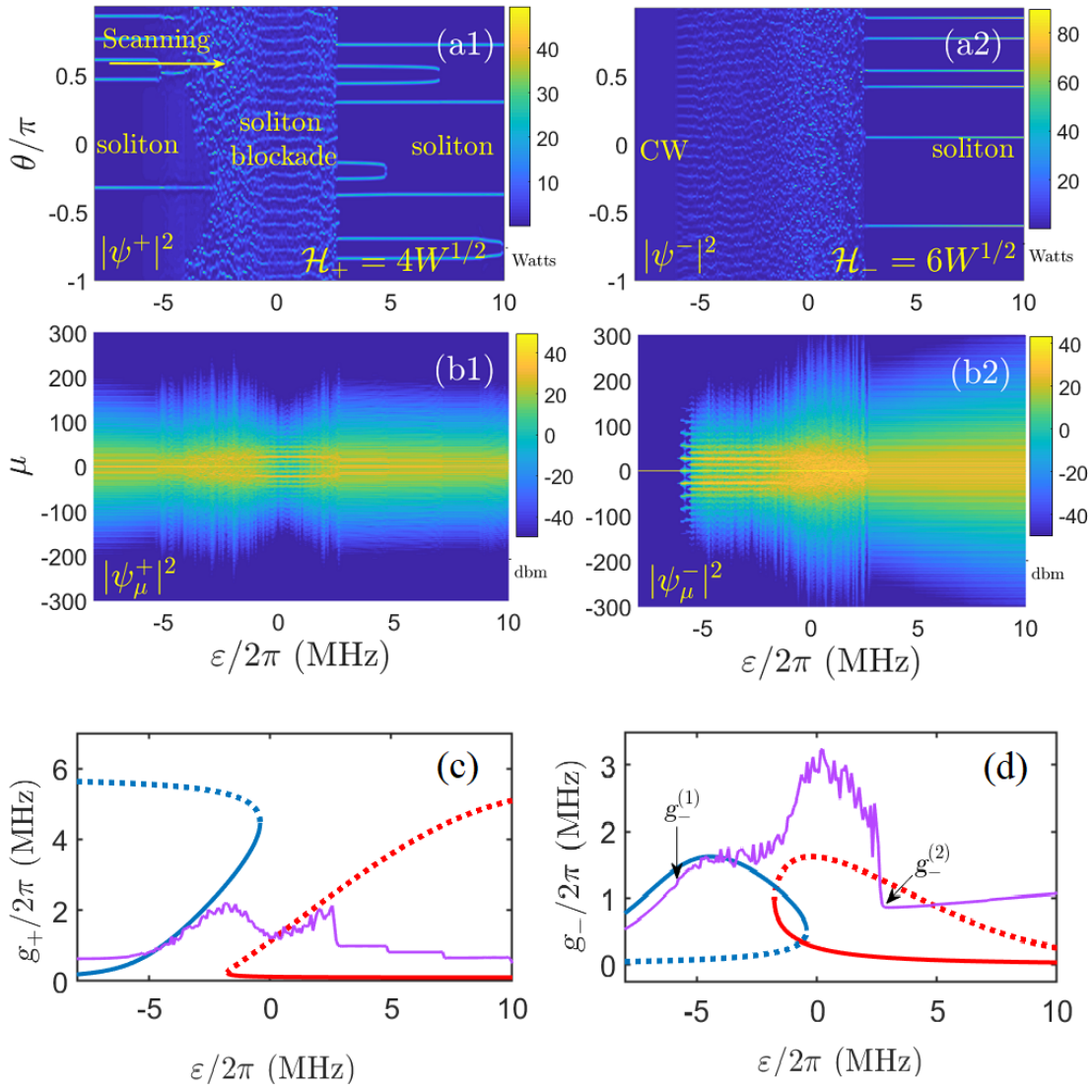

Fig. 2.11 Enhanced power $\mathscr{H}_- = 6W^{1/2}$ is taken for the extended soliton formation in the CCW component. In panel(d), the intensity threshold $g_-^{(1)}$ labels the critical level for the soliton blockade in the CW core. $g_-^{(2)}$ shows the intensity in the CCW wave when solitons are generated. $\delta = 6$MHz is fixed.

equivalent and match the dynamical scans in Fig.2.8. Here, the limitation of δ is from the detuning for maximal resonance at $\delta/2\pi \approx 6.4MHz$ with the assumption $g^- = 0$. Fig.2.9 (b), on the contrary, reflects the blockade interval controlled by the modulation of laser powers. Observing the strengthened blockade effect with incremental energy coming into the $'-'$ wave is more intuitive.

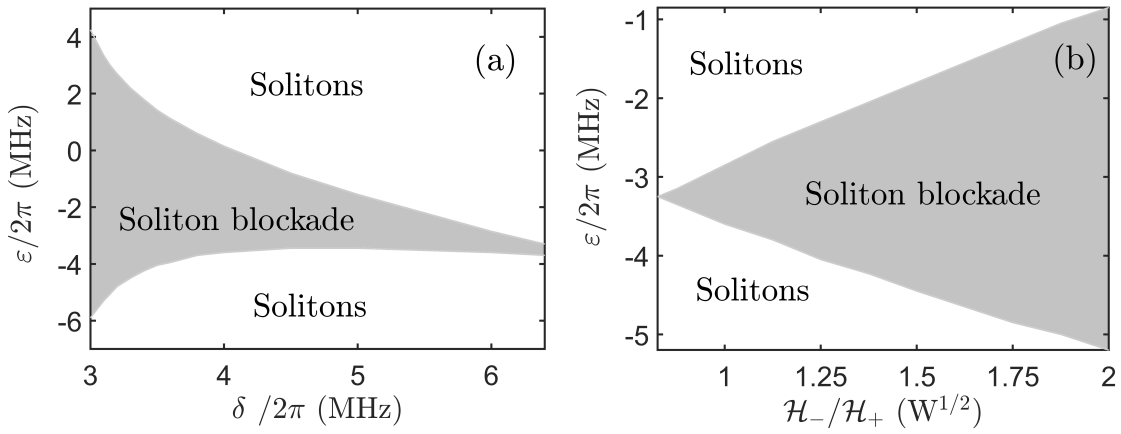

Fig. 2.12 Soliton blockade management is controlled through different fixed detunings (a) and the pump powers (b). Fixed parameters: (a) Same pumps are taken at $\mathscr{H}_\pm = 4W^{1/2}$; (b) $\delta/2\pi = 6$MHz.

2.5 Instability tongues

In the high Q microresonator, the finesse dispersion D_2/κ will split the instability areas into a set of partially overlapped tongue-like structures [17], which is crucial for the understanding of the formation of Turing patterns and crystals of light. In the following, we will extend the theory to the two-component regime.

Take the similar model introduced above:

$$i\partial_t\psi^+ = \delta_+\psi^+ - \frac{D_2}{2}\partial_\theta^2\psi^+ - R\psi^- - i\frac{\kappa}{2}(\psi^+ - \mathscr{H}_+) - \gamma|\psi^+|^2\psi^+ - 2\sigma\gamma\psi^+\int_0^{2\pi}|\psi^-|^2\frac{d\theta}{2\pi} \tag{2.26}$$

$$i\partial_t\psi^- = \delta_-\psi^- - \frac{D_2}{2}\partial_\theta^2\psi^- - R\psi^+ - i\frac{\kappa}{2}(\psi^- - \mathscr{H}_-) - \gamma|\psi^-|^2\psi^- - 2\sigma\gamma\psi^-\int_0^{2\pi}|\psi^+|^2\frac{d\theta}{2\pi} \tag{2.27}$$

Regarding the two new symbols, $\sigma = 1$ means the bidirectional waves in a single resonator, and R is the backscattered coupling between the counter-rotating waves. The other case, $\sigma = 0$, accounts for the double-ring system, and R is the coupling rate between the two rings. The MI assumes the slight perturbations adding to the zero modes with the substitution $\psi^\pm = A_0^\pm + \rho^\pm$ ($A_0^\pm$ and and $\rho^\pm$ are the stationary solutions and perturbations):

$$i\partial_t\vec{\rho} = \begin{bmatrix} \Delta_\mu^+ - i\frac{\kappa}{2} & -\gamma(A_0^+)^2 & -R-\sigma\hat{\delta}_{\mu,0}2\gamma A_0^+A_0^{-*} & -\sigma\hat{\delta}_{\mu,0}2\gamma A_0^+A_0^- \\ \gamma(A_0^{+*})^2 & -\Delta_{-\mu}^+ - i\frac{\kappa}{2} & \sigma\hat{\delta}_{\mu,0}2\gamma A_0^{+*}A_0^{-*} & R+\sigma\hat{\delta}_{\mu,0}2\gamma A_0^{+*}A_0^- \\ -R-\sigma\hat{\delta}_{\mu,0}2\gamma A_0^{+*}A_0^- & -\sigma\hat{\delta}_{\mu,0}2\gamma A_0^+A_0^- & \Delta_\mu^- - i\frac{\kappa}{2} & -\gamma(A_0^-)^2 \\ \sigma\hat{\delta}_{\mu,0}2\gamma A_0^{+*}A_0^{-*} & R+\sigma\hat{\delta}_{\mu,0}2\gamma A_0^+A_0^{-*} & \gamma(A_0^{-*})^2 & -\Delta_{-\mu}^- - i\frac{\kappa}{2} \end{bmatrix}\vec{\rho}$$

$$i\partial_t\vec{\rho} = \hat{M}\vec{\rho}, \vec{\rho} = \vec{\rho}_0 e^{\lambda t} \tag{2.28}$$

$$(\hat{M} - i\lambda\hat{I})\vec{\rho}_0 = 0 \tag{2.29}$$

where the kernels are:

$$\Delta_\mu^+ = \delta_+ + \frac{1}{2}D_2\mu^2 - 2\gamma(|A_0^+|^2 + \sigma|A_0^-|^2) \tag{2.30}$$

$$\Delta_{-\mu}^+ = \delta_+ + \frac{1}{2}D_2\mu^2 - 2\gamma(|A_0^+|^2 + \sigma|A_0^-|^2) \tag{2.31}$$

$$\Delta_\mu^- = \delta_- + \frac{1}{2}D_2\mu^2 - 2\gamma(\sigma|A_0^+|^2 + |A_0^-|^2) \tag{2.32}$$

$$\Delta_{-\mu}^- = \delta_- + \frac{1}{2}D_2\mu^2 - 2\gamma(\sigma|A_0^+|^2 + |A_0^-|^2) \tag{2.33}$$

See ρ_0 expressions in Eqs.(A.30, A.31). μ is the relative mode index which centralized for pump mode (i.e., $\mu = 0$), and the sideband modes are counting from $\mu = \pm1, \pm2, \pm3, \cdots$. Assuming symmetric case ($\delta_+ = \delta_-, A_0^+ = A_0^- = A_0$), the matrix will be factorized by introducing eigenstates $\vec{\rho}_0 = [w, -v, w, -v]^T$ as in-phase eigenstates (where $A_\mu^\pm$ have same perturbations), and $\vec{\rho}_0 = [w, -v, -w, v]^T$ as out-phase eigenstates (where $A_\mu^\pm$ have opposite perturbations). They solve the eigenvalues λ_{in} and λ_{out} below:

$$[\Delta - R + \gamma|A_0|^2][\Delta - R - (1 + 4\sigma\hat{\delta}_{\mu,0})\gamma|A_0|^2] = -(\frac{\kappa}{2} + \lambda_{in})^2 \tag{2.34}$$

$$[\Delta + R + (1 + 2\sigma\hat{\delta}_{\mu,0})\gamma|A_0|^2][\Delta + R + (-1 + 2\sigma\hat{\delta}_{\mu,0})\gamma|A_0|^2] = -(\frac{\kappa}{2} + \lambda_{out})^2 \tag{2.35}$$

In the symmetric regime ($A_0^+ = A_0^-$), $\Delta_\pm = \Delta$. The Kronecker delta $\hat{\delta}_{\mu,0}$ returns 1 when $\mu = 0$. $\sigma = 1$ for the single ring with bidirectional fields; $\sigma = 0$ for two coupled rings with unidirectional waves in each ring. Open the capital delta term by defining

$\Delta = \Delta_\mu - 2\gamma(|A_0|^2 + \sigma|A_0|^2)$, $\Delta_\mu = \delta + \frac{1}{2}D_2\mu^2$ and $g = \gamma|A_0|^2$, Eqs.(2.34, 2.35) can be written as:

$$[\Delta_\mu - R - (1+2\sigma)g][\Delta_\mu - R - (3+2\sigma+4\sigma\hat{\delta}_{\mu,0})g] = -(\frac{\kappa}{2} + \lambda_{in})^2 \tag{2.36}$$

$$[\Delta_\mu + R - (1+2\sigma-2\sigma\hat{\delta}_{\mu,0})g][\Delta_\mu + R - (3+2\sigma-2\sigma\hat{\delta}_{\mu,0})g] = -(\frac{\kappa}{2} + \lambda_{out})^2 \tag{2.37}$$

Eqs.(2.36, 2.37) yield the two pairs of eigenvalues, and the set of the in-phase and out-phase perturbations can be regarded as two eigenmodes of the system, each having its own stability threshold.
Firstly, by taking $\sigma = 1$, the in-phase eigenstates are:

$$\lambda_{in}(\lambda_{in} + \kappa) = (15 + 12\hat{\delta}_{\mu,0})(g - g_{in}^{(1)})(g_{in}^{(2)} - g) \tag{2.38}$$

$$g_{in}^{(1,2)} = \frac{(4+2\hat{\delta})a_{in}}{15+12\hat{\delta}} \pm \frac{\sqrt{(4+32\hat{\delta})a_{in}^2 - (15+12\hat{\delta})\kappa^2}}{30+24\hat{\delta}} \tag{2.39}$$

$$a_{in} = \Delta_\mu - R \tag{2.40}$$

and out-phase case is:

$$\lambda_{out}(\lambda_{out} + \kappa) = (15 - 12\hat{\delta}_{\mu,0})(g - g_{out}^{(1)})(g_{out}^{(2)} - g) \tag{2.41}$$

$$g_{out}^{(1,2)} = \frac{(4-2\hat{\delta})a_{out}}{15-12\hat{\delta}} \pm \frac{\sqrt{4a_{out}^2 - (15-12\hat{\delta})\kappa^2}}{30-24\hat{\delta}} \tag{2.42}$$

$$a_{out} = \Delta_\mu + R \tag{2.43}$$

The maximal instability occurs under the condition of $\partial_\mu\lambda_\mu = 0, \partial_\delta\lambda_\mu = 0$, which can be reduced to $\partial_\mu g_\mu^{(1,2)} = 0, \partial_\delta g_\mu^{(1,2)} = 0$. Only $\partial_{\mu,\delta} g^{(2)}$ returns meaningful solution (no extremum exists in the other selection):
For $\partial_\mu g_{in,\mu}^{(2)} = 0, \partial_\delta g_{in,\mu}^{(2)} = 0$

$$\Delta_\mu = (2-\hat{\delta})\kappa + R; \;\; g_{in,\mu}^{(2)} = \frac{\kappa}{2+4\hat{\delta}} \tag{2.44}$$

For $\partial_\mu g^{(2)}_{out,\mu} = 0, \partial_\delta g^{(2)}_{out,\mu} = 0$

$$\Delta_\mu = (2-\hat{\delta})\kappa - R; \;\; g^{(2)}_{out,\mu} = \frac{\kappa}{2} \tag{2.45}$$

The relation of $\Delta_\mu = (2-\hat{\delta})\kappa \pm R$ makes a set of critical pump frequencies (recall $\Delta_\mu = \delta + \frac{1}{2}D_2\mu^2$):

$$\omega_p^{\mu L,in} = \omega_0 + \frac{1}{2}D_2\mu^2 - [(2-\hat{\delta})\kappa + R], \tag{2.46}$$

$$\omega_p^{\mu L,out} = \omega_0 + \frac{1}{2}D_2\mu^2 - [(2-\hat{\delta})\kappa - R] \tag{2.47}$$

where $\omega_p^{\mu L,in/out}$ are a pair of pump frequencies satisfying the threshold condition. Accordingly, the thresholds of the intracavity power can be derived below.

The symmetric homogeneous solutions are obtained at $\mu = 0$:

$$\frac{4g}{\kappa^2}(\delta - R - 3g)^2 + g = \gamma\mathscr{H}^2 \tag{2.48}$$

For the in-phase case, we substitute $g \to g^{(2)}_{in}$ and $\delta \to \delta^{\mu L}_{in}$:

$$\frac{\kappa}{2+4\hat{\delta}}[1 + \frac{4}{\kappa^2}(\delta^{\mu L}_{in} - R - \frac{3\kappa}{2+4\hat{\delta}})^2] = \gamma\mathscr{H}^2_{\mu L,in} \tag{2.49}$$

$$\delta^{\mu L}_{in} = \omega_0 - \omega_p^{\mu L,in} \tag{2.50}$$

For the out-phase case, we substitute $g \to g^{(2)}_{out}$ and $\delta \to \delta^{\mu L}_{out}$:

$$\frac{\kappa}{2}[1 + \frac{4}{\kappa^2}(\delta^{\mu L}_{out} - R - \frac{3\kappa}{2})^2] = \gamma\mathscr{H}^2_{\mu L,out} \tag{2.51}$$

$$\delta^{\mu L}_{out} = \omega_0 - \omega_p^{\mu L,out} \tag{2.52}$$

Here, $\mathscr{H}_{\mu L,in}$ and $\mathscr{H}_{\mu L,out}$ are the thresholds of the power for an excited mode μ from cw branch. The above critical relations show the instability structures are determined by dispersion D_2 and R in the panel of $(\delta, g_{in,out})$.

In Fig.2.13, the instability threshold for dense and sparse cases are controlled by the dispersion coefficient D_2. Here, the black contour is the threshold for the pump mode $\mu = 0$. The lower and upper edges in g_{in}, g_{out} with fixed detuning are given by the two roots in Eq.(2.40) and Eq.(2.43), respectively. The green and purple dashed lines are marked in line with Eqs.(2.44,2.45). When $R = 0$, there is no splitting of the tongues in g_{in} and g_{out} for

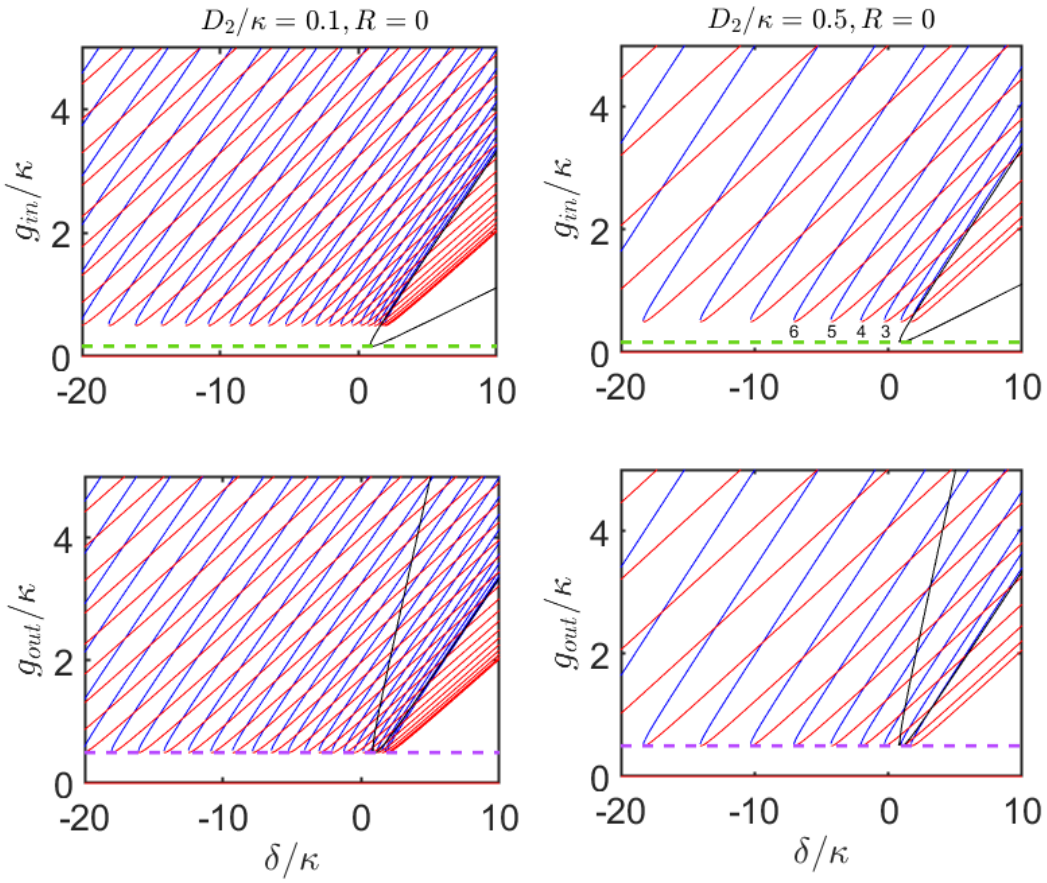

Fig. 2.13 Instability tongue-like structures with low and high dispersion $D_2 = 0.1, 0.5$, separately. The green and purple dashed lines are the rulers for levels of $1/6, 1/2$. $\gamma = 1$ is fixed, and $\mu = 0$ is contoured by the black line.

$\mu \neq 0$. The tongue-like contours present the instability range. The order of tongue indices marks the instability region for specific mode μ. For instance, the numbers $\mu = 3$ to 6 are labelled. In either case, the crossings between two tongues will give rise to the multiple mode instability and the Turing patterns whose periodicity of m can be found at the tip of the corresponding tongue with the same index. In Fig.2.14, we demonstrate the effect of tongue splitting with $R \neq 0$. The top panel implies the introduction of R will linearly shift the instability tongues, whereas the splitting of g_{in} and g_{out} as given in the bottom panel will be $2R$ (the spacing between the black tip and cyan tip from the same tongue). As the

eigenstates of in-phase and out-phase mark the two boundaries of instability tongue, i.e., any perturbations which can be factorized into such eigenstates should sit between the two extreme thresholds.

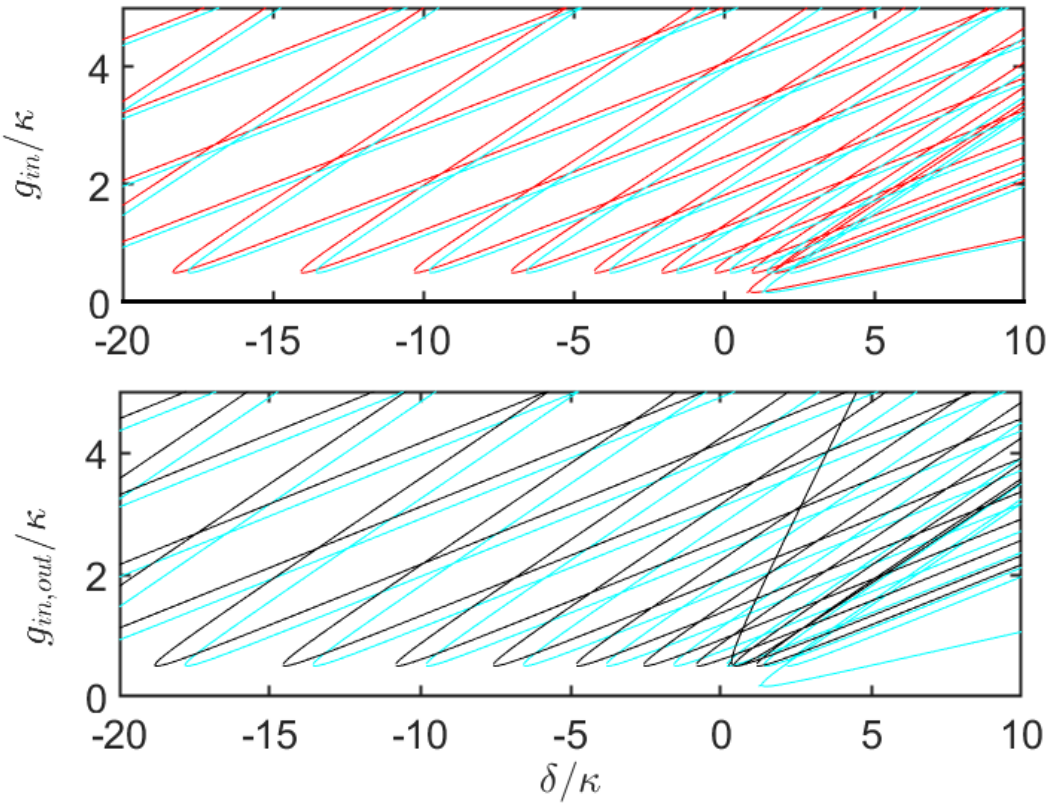

Fig. 2.14 Top panel compares g_{in} with $R = 0$ (red) and $R = 0.5$ (cyan) with same $D_2 = 0.5$. Bottom panel compares g_{in} (cyan) and g_{out} (red) with $R = 0.5$.

Following the same approach, the other case with $\sigma = 0$ can be treated in the similar analysis:

$$\lambda_{in}(\lambda_{in} + \kappa) = 3(g - g_{in}^{(1)})(g_{in}^{(2)} - g) \tag{2.53}$$

$$g_{in}^{(1,2)} = \frac{2a_{in}}{3} \pm \frac{\sqrt{a_{in}^2 - \frac{3}{4}\kappa^2}}{3} \tag{2.54}$$

$$a_{in} = \Delta_\mu - R \tag{2.55}$$

The out-phase regime will have similar form due to the symmetry of two rings:

$$\lambda_{out}(\lambda_{out} + \kappa) = 3(g - g_{out}^{(1)})(g_{out}^{(2)} - g) \tag{2.56}$$

$$g_{out}^{(1,2)} = \frac{2a_{out}}{3} \pm \frac{\sqrt{a_{out}^2 - \frac{3}{4}\kappa^2}}{3} \tag{2.57}$$

$$a_{out} = \Delta_\mu + R \tag{2.58}$$

where kernels $a_{in,out}$ imply the coupling between them will break the degeneracy.

The maximal instability can be sought by $\partial_\mu g_\mu^{(1,2)} = 0, \partial_\delta g_\mu^{(1,2)} = 0$. Similarly, only $\partial_{\mu,\delta} g^{(2)}$ returns extremum:

For $\partial_\mu g_{in,\mu}^{(2)} = 0, \partial_\delta g_{in,\mu}^{(2)} = 0$

$$\Delta_\mu = \kappa + R; \;\; g_{in,\mu}^{(2)} = \frac{\kappa}{2} \tag{2.59}$$

For $\partial_\mu g_{out,\mu}^{(2)} = 0, \partial_\delta g_{out,\mu}^{(2)} = 0$

$$\Delta_\mu = \kappa - R; \;\; g_{out,\mu}^{(2)} = \frac{\kappa}{2} \tag{2.60}$$

The relation of $\Delta_\mu = \kappa \pm R$ indicates a set of pump frequencies:

$$\omega_p^{\mu L,in} = \omega_0 + \frac{1}{2} D_2 \mu^2 - (\kappa + R), \tag{2.61}$$

$$\omega_p^{\mu L,out} = \omega_0 + \frac{1}{2} D_2 \mu^2 - (\kappa - R) \tag{2.62}$$

where $\omega_p^{\mu L,in/out}$ are pump frequencies under instability threshold conditions.

By comparing the threshold conditions Eqs.(2.39, 2.42) and Eqs.(2.54, 2.57), the zero mode instability threshold affected by nonlinearity is different, see Fig.2.13. When $\sigma = 0$, the nonlinearity in each ring is reduced to the self-phase modulation. From Eqs.(2.59, 2.60), the minimal threshold $g_{in/out,\mu}^{(2)}$ becomes uniform for all modes. In addition, the tongue splitting is solely impacted by the coupling rate R. The complexity of the system can be further reduced when $R = 0$ is taken, and it shows equivalence to the single component Kerr resonator, which has been extensively discussed in our recent work [17].

2.6 Conclusion

In this chapter, we started with the model of a bidirectional microresonator under the high finesse condition. The counterrotating group velocity terms are treated as the fast oscillating phases and thus can be averaged out. The applied mode restrictions effectively shape the cross-phase modulations into an integral form, serving as additional detuning shifts. We

have studied the homogeneous solutions and the stability under two regimes: firstly, we have discussed the cases under fixed offsets between two pump frequencies varying in the same scanning rate where symmetric and symmetry-breaking states are captured. Secondly, the resonances formed by scanning with one laser have been introduced. Under such a regime, we found the blockade regions of soliton combs. Soliton blockade effect has been further discussed in the dynamical simulations under various conditions and identified to match the existing steady-state soliton families. Controlling the soliton frequency combs through the frequency scans forwardly and backwardly is associated with the gap between low-intensity states, as well as the stability of the cw background. At the end of this topic, we provided the theory of the soliton blockade effect through either frequency or laser power scans. The additional discussions about the stability thresholds in two-component resonators provided significant insights into the frequency conversion conditions.

References

[1] J. M. Silver, L. D. Bino, M. T. M. Woodley, G. N. Ghalanos, A. Svela, N. Moroney, S. Zhang, K. T. V. Grattan, and P. DelHaye, Nonlinear enhanced microresonator gyroscope, Optica 8, 1219-1226 (2021).

[2] Q. F. Yang, X. Yi, K. Yang, et al., Counter-propagating solitons in microresonators. Nat. Photon. 11, 560564 (2017).

[3] M. T. M. Woodley, J. M. Silver, L. Hill, F. Copie, L. D. Bino, S. Zhang, G. Oppo, and P. Del'Haye, Universal symmetry-breaking dynamics for the Kerr interaction of counterpropagating light in dielectric ring resonators, Phys. Rev. A 98, 053863 (2018).

[4] M. G. Suh, Q. F. Yang, K. Y. Yang, X. Yi, K. J. Vahala, Microresonator soliton dual-comb spectroscopy, Science 354, 600603 (2016).

[5] I. Coddington, W. Swann, L. Nenadovic, N. Newbury, Rapid and precise absolute distance measurements at long range, Nat. Photon. 3, 351356 (2009).

[6] N. Pavlov, et al., Soliton dual frequency combs in crystalline microresonators, Opt. Lett. 42, 514517 (2017).

[7] W. Weng, R. Bouchand, E. Lucas, and T. J. Kippenberg, Polychromatic Cherenkov Radiation Induced Group Velocity Symmetry Breaking in Counterpropagating Dissipative Kerr Solitons, Phys. Rev. Lett. 123, 253902 (2019).

[8] D. V. Skryabin, Hierarchy of coupled mode and envelope models for bi-directional microresonators with Kerr nonlinearity, OSA Continuum 3, 1364-1375 (2020).

[9] Ó. B. Helgason, M. Girardi, Z. Ye, F. Lei, J. Schröder and V. T. Company, Power-efficient soliton microcombs, arXiv:2202.09410 (2022).

[10] H. Weng, A. A. Afridi, J. Li, M. McDermott, H. Tu, L. P. Barry, Q. Lu, W. Guo, J. F. Donegan, Dual-mode microresonators as straightforward access to octave-spanning dissipative Kerr solitons, arXiv:2202.09786 (2022).

[11] I. Pupeza, Power Scaling of Enhancement Cavities for Nonlinear Optics, Springer (2012).

[12] A. Yariv, Critical Coupling and Its Control in Optical Waveguide-Ring Resonator Systems, IEEE Photonics Technology Letters 14, 4 (2002).

[13] M. T. M. Woodley, J. M. Silver, L. Hill, F. Copie, L. D. Bino, S. Zhang, G. Oppo, and P. Del'Haye, Universal symmetry-breaking dynamics for the Kerr interaction of counterpropagating light in dielectric ring resonators, Phys. Rev. A 98, 053863 (2018).

[14] L. D. Bino, J. Silver, S. Stebbings, et al., Symmetry Breaking of Counter-Propagating Light in a Nonlinear Resonator, Sci. Rep. 7, 43142 (2017).

[15] Z. Fan and D. V. Skryabin, Soliton blockade in bidirectional microresonators, Opt. Lett. 45, 6446-6449 (2020).

[16] Z. Fan and D. V. Skryabin, Controlling Microresonator Solitons with the Counter-Propagating Pump, Photonics 8, 239 (2021).

[17] D. V. Skryabin, Z. Fan, A. Villois, D. N. Puzyrev, Threshold of complexity and Arnold tongues in Kerr-ring microresonators, 103, L011502 (2021).

Chapter 3

Topological soliton crystals

3.1 Introduction

In this chapter, we will focus on the periodic multiple soliton states, namely, the soliton crystals. We report the observation of topology in soliton crystals where the topological chain is fully constructed through the arrangement of dissipative Kerr solitons and their relative positions are alike to the known Su-Schrieffer-Heeger (SSH) model. The geometric phase, Wannier formalism, and edge states have been included.

3.1.1 Soliton crystals and topology

The formation of dissipative Kerr solitons has been discussed in the first two chapters. In particular, we have observed the multi-soliton states (MSSs) in a bidirectional resonator. The perfect soliton crystals (PSCs) can be regarded as a special multiple soliton state where the solitons are evenly spaced in a ring resonator. Following the observation of the PSCs in a silica resonator [1], in 2019, colleagues found a deterministic generation of PSCs in a *SiN* microresonator. Distinguished from the disordered multiple soliton states, the PSCs often emerge at low pump power. The crystal formation has been attributed to the specific regions in the two-dimensional domain mapped by the detuning and the pump power [2]. The formation of crystals is often associated with the avoid-mode crossing, where one specific mode frequency has been shifted, thus leading to the modulation on the CW background serving as potential sites for the regular spacings [3]. The other works have demonstrated the on-demand positioning of soliton through pump modulation [4], dual-pumps [5], optoacoustically mode-locked laser [6] and forward and backward detuning control [7]. All these approaches and observations support our findings.

Topology classifies objects by their geometric structures. One typical example is the comparison between a mug and one doughnut, where both objects include a hole. The computation by integrating the Gaussian curvature over the surfaces returns the same number, indicating they belong to the same class, viz, one can be deformed to the other without changing the integration number [8]. This concept is widely used in physics, where some systems feature certain phases displaying unique properties as an analogy to their mathematical counterpart. The topological insulator, whose surface is metallic but the bulk portion remains insulating [9], is one of the most intriguing subjects in the last decade. Beyond the topology in the electronic condensed physics system, the recent emerging studies in the topological photonics have demonstrated their relevance for the design of high-efficiency optical devices [10], such as the waveguide arrays [11, 12], photonic crystals [13], and ring resonators [14]. In the presence of loss and gain, optical systems become non-Hermitian, leading to significant theoretical interests and new topological effects [15–17].

3.1.2 Su-Schrieffer-Heeger (SSH) model

The SSH model provides basic concepts for understanding a topological system. In Fig.3.1(a), the one-dimensional chain is composed of particles shown in red and green with strong (blue bond) and weak (orange bond) couplings with their neighbours. For the arrangement given

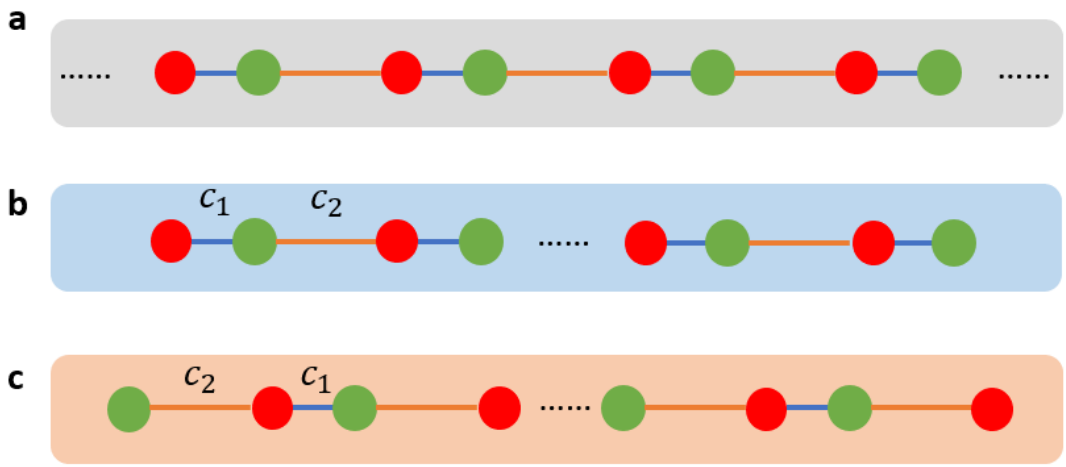

Fig. 3.1 The sketch of SSH model. The strong and weak couplings between particles are c_1, c_2, respectively.

in Fig.3.1(b) and(c), where the edge particles on the sides have strong and weak couplings to

the chain. The real-space tight-binding Hamiltonian matrix of the SSH lattice can be written as [18, 19]:

$$H_b = \begin{bmatrix} 0 & c_1 & 0 & 0 & ... & 0 \\ c_1 & 0 & c_2 & 0 & ... & 0 \\ 0 & c_2 & 0 & c_1 & ... & 0 \\ \vdots & \vdots & \vdots & \vdots & \ddots & \vdots \\ 0 & 0 & 0 & ... & c_1 & 0 \end{bmatrix}, H_c = \begin{bmatrix} 0 & c_2 & 0 & 0 & ... & 0 \\ c_2 & 0 & c_1 & 0 & ... & 0 \\ 0 & c_1 & 0 & c_2 & ... & 0 \\ \vdots & \vdots & \vdots & \vdots & \ddots & \vdots \\ 0 & 0 & 0 & ... & c_2 & 0 \end{bmatrix} \tag{3.1}$$

The eigenvalues and eigenfunctions are solved with a set of coupling strengths of c_1, c_2 $(c_1 > c_2)$. Fig.3.2 (a) shows the band spectrum of H_b, H_c with 60 different relative couplings. The spectrum show that the edge states emerge when two edge particles have weak coupling to the rest of the chain, coinciding with the arrangement in Fig.3.1 (c). The typical edge state distribution in Fig.3.2 (d) is given. Such isolated eigenstates can exist when the system is in the non-trivial topological status coloured by red carpet in Fig.3.2 (a).

Further discussion of geometric phase, etc., will be included in the main section. This discussion makes a brief impression on the relation between the arrangement of lattice and the edge states. Even though this model is linear, it still provides significant insights into the following discussion about the topological soliton crystals sustained by nonlinearity.

3.2 Atomic and molecular soliton crystals

Soliton crystals can be divided into two categories, i.e., atomic soliton crystals (ASCs) and molecular soliton crystals (MSCs), whose periods are π/K (K is the number of solitons) and $2\pi/K$. In either case, the study of such periodic structures takes great benefits from the Bloch theorem.

3.2.1 Unit cells and Bloch states

The atomic and molecular families diagrams are displayed in Fig.3.3. Panel (a) shows the atomic crystal with the period of π/K. For molecular case, such period is $2\pi/K$ and panels (b,c) show two possible choices of unit cells named 'Unit cell A' and 'Unit cell B'. The soliton crystals envelope ϕ obeys the Lugiato-Lefever equation in the moving reference frame:

$$i\partial_t \phi = (\omega_0 - \omega_p)\phi + \sum_{j=1}^{3} \frac{d_j}{j!}(-i\partial_\theta)^j \phi - \gamma|\phi|^2\phi - \frac{i}{2}\kappa(\phi - h) \tag{3.2}$$

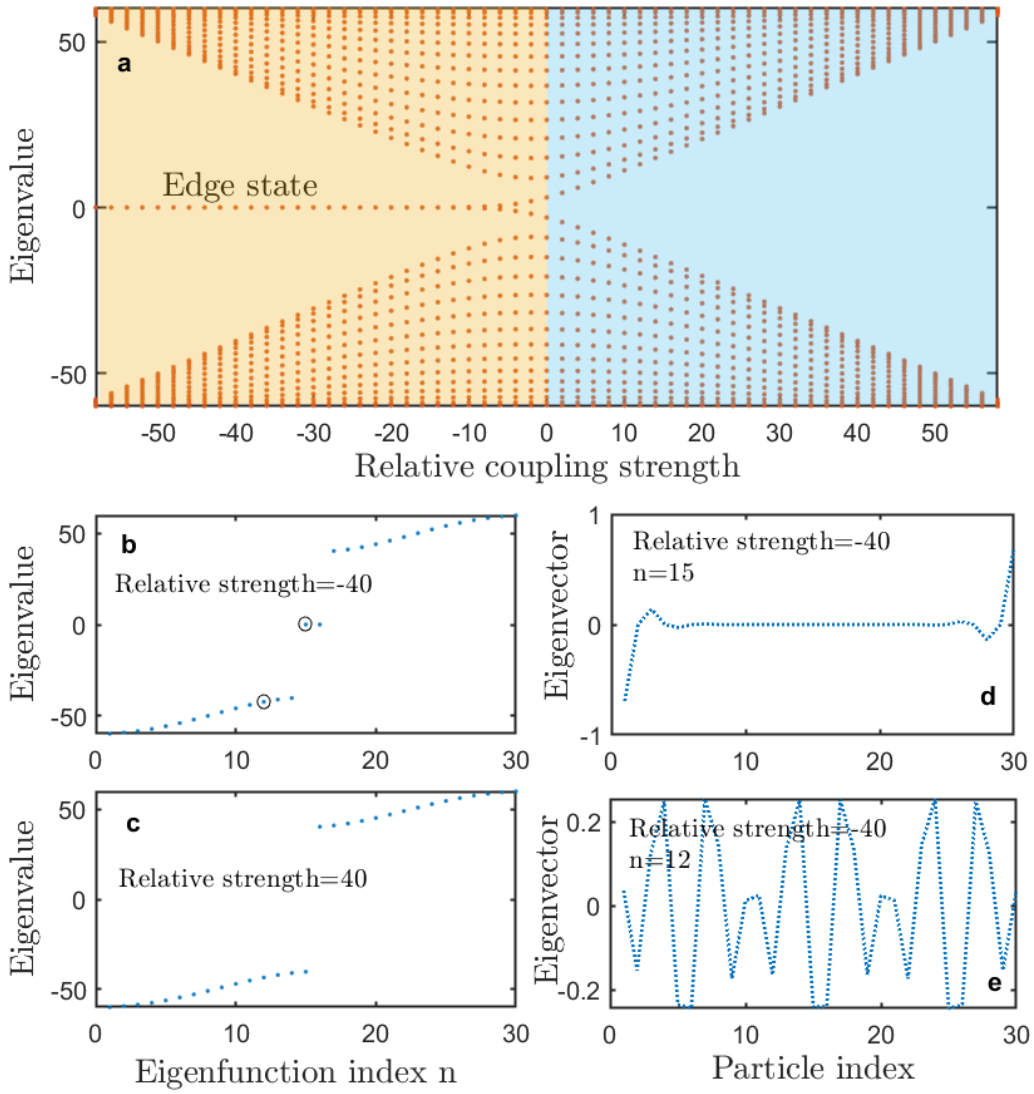

Fig. 3.2 (a) Relative coupling strength is defined as the offset between c_1, c_2 ($c_2 - c_1$ in the orange range; $c_1 - c_2$ in the blue range) given Fig.3.1 (b, c). The bands in blue and orange carpets are solved separately with matrix H_b, H_c. (b, c) Full band structures are presented with eigenmode indices. (d, e) Eigenvector shows the edge and trivial states distribution, corresponding to the eigenvalue marked with black circles in (b). The simulation contains 30 particles.

where d_1 is the nonlinear repetition rate; $d_{2,3}$ are the second and third order of dispersions; κ is the linewidth where the quality factor $Q = \omega/\kappa$; γ is the nonlinear factor and h is the gain.

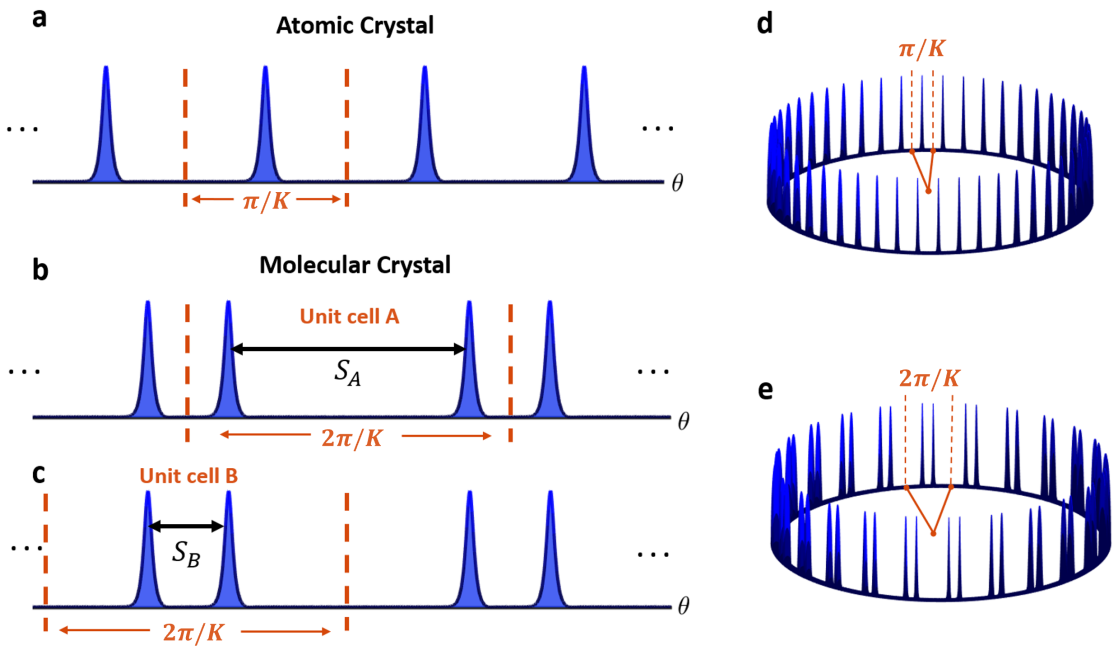

Fig. 3.3 A sketch of perfect/atomic soliton crystals and molecular soliton crystals. The spacings in unit cells A and B satisfy $S_A + S_B = 2\pi/K$. Panel(d, e) show the atomic and molecular crystals composed of 48 solitons.

The dimensionless LLE is obtained with the substitution $\sqrt{\gamma/\kappa}\phi = \psi$:

$$i\partial_t \psi = \delta\psi + \sum_{j=1}^{3} \frac{F_{d_j}}{j!}(-i\partial_\theta)^j \psi - |\psi|^2\psi - \frac{i}{2}(\psi - \mathscr{P}) \tag{3.3}$$

Here, t is dimensionless time, which equals physical time normalized to κ. $\delta = (\omega_0 - \omega_p)/\kappa$ is normalized detuning of the pump laser frequency, and normalized dispersions are $F_{d_j} = d_j/\kappa$. The pump is linked to the laser power $\mathscr{W}$ with the relation:

$$\mathscr{P} = \sqrt{\frac{\gamma\eta\mathscr{F}\mathscr{W}}{\kappa\pi}} \tag{3.4}$$

where $\eta < 1$ is the coupling factor and $\mathscr{F}$ is the finesse of the resonator. In the following, we will take the dimensionless model into consideration. Below, we derive the Bloch states using the lattice periodicity:

$$\psi(\theta) = \psi(\theta + na) \tag{3.5}$$

where $a = 2\pi/K$ is the periodicity for both atomic and molecular cases. The Fourier series dictates:

$$\psi(\theta) = \sum_k \psi_k e^{iG_k\theta} \tag{3.6}$$

$$\psi(\theta + na) = \sum_k \psi_k e^{iG_k(\theta+na)} = \sum_k \psi_k e^{iG_k\theta} e^{iG_k na} \tag{3.7}$$

$$e^{iG_k na} = 1 \rightarrow cos(G_k na) + isin(G_k na) = 1 + 0i \rightarrow G_k = \frac{2\pi k}{a}, k \in \mathbb{Z}^+ \tag{3.8}$$

Note k varies from 1 to $K = 2\pi/a$ (ring geometry) corresponding to the grids in first Brillouin zone with unique vector of every k.

Due to the periodicity, the study can be conveniently restricted in the range of one period. In the Fourier domain, the equivalent expression is $\mu = lK$, where $\mu = 0, \pm K, \pm 2K, \ldots$ is the resonator mode index and $l = 0, \pm 1, \pm 2, \ldots$ is the unit cell mode index. The direct connection allows us to track soliton crystals in the unit cell with great advantages: the computational efficiency can be largely boosted by confining the computational space to one unit cell. For example, in the spectral domain, the soliton crystal composed of K unit cells has the FSR spacing of K, and the equivalent solution can be computed by considering one unit cell solution spaced by 1 FSR. This merit will be obvious for metacrystals. The single crystal wave ψ_c in the range of $[0, 2\pi/K)$ is defined as the summation of its Fourier series:

$$\psi_c(\theta) = \sum_l \psi_{Kl} e^{iKl\theta} = \psi_c(\theta + \frac{2\pi}{K}) \tag{3.9}$$

The perturbation $\tilde{\psi}$ is written as the summation of periodic states $X_k(\theta,t)$ and $Y_k^*(\theta,t)$ [20]:

$$\tilde{\psi} = \sum_k \left(X_k(\theta,t) e^{ik\theta} + Y_k^*(\theta,t) e^{-ik\theta} \right) \tag{3.10}$$

$$X_k(\theta,t) = X_k(\theta) e^{-it\beta_k + t\lambda_k} = X_k(\theta + \frac{2\pi}{K}, t) \tag{3.11}$$

$$Y_k(\theta,t) = Y_k(\theta) e^{-it\beta_k + t\lambda_k} = Y_k(\theta + \frac{2\pi}{K}, t) \tag{3.12}$$

The substitution of $\psi = \psi_c + \tilde{\psi}$ into Eq.(3.3) returns:

$$(\beta_k + i\lambda_k + i\frac{1}{2}) |\mathbf{u_k}\rangle = \hat{J} |\mathbf{u_k}\rangle = \hat{\sigma}\hat{H} |\mathbf{u_k}\rangle \tag{3.13}$$

where

$$\hat{\sigma} = \begin{bmatrix} 1 & 0 \\ 0 & -1 \end{bmatrix}, \hat{H} = \begin{bmatrix} \hat{D}_k & -\psi_c^2 \\ -\psi_c^{*2} & \hat{D}_{-k}^* \end{bmatrix}, |\mathbf{u_k}\rangle = \begin{bmatrix} X_k \\ Y_k \end{bmatrix} \tag{3.14}$$

$$\hat{D}_k = \delta - 2|\psi_c|^2 + \sum_j \frac{F_{d_j}}{j!}(k - i\partial_\theta)^j, \theta \in [0, \frac{2\pi}{K}) \tag{3.15}$$

$X_k(\theta,t)$ and $Y_k^*(\theta,t)$ are the pair of eigenstates of the linearized system at the given index k with the same periodicity as ψ_c. The eigenvalue can be separated into real (λ_k) and imaginary (β_k) parts, where $k = 1,2,\ldots,K$ is the Bloch momentum. The Bloch formalism enables the study within the first Brillouin zone with the following translations:

$$\lambda_k = \lambda_{k+K}; \beta_k = \beta_{k+K}; |\mathbf{u_k}\rangle = |\mathbf{u_{k+K}}\rangle\, e^{iK\theta} \tag{3.16}$$

Note, for each k, $|\mathbf{u_k}\rangle = [X_k, Y_k]^T$ are cell-periodic functions along θ. Eq.(3.13) with index k from 1 to K within one Brillouin zone depicts all Bloch states without redundancy. The eigenfrequency β_k will be given below in the band structure discussion.

3.2.2 Band structures and Bloch functions

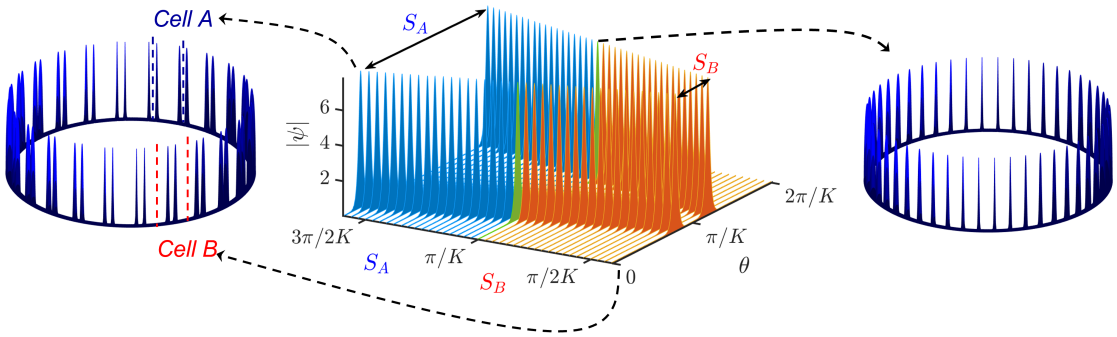

Fig. 3.4 A set of soliton crystal unit cells are solved with Eq.3.3. The spacings are set as a variable for different cases. The fixed parameters are $d_2/\kappa = 5\times10^{-4}$, $d_3/\kappa = 5\times10^{-7}$, $\delta/\kappa = 30$, and $\mathscr{P}^2 = 25$. Unit cells in blue and red pair feature $S_A + S_B = 2\pi/K$, where $K = 24$. The green shows the atomic soliton crystals with $S_A = S_B$.

Periodic soliton crystals feature the periodicity of $2\pi/K$. The SSH-like soliton crystals are formed with small oscillatory tails along the microresonator. In Fig.3.4, the branch of solutions are solved by applying the Bloch formalism, and the stationary solutions are tracked by Newton's method under the manipulation of spacing between solitons in each unit cell. The difference of the interaction strengths between the left and right neighbours of a given soliton, in other words, the imbalance of the intra-cell and inter-cell coupling rates, is controlled by the separation distance. They are 20 pairs of crystals where each pair contains one blue and one red combination featuring the relation $S_A + S_B = 2\pi/K$. Here, we have

demonstrated the stability of all solutions by seeding perturbations to the stationary soliton solutions (see appendix). Given the unit cell solitons, the band structures in the panel of (k, β_k) can be obtained by inserting ψ into Eq.3.14.

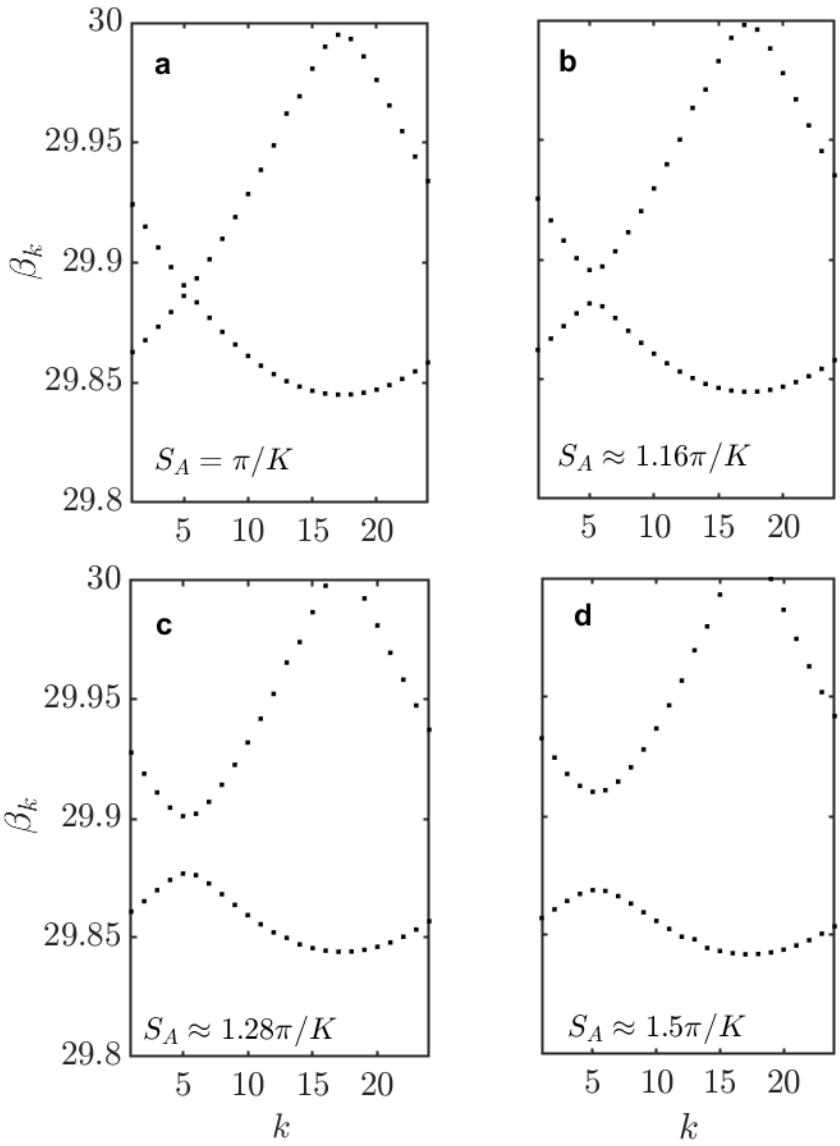

Fig. 3.5 Band structures are computed for atomic and molecular crystals with different S_A labelled in each panel. The horizontal axis marks the k from 1 to 24, and the vertical axis marks the frequency β_k. Panel (a) shows the crossover of two bands for atomic crystals, and such bands can be separated in the transition from atomic type to strong coupled molecular ones, i.e., see the interval change from panel (b) to (d).

Four typical band structures in Fig.3.5 show that the spacing between two neighbouring solitons modifies the intervals between upper and lower frequency bands. When $S_A = \pi/K$, the atomic crystals have two bands touching each other, where the functions $[X_k, Y_k]^T$ for the lower band are given in Fig.3.6. Note that the profiles are divided into real and imaginary parts. The non-trivial jumps happen in real and imaginary parts at $k = 5$. Interestingly, a smooth connection along k can be achieved if one swaps the $[X_k, Y_k]^T$ with the upper band in the region of $k \in [1, 5]$. It indicates the mixture of two bands for the atomic crystal, i.e., the continuity is broken in the discrete lattice.

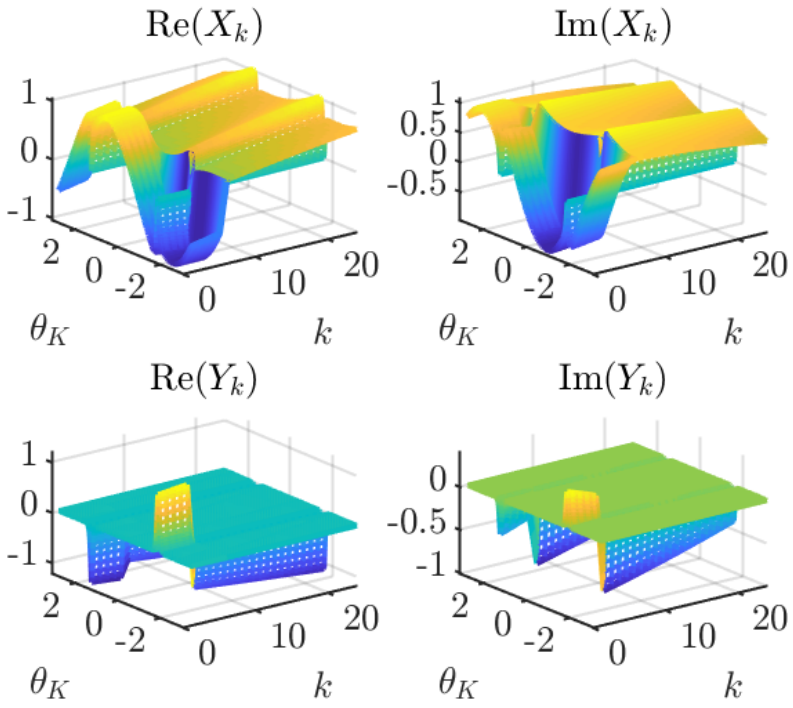

Fig. 3.6 Periodic functions X_K, Y_K are computed for atomic crystals. The lower band profiles are displayed in Fig.3.5(a).

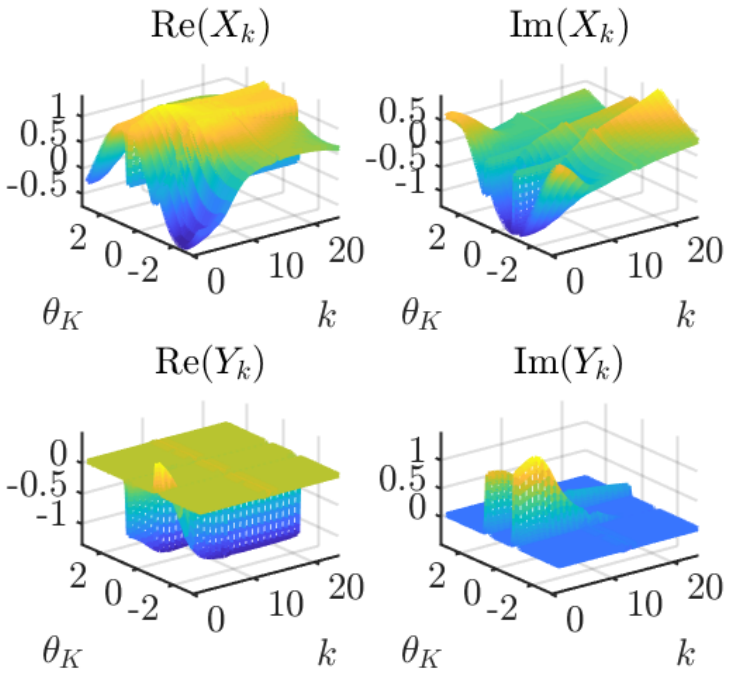

Fig. 3.7 Periodic functions X_K, Y_K are computed with $S_B = 0.5\pi/K$.

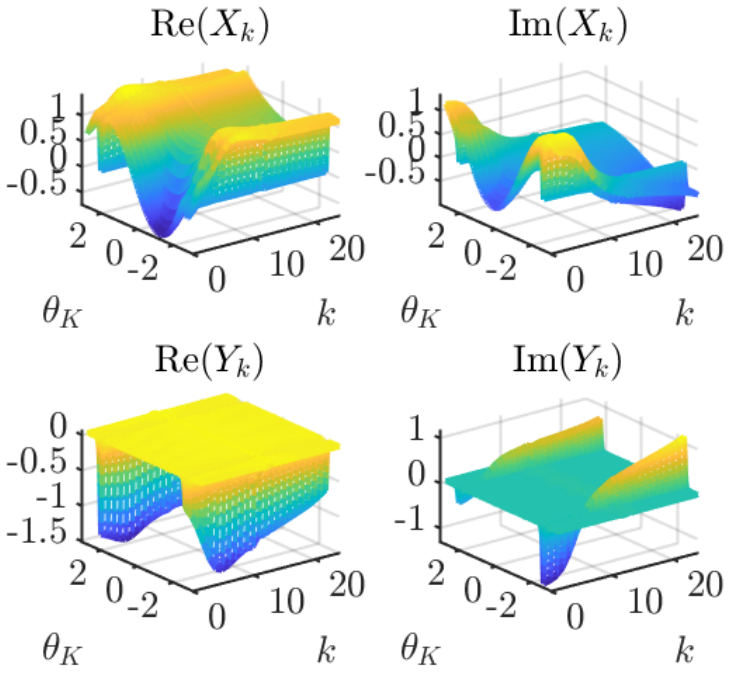

Fig. 3.8 Periodic functions X_K, Y_K are computed with $S_A = 1.5\pi/K$.

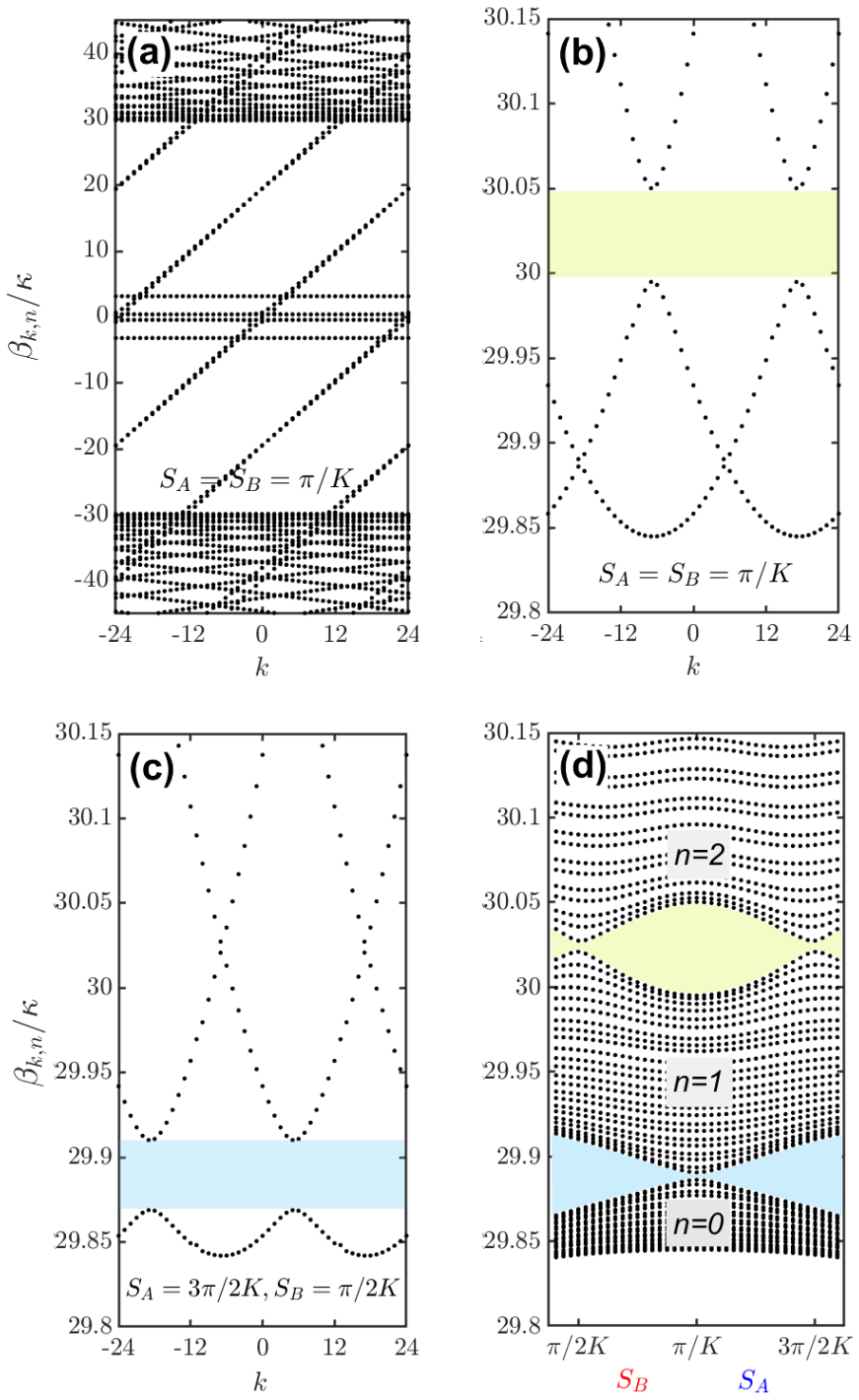

Fig. 3.9 Photonic band structures displayed in two Brillouin zones $k \in [-24, 24], K = 24$. Panel (b) shows the bandgap of atomic crystals at $\beta_{k,n} \approx 30$ in the yellow-shaded region. Panel (c) shows the first bandgap in blue for molecular crystals. $S_A + S_B = 2\pi/K$ means the same solution arranged in two unit cell setups. Panel (d) shows the whole bands with varying distances of S_A, S_B.

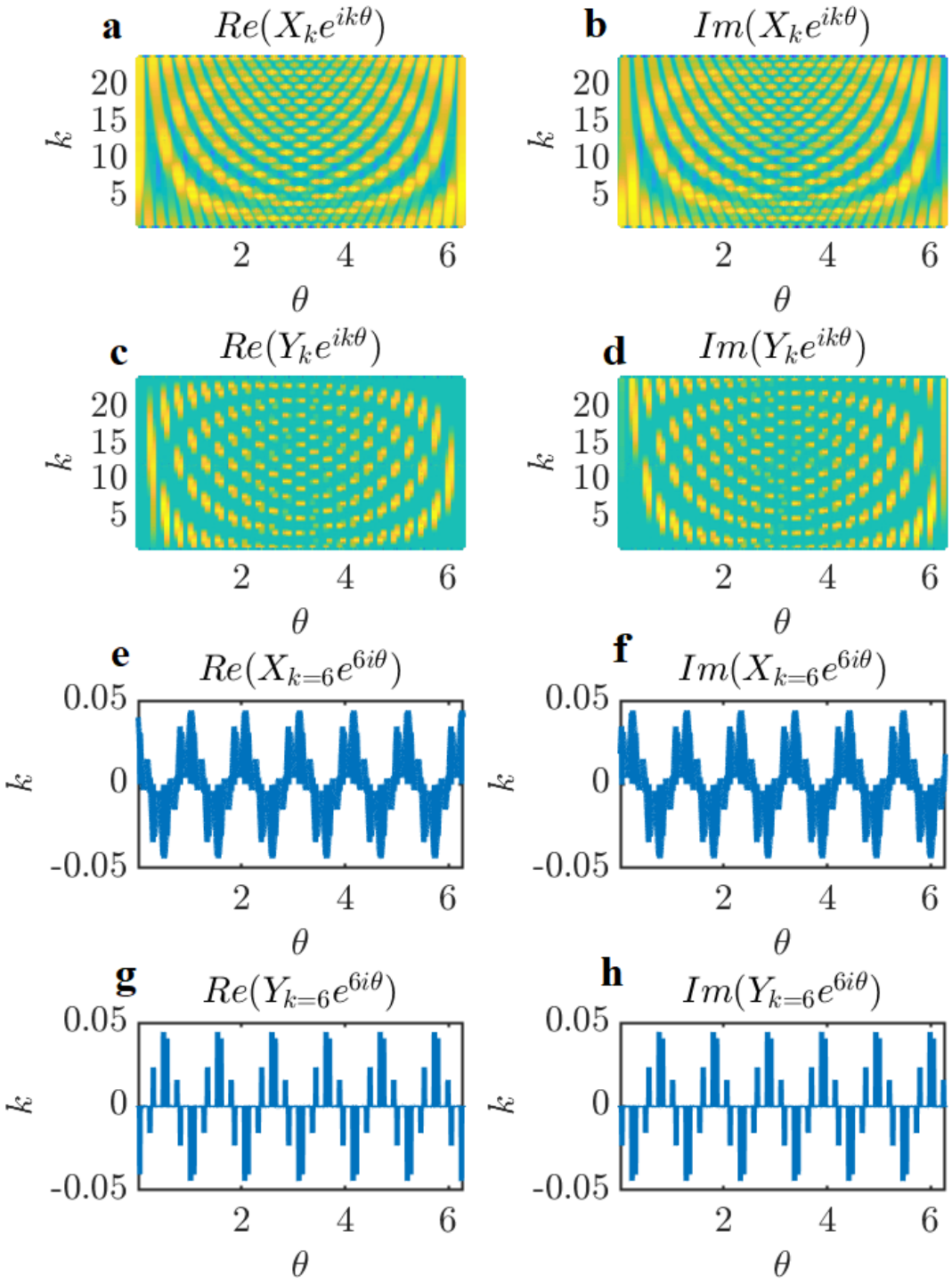

Fig. 3.10 Bloch functions are computed with $S_A = 1.5\pi/K$. The periodic functions X_K, Y_K are modulated by phases $e^{ik\theta}$. Panels (a-d) show the evolution of the Bloch functions along k. The yellow and blue carpets relate to the high and low amplitudes, separately. Panels (e-h) present the slide capture at each corresponding k.

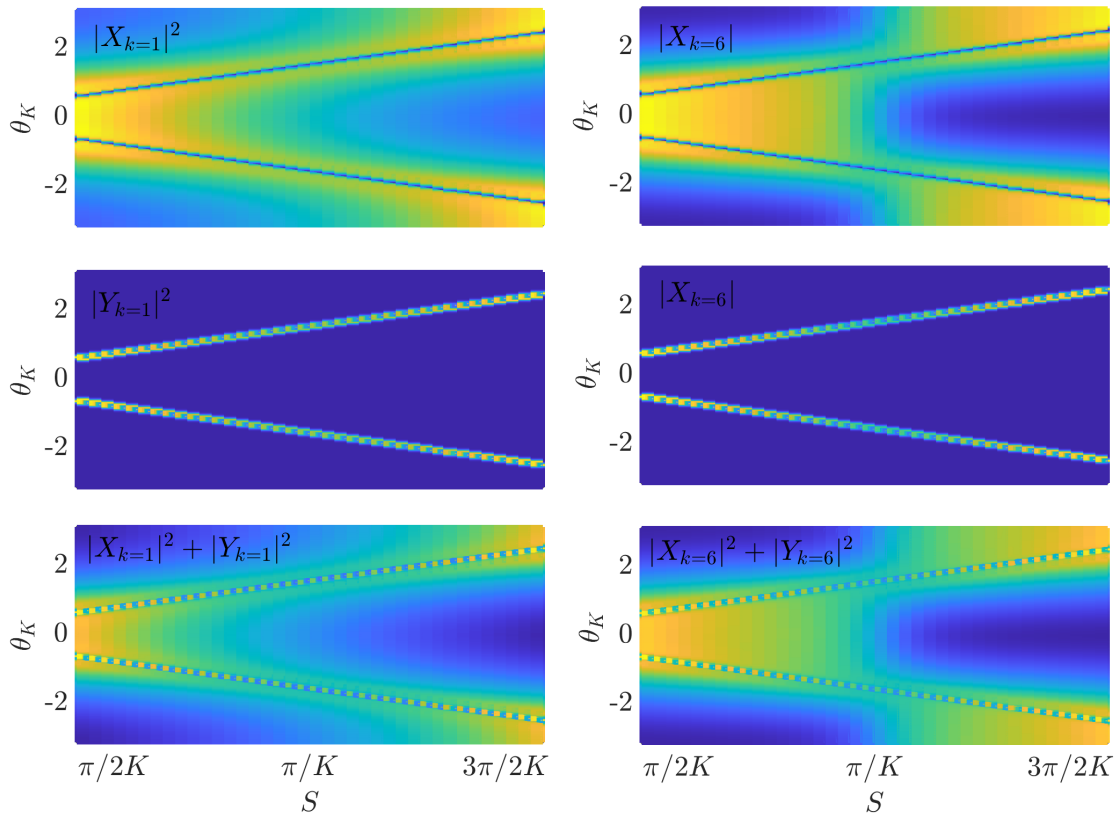

Fig. 3.11 Periodic functions X_K, Y_K are captured with varying S for fixed $k = 1, 6$. The saw-edged tilted lines imply the molecule's location, and the carpet density reveals the localization of the periodic functions for two typical k examples.

The lower and upper bands will be distinguishable when the coupling between two neighbouring solitons becomes stronger induced by the dispersive wave. A clear molecular band transition can be seen from Fig. 3.5 (a-d). Meanwhile, the periodic functions in Fig.3.7 and Fig.3.8 also give the continuous transition along k, different from the flips in the atomic case. The cases $S_A = 1.5\pi/K$ and $S_B = 0.5\pi/K$ are defined concerning unit cells A and B, even though their band structure share the same distribution, but their Bloch functions do not. In Fig.3.9 (a), the tilted straight lines are produced with non-zero d_3. If the high-order dispersion is switched off, such tilted pattern will no longer exist. We assume it should be associated with the spectral recoil effect. Panels (b,c) show the band spectrum with the blue carpet for the first gap and yellow carpet for the second. In Fig.3.9 (d), we mark the bandgap between bands $n = 0, 1$ and $n = 1, 2$ with varying $S_{A,B}$. One notable feature in these plots is the non-trivial (topological) bands at $\beta_{k,n} \approx 30$. This value closes to the detuning scaled by linewidth κ in the Jacobian. Provided that the on-site energy in the SSH lattice shifts the

band frequencies in the same scale, we should look for the non-trivial structure at $\beta_{k,n} \approx \delta/\kappa$. The Bloch functions in Fig.3.10 describe the distribution of the photonic waves subjected to the periodic potentials created by the soliton crystals. The X_k components are much more dispersive than Y_k, which are centralized around soliton positions, see Fig. 3.11.

3.2.3 Geometric phase and Wannier functions

The geometric phase in a one-dimensional lattice is known as the zak phase [21]. The Hermitian Hamiltonian features the form:

$$\gamma_n = \int_{-\pi/a}^{\pi/a} X_{nn}(k) dk \tag{3.17}$$

$$X_{nn}(k) = \frac{2\pi}{a} \int_0^a u_{nk}^*(x) i \frac{\partial u_{nk}(x)}{\partial k} dx \tag{3.18}$$

where γ_n is the integration of the kernels X_{nn} in the reciprocal domain over the whole Brillouin zone $[-\pi/a, \pi/a]$ (a is the lattice constant). u_{nk} is the periodic function in band number n with given index k. For non-Hermitian Hamiltonian, the complex geometric phase for band n is defined by [22–24]:

$$\gamma_n = iM_{nk} \int_{BZ} \langle p_{nk} | \, \partial_k \, | q_{nk} \rangle \, dk \tag{3.19}$$

where $|q\rangle, |p\rangle$ are the eigenvectors of $\hat{H}, \hat{H}^\dagger$, i.e., the right and left eigenvectors of the Hamiltonian, separately. M_{nk} is the normalization factor. The discretization of points along k leads to the summation of every accumulated phase within one Brillouin zone:

$$\mathscr{Z}_n = i \sum_k \frac{\langle c_{nk} | \, \partial_k \, | u_{nk} \rangle}{\langle c_{nk} | u_{nk} \rangle} \tag{3.20}$$

Here, the right-eigenvector $|u_{nk}\rangle$ satisfies:

$$\hat{\sigma}\hat{H} \, |u_{nk}\rangle = (\beta_{nk} + i\lambda_{nk} + i\frac{1}{2}) \, |u_{nk}\rangle \tag{3.21}$$

The eigenvector $|c_{nk}\rangle$ of the Hermitian conjugation $(\hat{\sigma}\hat{H})^T$ is:

$$\hat{H}\hat{\sigma} \, |c_{nk}\rangle = (\beta_{nk} - i\lambda_{nk} - i\frac{1}{2}) \, |c_{nk}\rangle \tag{3.22}$$

β_{nk} is the RF spectrum of the crystals of light fulfilling the condition $|\beta_{nk}| >> |\lambda + \frac{1}{2}|$, and the left-eigenvector of $\hat{\sigma}\hat{H}$ is given by $\langle c_{nk}| = \langle u_{nk}| \, \hat{\sigma}$. This relation holds from the simple linear algebra by neglecting trivial terms λ_{nk} and $\frac{1}{2}$ [25]. Inserting the left-eigenvector in

Eq.3.20, we have:

$$\mathscr{Z}_n = i\sum_k \frac{\langle u_{nk}|\,\hat{\sigma}\partial_k\,|u_{nk}\rangle}{\langle u_{nk}|\,\hat{\sigma}\,|u_{nk}\rangle} \tag{3.23}$$

Note the notation $|u_{nk}\rangle$ composed of two eigenvectors due to the 2×2 matrix, it can be readily defined as $[X_{nk}, Y_{nk}]^T$, which gives the following:

$$\mathscr{Z}_n = i\sum_k \frac{\int_0^{2\pi/K}(X_{nk}^*\partial_k X_{nk} - Y_{nk}^*\partial_k Y_{nk})d\theta}{\int_0^{2\pi/K}(|X_{nk}|^2 - |Y_{nk}|^2)d\theta} \tag{3.24}$$

Eq.3.24 is the general form for computing the geometric phase in the discrete ring system. Note that the gauge invariance is generally true in the k continuous system, but the discrete system does not strictly obey the manner. Therefore, the geometric phases may fluctuate under different gauge restrictions [26]. To overcome this issue and make a deterministic computation of the geometric phase, we need to design an approach without the influence from gauge selection. In the following, we rewrite Eq. 3.24 into discrete form [27]:

$$\mathscr{Z}_n \approx i\sum_k \frac{\int_0^{2\pi/K}(X_{nk}^*(X_{n,k+1} - X_{n,k}) - Y_{nk}^*(Y_{n,k+1} - Y_{n,k})d\theta}{\int_0^{2\pi/K}(|X_{nk}|^2 - |Y_{nk}|^2)d\theta} \tag{3.25}$$

$$= i\sum_k \frac{\int_0^{2\pi/K}(X_{nk}^*X_{n,k+1} - |X_{nk}|^2 - Y_{nk}^*Y_{n,k+1} + |Y_{nk}|^2)d\theta}{\int_0^{2\pi/K}(|X_{nk}|^2 - |Y_{nk}|^2)d\theta} \tag{3.26}$$

$$= i\left(\sum_k \frac{\int_0^{2\pi/K}(X_{nk}^*X_{n,k+1} - Y_{nk}^*Y_{n,k+1})d\theta}{\int_0^{2\pi/K}(|X_{nk}|^2 - |Y_{nk}|^2)d\theta} - 1\right) \tag{3.27}$$

$$= i\left(\sum_k \frac{\langle u_{n,k}|\,\hat{\sigma}\,|u_{n,k+1}\rangle}{\langle u_{n,k}|\,\hat{\sigma}\,|u_{n,k}\rangle} - 1\right) \tag{3.28}$$

Consider the exponent form:

$$i\mathscr{Z}_n \approx -\ln\prod_k \left(e^{A_k} - 1\right) \tag{3.29}$$

$$A_k = \frac{\langle u_{n,k}|\,\hat{\sigma}\,|u_{n,k+1}\rangle}{\langle u_{n,k}|\,\hat{\sigma}\,|u_{n,k}\rangle} \tag{3.30}$$

Using the Taylor expansion for an exponential function in the form of $e^x = 1 + x + \cdots$ (namely $e^{A_k} \approx 1 + A_k$), the terms in the brackets can be reduced to:

$$i\mathscr{Z}_n \approx -\ln\prod_k (A_k) \tag{3.31}$$

Then, the geometric phase can be written as:

$$\mathscr{Z}_n \approx -Im\left(\ln\prod_k \frac{\langle u_{n,1}|\,\hat{\sigma}\,|u_{n,2}\rangle\langle u_{n,2}|\,\hat{\sigma}\,|u_{n,3}\rangle\cdots\langle u_{n,K-1}|\,\hat{\sigma}\,|u_{n,K}\rangle\langle u_{n,K}|\,\hat{\sigma}\,|u_{n,1}e^{-iK\theta}\rangle}{c_k}\right) \tag{3.32}$$

where normalization factor $c_k = \langle u_{n,k}|\,\hat{\sigma}\,|u_{n,k}\rangle$. The last bracket takes the relation in Eq.3.16. The logarithm form gives gauge-invariant expression as the arbitrary phase in periodic functions can be cancelled out through the multiplication of the bras and kets. Fig.3.12 shows the geometric phase computed with such formula, and the π difference between the phases from unit cells A and B (i.e., $|\mathscr{Z}_n^{(A)} - \mathscr{Z}_n^{(B)}| = \pi$ when $S_A \neq S_B$) implies the non-trivial topological band. Such π flip happens at the point $S_A = S_B = \pi/K$, corresponding to the atomic crystals where any single soliton has equal coupling strength from both neighbours.

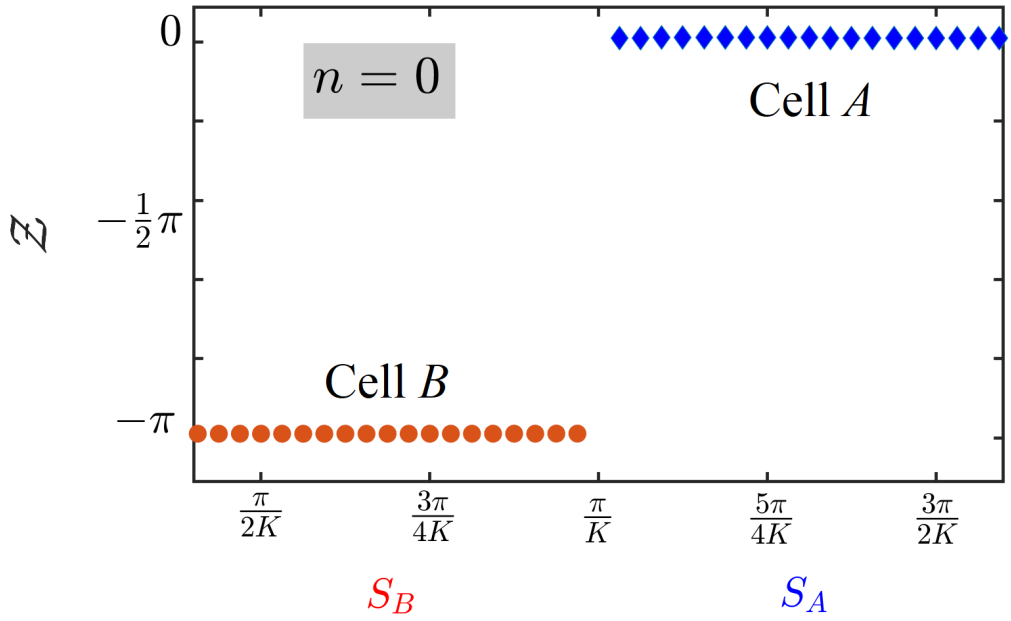

Fig. 3.12 Geometric phase computed by Eq.3.32, the blue and orange markers are related to the phases for unit cells A and B, respectively. The pair of solutions feature the relation $S_A + S_B = 2\pi/K$, which presents a phase jump of π.

Next, we discuss the Wannier function, which can be mapped as the Fourier transform of the Bloch functions in the following form:

$$|w_{n,J}\rangle = \frac{1}{K}\int_k |u_{n,k}\rangle\, e^{ik\theta} e^{-ik\theta_J} dk \tag{3.33}$$

where the first part $\left|u_{n,k}\right\rangle e^{ik\theta}$ is the Bloch function and second part $e^{-ik\theta_J}, \theta_J = \frac{2\pi(J-1)}{K}$ (J is the index of unit cell) is defined as per [28, 29]. It shows that for each index $'J'$, there is a corresponding function expressed as the summation of Bloch functions along the reciprocal space, leading to the spatial function $|w_{n,J}\rangle$. As the Bloch functions computed from matrix $\hat{\sigma}\hat{H}$ can possess an arbitrary phase (which has no physical meaning), we are free to select our gauge for the Wannier functions. Here, our gauge is chosen for the Bloch functions under the condition of $\mathrm{Im}(X_{n,k}|_{\theta=3\pi/2K}) = 0$. In fact, the spatial point can be either $\theta = \pi/2K$ or $\theta = 3\pi/2K$. They are the mirror points for half of the unit cell, which reduce the numerical impacts from the normalization of the unit cells in different S_A, S_B. The Wannier to Bloch functions can be readily obtained via inverse transformation in the following form:

$$|u_{n,J}\rangle = \int_J \left|w_{n,k}\right\rangle e^{-ik\theta} e^{ik\theta_J} dJ \tag{3.34}$$

Recall our definitions of $\left|u_{n,k}\right\rangle = [X_{n,k}, Y_{n,k}]^T$ and $|w_{n,J}\rangle = [W_{n,J}, V_{n,J}]^T$. The geometric phase can be obtained from the Wannier function by substituting Eq.3.33 into Eq.3.19:

$$\mathscr{L}_n = i\int_k \frac{\int_0^{2\pi/K}(X_{nk}^*\partial_k X_{nk} - Y_{nk}^*\partial_k Y_{nk})d\theta}{\int_0^{2\pi/K}(|X_{nk}|^2 - |Y_{nk}|^2)d\theta} \tag{3.35}$$

$$= \frac{i}{K}\int_k \frac{\int_{\theta_J-\pi}^{\theta_J+\pi}(X_{nk}^*\partial_k X_{nk} - Y_{nk}^*\partial_k Y_{nk})d\theta}{\int_{\theta_J-\pi}^{\theta_J+\pi}(|X_{nk}|^2 - |Y_{nk}|^2)d\theta} \tag{3.36}$$

$$= \frac{i}{K}\int_k dk \int_J \frac{\int_{\theta_J-\pi}^{\theta_J+\pi}(W_{nk}^* e^{ik(\theta-\theta_J)}\partial_k W_{nk} e^{-ik(\theta-\theta_J)} - V_{nk}^* e^{ik(\theta-\theta_J)}\partial_k V_{nk} e^{-ik(\theta-\theta_J)})d\theta}{\int_{\theta_J-\pi}^{\theta_J+\pi}(|W_{n,J}|^2 - |V_{n,J}|^2)d\theta} dJ \tag{3.37}$$

$$= \int_J \frac{\int_{\theta_J-\pi}^{\theta_J+\pi}(\theta-\theta_J)(|W_{n,J}|^2 - |V_{n,J}|^2)d\theta}{\int_{\theta_J-\pi}^{\theta_J+\pi}(|W_{n,J}|^2 - |V_{n,J}|^2)d\theta} dJ \tag{3.38}$$

$$= \sum_J \frac{\langle w_{n,J}|\,(\theta-\theta_J)\hat{\sigma}\,|w_{n,J}\rangle}{\langle w_{n,J}|\,\hat{\sigma}\,|w_{n,J}\rangle} \tag{3.39}$$

$$= K\frac{\langle w_{n,J}|\,(\theta-\theta_J)\hat{\sigma}\,|w_{n,J}\rangle}{\langle w_{n,J}|\,\hat{\sigma}\,|w_{n,J}\rangle} \tag{3.40}$$

In Eq.3.36, we use periodicity of the function $\left|u_{n,k}\right\rangle$, which accumulates the phase K times larger than one unit cell, accounting for the ratio of $1/K$. From Eq.3.38 to Eq.3.39, we adopt the discrete form as per the periodicity in the crystal. The last step, from Eq.3.39 to Eq.3.40, uses the properties of the Wannier function that the spatial profiles for different J indices lead to the shift in the θ domain. It means $\theta - \theta_J$ is the shift of the coordinate domain for

every Wannier function, which makes every J component in Eq.3.39 equal. Since J is the index of the unit cells, it accounts for the K coefficient in Eq.3.40. The above connections between Bloch and Wannier functions are developed in a quasi-continuum form, which has been numerically identified.

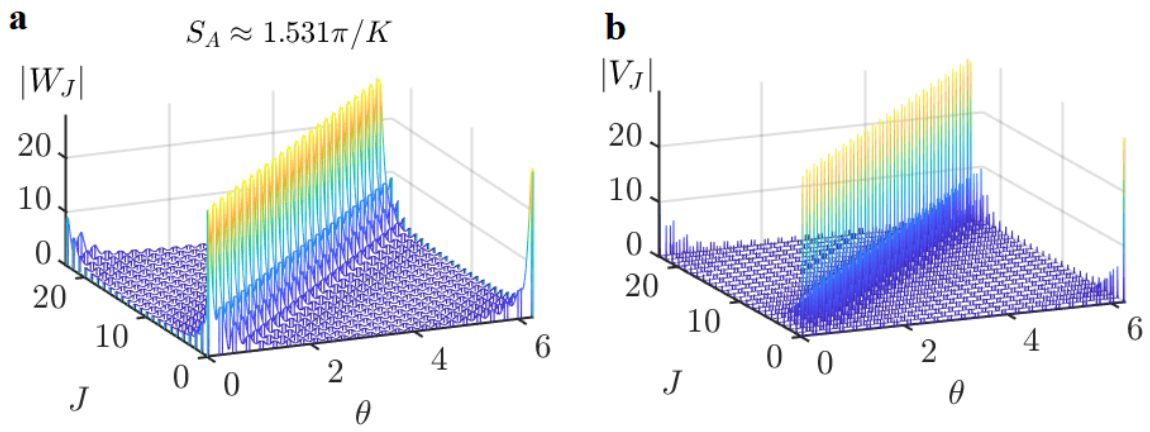

Fig. 3.13 Profiles of Wannier functions $|W_J|, |V_J|$ are solved with $J \in [0, K-1]$. Panels (a, b) present the spatial shift of these functions along J.

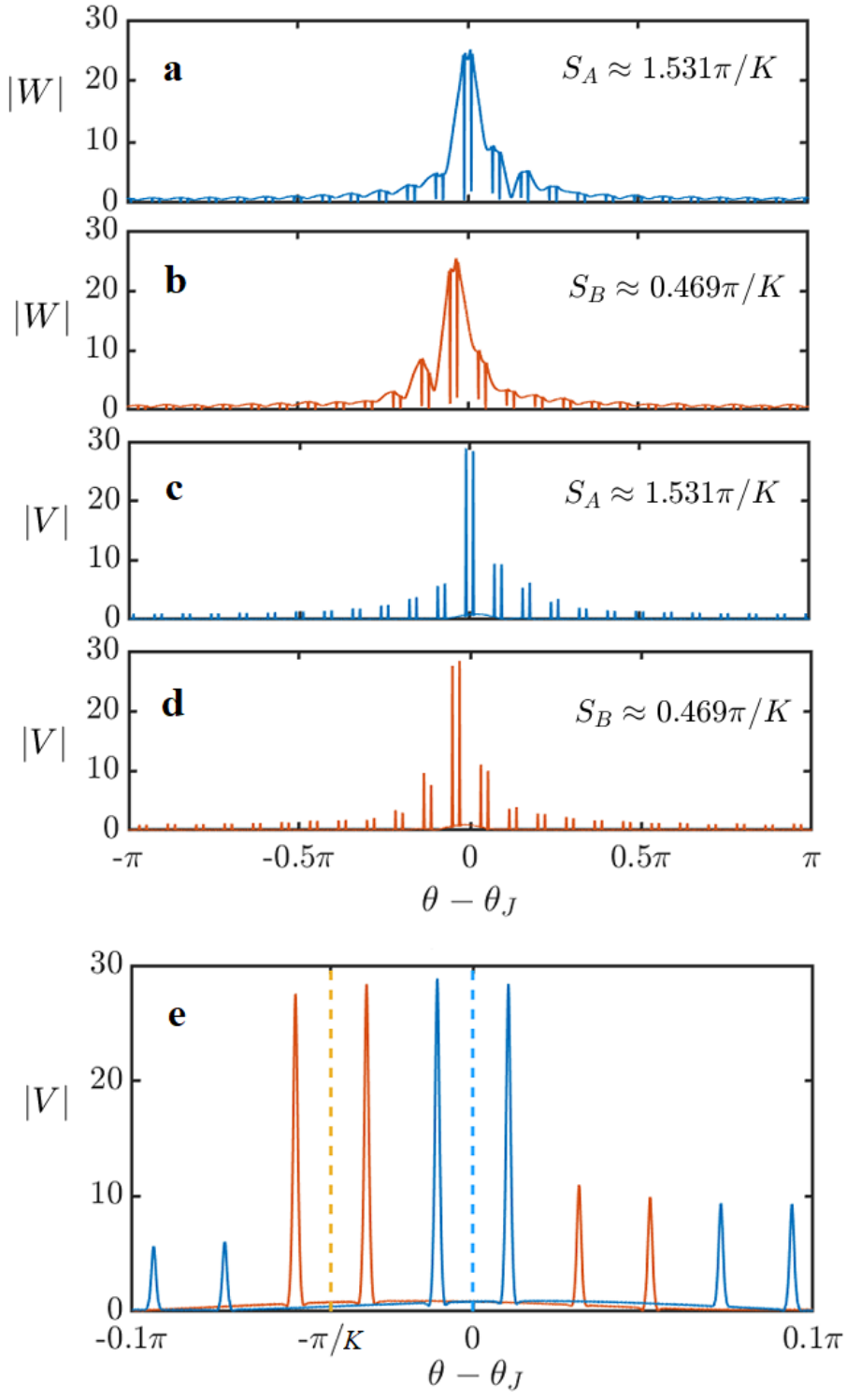

Fig. 3.14 Wannier functions are centralized, i.e., $\theta - \theta_J$. The pair of unit cells $S_A + S_B = 2\pi/K$ shows the shift of the centre of Wannier functions; see zooming comparison in panel (e).

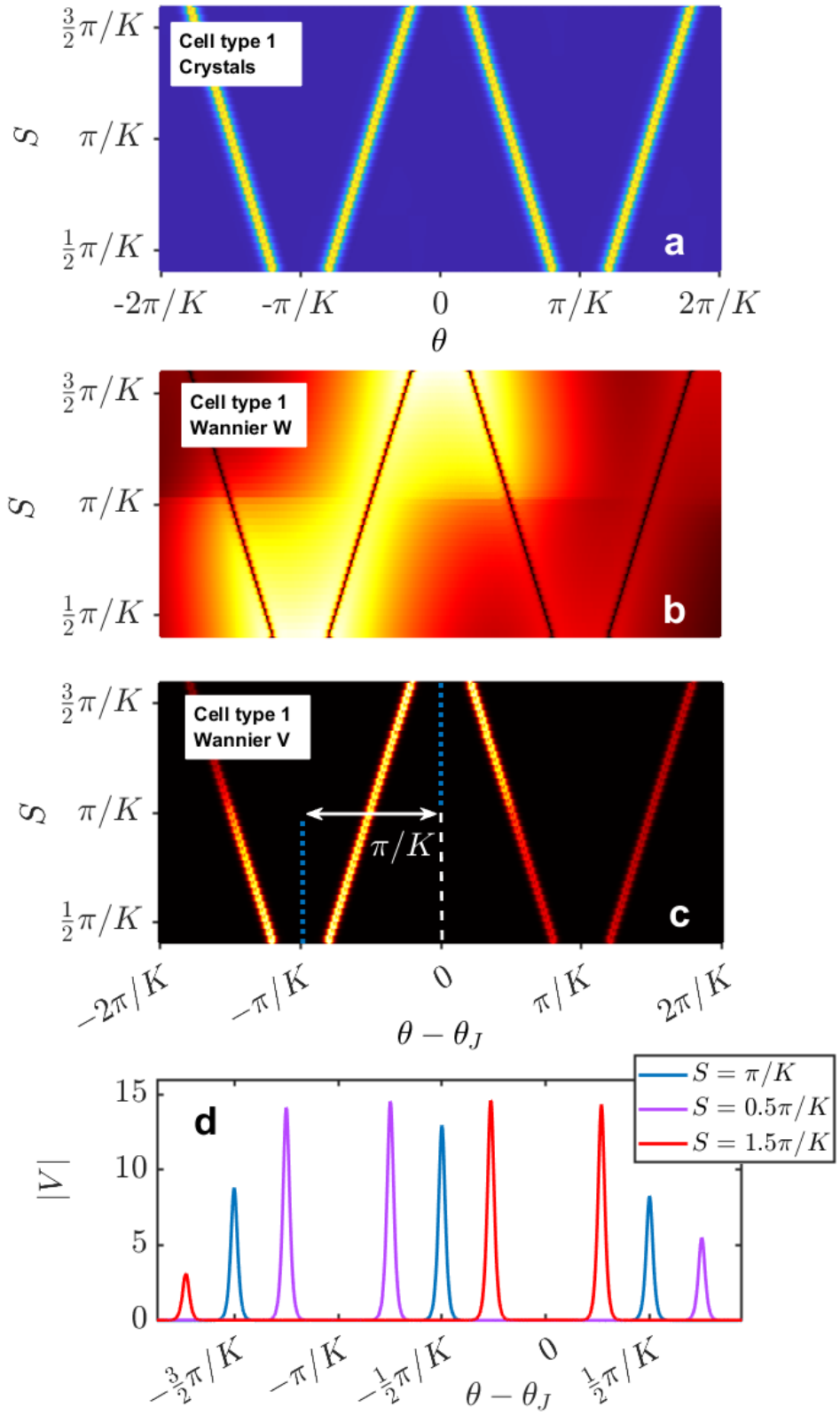

Fig. 3.15 Unit cells are defined in (a), with the corresponding Wannier functions in (b,c). Blue dots in (c) shows the geometric phase that coincides with the Wannier centre. (d) gives examples of centralized Wannier components. Bright/dark carpets show high/low intensities.

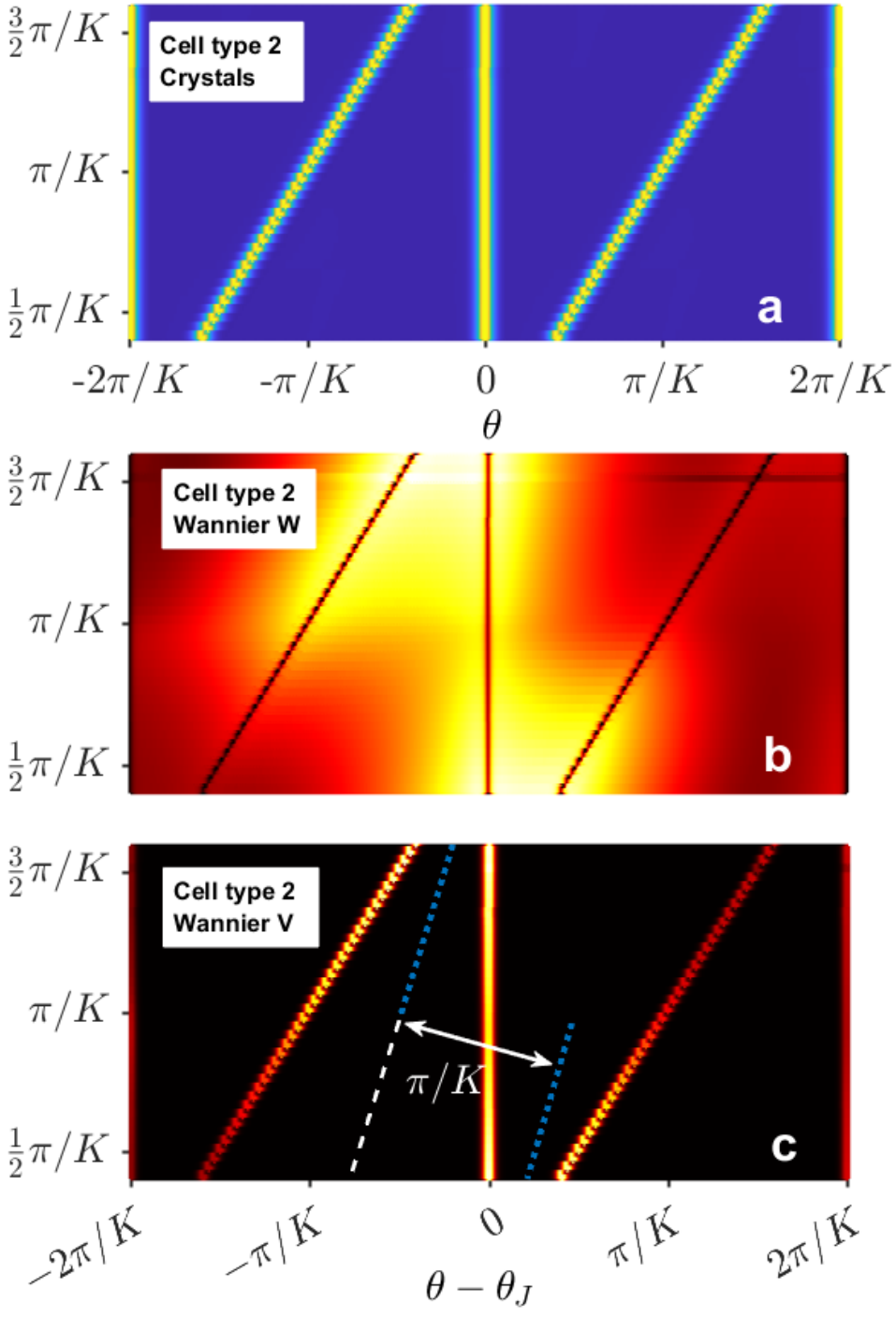

Fig. 3.16 (a) The crystals are centralized by locking one soliton at $\theta = 0$. (b,c) show the geometric phase and corresponding Wannier functions.

Fig.3.13 shows the Wannier function $|w_J\rangle = [W_J, V_J]^T$ shifting with J, and the spatial profiles in both components for adjacent J are locked to the shift of one unit cell. When coordinate $\theta - \theta_J$ is taken, Wannier functions can be simplified in Fig.3.14 (a, c). The other solution in its corresponding unit cell B (which satisfies $S_A + S_B = 2\pi/K$) leads to Wannier functions in panels (b, d). The Wannier centre for the S_A case is roughly 0 (see Fig.3.14 (e)), with the slight asymmetry induced by the high order dispersion. For the S_B case, such a centre is at $-\pi/K$ displayed in red solution. The Wannier centre is physically the averaged coordinate of the photonic waves. As an outcome, the geometric phase will be approximated by the K times the difference between the two Wannier centres, i.e., it equals an absolute value of π as computed through the gauge invariant method given by Eq.3.32.

We present systematic studies of Wannier centres and their geometric phases as a function of the separation in Fig.3.15. In panel(a), we show the region of two unit cell range $\theta \in [-2\pi/K, 2\pi/K]$, where the unit cell is defined in $[0, 2\pi/K]$. The Wannier components $|W|, |V|$ are displayed in Fig.3.15 (b, c), where the clear centres can be captured to be roughly consistent with the blue dots obtained from the gauge invariant geometric phases in Fig.3.15 (c). The spacing between families of unit cells A and B is π/K marked by the double arrow. Nevertheless, in Fig.3.15 (d), when the well-localised component V is selected, the atomic crystal of $S = \pi/K$ implies the Wannier centre of $-\frac{1}{2}\pi/K$, which demonstrates the atomic case (coloured in blue) as a critical one between π flip transition. The Wannier centre gives the geometric phase without additional computations. However, in the previous discussion, our unit cells (no matter families of A or B) are defined in the region of $\theta \in [0, 2\pi/K]$, and the solitons are roughly symmetric along $\theta = \pi/K$. This treatment leads to the vertical blue dots in Fig.3.15(c). One may raise a question that how the Wannier centre varies with different definitions of the unit cell. Namely, except for the current unit cell definition, there is no certain point for all the crystal cases featuring the fixed symmetric point (previously, such a point is π/K). The hypothesis assumes the Wannier centres should shift with the symmetric point within the arbitrarily defined unit cells. A quick check is to arrange the crystals in the form displayed in Fig.3.16 (a). In this regime, the unit cell ('Cell type 2') $\theta \in [0, 2\pi/K]$ is defined by fixing one soliton within a molecule at $\theta = 0$, and the other soliton in the molecule is the same relative spacing as per the case in 'Cell type 1'.

Here are some comments on the computation process: following the arrangement of the crystals in Fig.3.16 (a), we obtained the eigenvectors by solving the non-Hermitian matrix. The eigenvectors are gauged alike to the 'Cell type 1'. The Wannier profiles from the summation in Eq.3.33 are displayed in Fig.3.16 (b, c). Direct computation of geometric phase with gauge invariant approach returns the tilted blue dot lines in panel(c). However, it does not feature the relation $|\mathscr{Z}_{S_A} - \mathscr{Z}_{S_B}| = \pi(S_A + S_B = 2\pi/K)$, but the shortest spacing

between the two tilted lines does. The Wannier centres, marked by the centre of two bright dots at a given separation, coincide with the geometric phases.

3.3 Soliton crystals with defects and edge states

The above discussions identified the non-trivial π flips in both cases of 'Cell type 1' and 'Cell type 2'. In particular, the second type has been considered to extend the discussion of the geometric phases and Wannier centres. This section aims to find the topological states by introducing the defects in the crystals. Similar to the SSH model, one can cut the one-dimensional lattice in different ways (see Fig.3.1(a)): (1) cut the strong coupling bond (in blue) at two sides, leaving the two atoms with weak coupling bonds (in orange) to the main chain (similar to the case given in Fig.3.1(c)); (2) cut the weak coupling bond (in orange) at two sides, leaving the two atoms with strong coupling bonds (in blue) to the main chain (similar to the case given in Fig.3.1(b)); (3) cut strong/weak bond at left side and weak/strong bond at the right side, leaving the weak/strong atoms connected to the main lattice. The first and second cases are similar since S goes through the strong and weak couplings when it crosses $S = \pi/K$. Thus, they are achieved by removing one unit cell in the range from $\theta \in [\pi - \pi/K, \pi + \pi/K]$. Interestingly, the third case will introduce chirality by breaking half (or $N + 1/2$) of the unit cell at the left or right side of the ring. The edge states, similar to the profiles displayed in Fig.3.2 (d), in any of the above discussions will happen near the defect where the weak coupling of one soliton to its nearest neighbour emerges. In the following, the first and second cases are discussed together and the chirality crystals are studied in a separate section.

Numerically, the approach to creating the defect is slightly different to the path of generating periodic soliton crystals. Previously, we have solved the soliton crystals under a set of relative separations within the unit cell space. However, the smallest periodicity for defect crystals is 2π. It requires a much higher volume of modes taken into account, i.e., we have to consider the computational space for the whole microresonator. As a comparison, we use 512 modes in the unit cell range of $\theta \in [0, 2\pi/K)$, which converts to $512 \times 24 = 12288$ modes in the microresonator. In general, the spectrum intensity would decay regularly down to the noise level around the boundaries of computational space, for example, -80dB. Meanwhile, numerically, we will see the decaying intensity of modes when the computational space is extended. Concerning the defect crystals, even though the computational space is ultra-wide, it is still possible to assemble the crystals with desired defects by removing the redundant solitons in the periodic ring. Then, the pre-made defect crystals can be further converged through either the stationary solver or the dynamical LLE modelling.

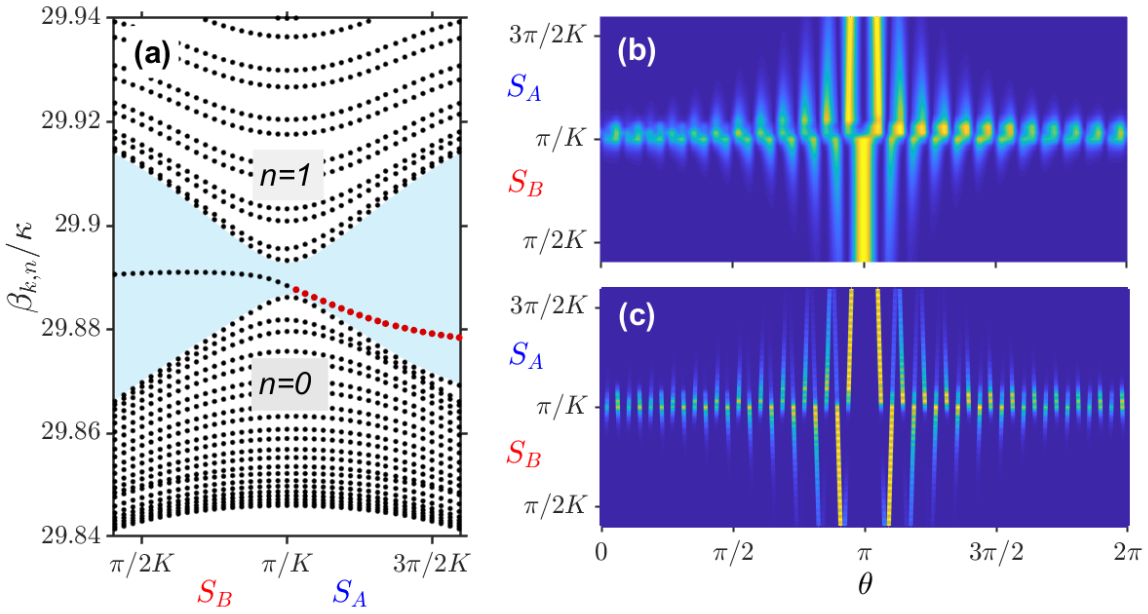

Fig. 3.17 Band structure and eigenstates for 2-soliton defect crystal are given. Edge states emerge for the S_A family, with the distribution of eigenvectors $[X,Y]^T$ presented in panels (b, c), respectively. All eigenvectors are related to the band in panel (a) between $\beta_{k,n} \in (29.87, 29.9)$, with red dots showing the emergence of edge cases.

We start with the discussion of one unit cell taken out from the periodic crystals. In order to be consistent with the cases discussed above, we keep the definitions of S_A, S_B. The difference in the defect ring is that one unit cell in the range of $\theta \in [\pi - \pi/K, \pi + \pi/K]$ is removed. In Fig.3.17 (a), compared to the spectrum in Fig.3.9 (d), the non-trivial band emerges at $\beta_{k,n} \approx 29.89$, with the eigenvectors given in panels (b, c). By checking carefully on the energy distribution of the bright carpets (the yellow columns on top of the blue background), we found the edge states exist in the S_A range with the band marked by the red dots. The corresponding eigenvectors (both X, Y) show the highest amplitudes at the edge soliton locations. This observation shows the similarity to the known SSH model. The other side of S_B presents an unique feature: the highest amplitude of the eigenstates emerge not at the edge soliton locations but at their closest neighbours for the Y eigenstate (see panel(c)), meanwhile, the X state shows the photonic wave is being trapped between two edge solitons (see the thick bright column in panel(b) within S_B range).

Regarding $N + \frac{1}{2}$ (N is an integer) pairs of solitons can be removed from the periodic crystals to make the chiral crystal, a group of tests found that $N = 3$ would be enough to figure out the band structure information, as well as the eigenstate distributions. Fig.3.18 (a,

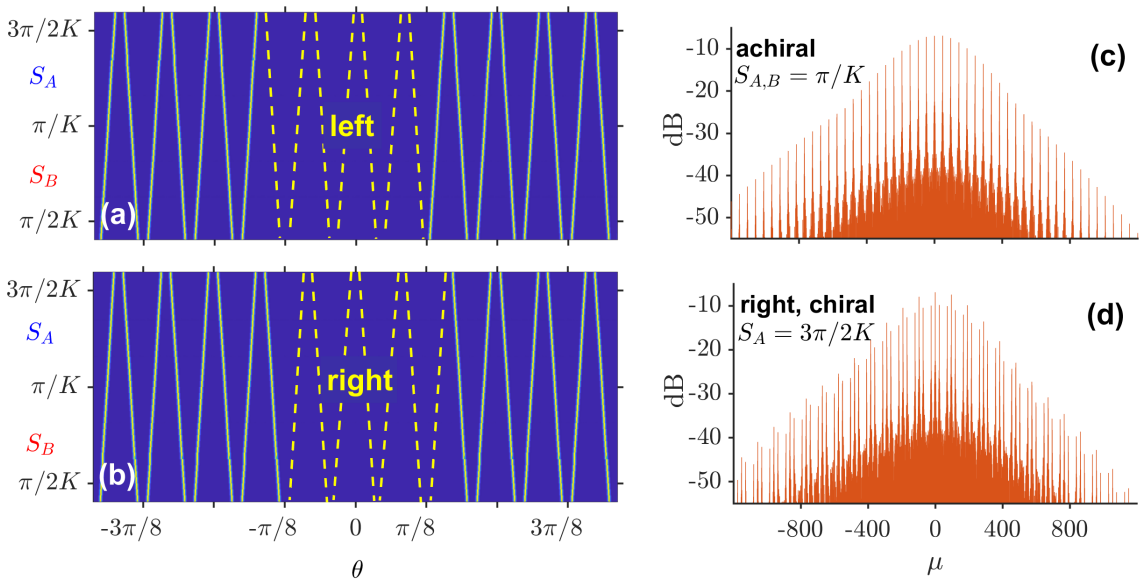

Fig. 3.18 The families of defect soliton crystals with three and a half unit cells are removed. (a,b) shows the chiral symmetry of the left and right setups. (c,d) are two examples of spectrums regarding the cases of defect atomic and molecular crystals, respectively.

b) present 7 solitons have been removed from the ring with their positions marked by yellow dashed lines. In particular, panel (a) shows that half of the unit cell is taken from the left side of the ring in the S_A range, whereas in panel (b), the right side includes the additional absence of soliton. Panel (c) shows the defect crystals for the atomic case with $S_A = S_B$. The spectrum should be equal on either left or right because of the coordinate shift along the ring. The spectrum of one molecular defect crystal in panel (d) presents the distinction in the density of modes compared to atomic case with sparse spectrum. In the discussion of band structure, only one family is needed, and we adopt the 'left' family. The 'right' family can be readily considered as the flip of $S_{A,B}$ along π/K. Fig. 3.19 shows 4 bands inside the gap labelled by the grey shaded numbers. Their corresponding eigenvectors are shown on the right. The wave distribution of Y eigenvectors is comparable to the edge states. However, such edge distribution emerges only at band number 4 for X component. The bright thick carpets of X in band numbers $1,2,3$ show the phononic wave trapped within the potentials induced by the soliton cores, similar to the bandgap guidance in photonic crystal fibres. Finally, only $'4-X, 4-Y'$ have the localized energy shown at the locations of edge solitons.

An odd number of solitons taken out from the periodic crystals breaks the ring's left-right (mirror) symmetry. This is true for any arrangements with $S_A \neq S_B$. The chiral pairs of the right and left defects have spectra which are hard to observe directly. However, such chiral

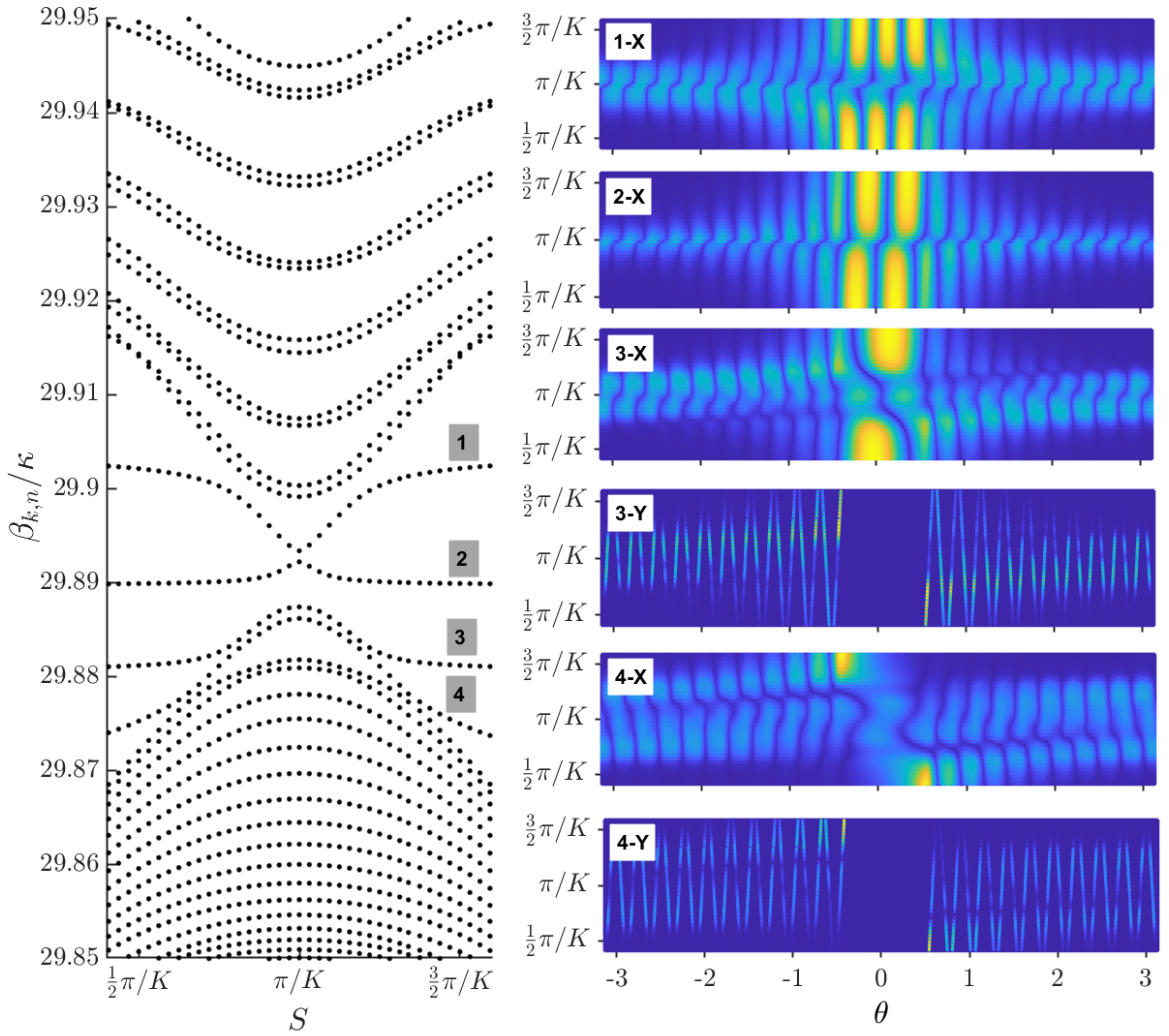

Fig. 3.19 Band structure and eigenstates for the 7-soliton defect crystal are displayed. The eigenvector pairs $[X,Y]^T$ are displayed for four bands labelled from 1 to 4. The phononic waves projected on both eigenvectors give the edge states solely emerging on band number 4, whereas other bands have the distribution of energy in X component sitting between two edge solitons, see $'1-X',{}'2-X',{}'3-X'$. The geometry of the defect crystals is given in Fig.3.18 (a).

crystals in the comparison of the symmetric case (achiral crystal) at $S=\pi/K$ present the butterfly spectrum as shown in Fig.3.20. A group of modes are equally selected from $\mu=360$ to $\mu=1200$. The frequency $\tilde{\omega}_\mu$ is defined as the nonlinearity induced group velocity shift normalized by κ (see F_{d1} in the modelling part). The spectrum marks the growth of frequency offset with increasing mode number $\tilde{\omega}_\mu \sim \mu F_{d1}$, and they are displayed with the subtraction values from the achiral case $S=\pi/K$. Such spectral differences make the double-wings

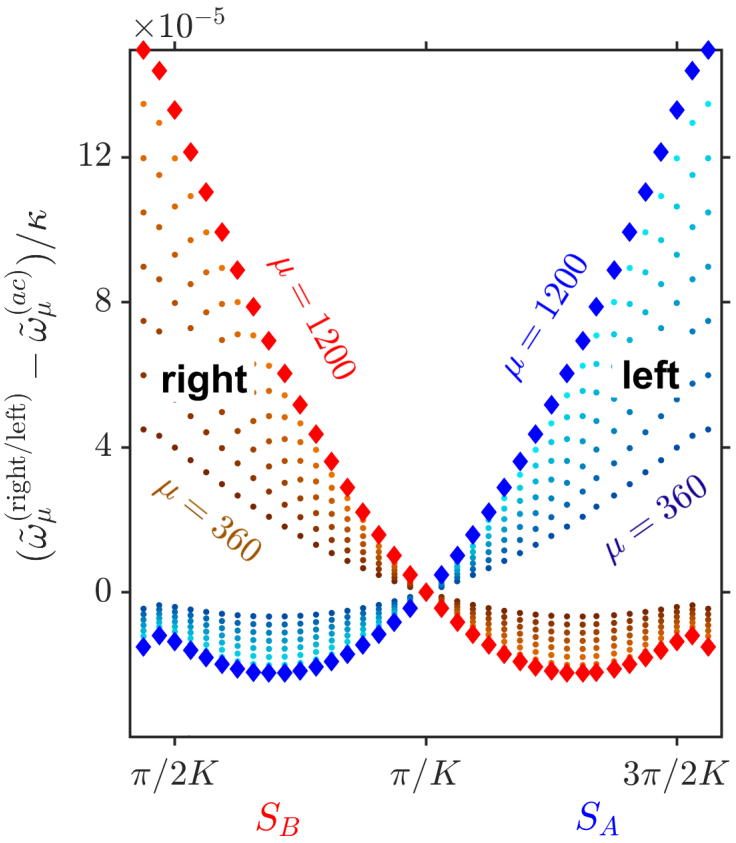

Fig. 3.20 The chirality spectrum presents the butterfly-wings pattern. The vertical axis is defined as the frequency offset between the right, left $\tilde{\omega}^{(right/left)}$ at given mode number μ and the achiral frequency $\tilde{\omega}^{(ac)}$ which is displayed in Fig.3.18(c).

pattern concerning the $S_A = S_B$ case, which reveals the spatio-temporal chirality of the soliton metacrystals.

3.4 Conclusion

To conclude this chapter, we started by introducing the SSH model and applied a similar concept to the soliton crystals in microresonators. Then, we applied the Bloch theorem to study the band structures of the periodic soliton crystals and also for the convenience of computations. The discrete band structure and eigenstates have been demonstrated to be topological by applying the developed geometric phase formulas in the gauge invariant form. The topological phase has been further checked through Wannier functions representation. In particular, we have investigated the relationship between the geometric phase and the Wannier centre under different unit cell selections. Lastly, the topological states were captured by introducing two different defects. With an odd number of solitons' absence, the chirality of the topological soliton crystals and their spectral butterfly signature have been reported.

We point out that the formation of such a topology is fully sustained by the Kerr soliton crystals, differing from the modulations on the materials and complex fabrication of waveguides arrays. The previous reports of the microresonator solitons and topological photonics [30, 31] forecast the applications of classical and quantum information processing based on the soliton metacrystals.

References

[1] D. C. Cole, E. S. Lamb, P. Del'Haye, S. A. Diddams, S. B. Papp, Soliton crystals in Kerr resonators, Nat. Photon. 11, 671676 (2017).

[2] M. Karpov, M. H. P. Pfeiffer, H. Guo et al. Dynamics of soliton crystals in optical microresonators, Nat. Phys. 15, 10711077 (2019).

[3] T. Huang, J. Pan, Z. Cheng et al., Nonlinear-mode-coupling-induced soliton crystal dynamics in optical microresonators, Phys. Rev. A 103, 023502 (2021).

[4] Z. Lu, H. J. Chen, W. Q. Wang, L. Yao, Y. Wang, Y. Yu, B. E. Little, S. T. Chu, Q. Gong, W. Zhao, X. Yi, Y. F. Xiao, and W. F. Zhang, Synthesized soliton crystals, Nat. Commun. 12, 3179 (2021).

[5] H. Taheri, A. B. Matsko, L. Maleki, and K. Sacha, All-optical dissipative discrete time crystals, Nat. Commun. 13, 848 (2022).

[6] W. He, M. Pang, D. H. Yeh et al., Synthesis and dissociation of soliton molecules in parallel optical-soliton reactors. Light Sci. Appl. 10, 120 (2021).

[7] H. Guo, M. Karpov, E. Lucas, A. Kordts, M. H. P. Pfeiffer, V. Brasch, G. Lihachev, V. E. Lobanov, M. L. Gorodetsky, and T. J. Kippenberg, Universal dynamics and deterministic switching of dissipative Kerr solitons in optical microresonators, Nat. Phys. 13, 94 (2017).

[8] N. Batra and G. Sheet, Understanding Basic Concepts of Topological Insulators Through Su-Schrieffer-Heeger (SSH) Model, J of Sci. Edu. 25, 765 (2020).

[9] J. E. Moore, The birth of topological insulators, Nature 464, 194 (2010).

[10] D. Smirnova, D. Leykam, Y. Chong, Y. Kivshar, Nonlinear topological photonics, Appl. Phys. Rev. 7, 021306 (2020).

[11] M. C. Rechtsman, J. M. Zeuner, Y. Plotnik, Y. Lumer, D. Podolsky, F. Dreisow, S. Nolte, M. Segev, and A. Szameit, Photonic Floquet topological insulators, Nature 496, 196 (2013).

[12] T. Ma, A. B. Khanikaev, S. H. Mousavi, and G. Shvets, Guiding electromagnetic waves around sharp corners: Topologically protected photonic transport in metawaveguides, Phys. Rev. Lett. 114, 127401 (2015).

[13] B. Bahari, A. Ndao, F. Vallini, A. E. Amili, Y. Fainman, and B. Kante, Nonreciprocal lasing in topological cavities of arbitrary geometries, Science 358, 636640 (2017).

[14] M. Hafezi, S. Mittal, J. Fan, A. Migdall, and J. M. Taylor, Imaging topological edge states in silicon photonics, Nat. Photonics 7, 1001 (2013).

[15] L. Lang, Y. Wang, H. Wang, Y. D. Chong, Effects of non-Hermiticity on Su-Schrieffer-Heeger defect states, Phys. Rev. B 98, 094307 (2018).

[16] D. Leykam, K. Y. Bliokh, C. Huang, Y. D. Chong, F. Nori, Edge Modes, Degeneracies, and Topological Numbers in Non-Hermitian Systems, Phys. Rev. Lett. 118, 040401 (2017).

[17] S. Malzard, C. Poli, H. Schomerus, Topologically Protected Defect States in Open Photonic Systems with Non-Hermitian Charge-Conjugation and Parity-Time Symmetry, Phys. Rev. Lett. 115, 200402 (2015).

[18] W. P. Su, J. R. Schrieffer, and A. J. Heeger, Solitons in Polyacetylene, Phys. Rev. Lett. 42, 1698 (1979).

[19] J. K. Asbóth, L. Oroszlány, A. Pályi, A Short Course on Topological Insulators, Springer (2016).

[20] P. Parra-Rivas, D. Gomila, L. Gelens, and E. Knobloch, Bifurcation structure of periodic patterns in the Lugiato-Lefever equation with anomalous dispersion, Phys. Rev. E 98, 042212 (2018).

[21] J. Zak, Berry's phase for energy bands in solids, Phys. Rev. Lett. 62, 2747 (1989).

[22] S. Lieu, Topological phases in the non-Hermitian Su-Schrieffer-Heeger model, Phys. Rev. B, 97, 045106 (2018).

[23] G. Dattoli et al., Geometrical phase in the cyclic evolution of nonHermitian systems, J. Phys. A: Math. Gen. 23 5795 (1990).

[24] J. C. Garrison, E. M. Wright, Complex geometrical phases for dissipative systems, 128, Phys. Lett. A 128, 177-181 (1988).

[25] D. V. Skryabin, Instabilities of vortices in a binary mixture of trapped Bose-Einstein condensates: Role of collective excitations with positive and negative energies, Phys. Rev. A 63, 013602 (2000).

[26] M. Atala, M. Aidelsburger, J. Barreiro, et al., Direct measurement of the Zak phase in topological Bloch bands. Nat. Phys. 9, 795800 (2013).

[27] J. Bonini, D. Vanderbilt, and K. M. Rabe, Berry flux diagonalization: Application to electric polarization, Phys. Rev. B 102, 045141 (2020).

[28] Z. Fan, D. N. Puzyrev, D. V. Skryabin, Soliton metacrystals: topology and chirality, arXiv:2208.09750 (2022).

[29] G. H. Wannier, The Structure of Electronic Excitation Levels in Insulating Crystals, Physical Review. 52 (3): 191197 (1937).

[30] S. Mittal, E. A. Goldschmidt, and M. Hafezi, A topological source of quantum light, Nature 561, 502 (2018).

[31] M. A. Guidry, D. M. Lukin, K. Y. Yang, R. Trivedi, and J. Vuckovic, Quantum optics of soliton microcombs, Nat. Photon. 16, 52 (2022).

Chapter 4

Frequency combs in $\chi^{(2)}$ resonators

4.1 Introduction

In this chapter, we will consider the OPO frequency comb generations in $\chi^{(2)}$ resonators. The phase matching condition has been achieved for pump and signal fields at $1556nm$ and $3112nm$ in a $CdSiP_2$ resonator with a radius of $560\mu m$. The mid-infrared comb has been observed experimentally by our colleagues at the University of Freiburg and demonstrated in numerical simulations by us. Below, We will focus on the theoretical part including the modelling, mathematical analyses and simulations. The experimental operations can be found in our manuscript [1].

4.1.1 Background

While the Kerr frequency combs have proven significant in a wide range of applications, there are still many merits of the $\chi^{(2)}$ medium to be a better choice. Two major advantages of the $\chi^{(2)}$ nonlinear process are the low input power threshold and the immediate octave-wide frequency conversion, where the former conduces to the thermal-controlled integrated circuit, and the latter helps the comb generation in mid-IR and visible ranges. Mid-IR sources are crucial and favoured in many applications, spanning from communications, spectroscopy, biology sample analysis, material detection, environment monitoring, and so on [2–9]. All these can be summarized as the spectrum identification in the given sample, resulting from the energy absorption of chemical bonds in the materials covering most glasses, polymers, and biological tissues with the fundamental vibration resonances located within the mid-IR range. The octave-wide generation also brings convenience to the self-referencing process compared to the Kerr combs [10]. Beside, various materials have been used, including lithium niobate (LN), aluminium nitride (AlN), gallium phosphate (GaP), and cadmium

silicon phosphide ($CdSiP_2$) etc.. The first realization of parametric down conversion in a spherical phase-matched *LN* resonator shows the photon transition from the pump at 532nm to the signal and idler pairs around 1064 nm with a low-threshold of 6.7 μW and narrow linewidth below $10MHz$ [11], where the power threshold is mainly dominated by the losses at the pump and harmonic fields as well as the nonlinearity strength [12]. Recent work reports the first demonstration of OPO ($780nm$ to $1560nm$) in a waveguide integrated *AlN* microring resonator with output power above $10mW$. The demonstrated energy conversion efficiency can reach up to 17% with reduced power threshold due to the significantly smaller mode volume, which serves as an ideal platform for future integrated nano-photonic devices [13]. Below, our study is based on the birefringence matching in a $CdSiP_2$ resonator. $CdSiP_2$ exhibits attractive properties for the mid-IR generation due to its wide transparent range (from $0.5-9\mu m$), high birefringence factor $n_e - n_o = -0.05$, large nonlinear coefficient ($d_{36} = 84.5pm/V$), as well as its sensitive thermal response [14]. All these remarkable features help and enable the mid-IR spectrum generation with the pump at $1.55\mu m$.

Different from the difference frequency generation (DFG) [15–18], the OPO process is initialized with vacuum signal and idler photons. The process starts from one photon at pump frequency splitting into the pair of signal and idler photons governed by the energy conservation and the newly generated photons provide increasing combinations of the sum and difference frequency conversions. Phase matching is critical in the whole cascaded process and governs the frequency conversion efficiency. Usually, it can be satisfied either through the quasi-phase-matching or using different polarizations in a birefringence material. Photon excitation can be identified through the similar modulational instability approach introduced in $\chi^{(3)}$ microresonators above.

4.1.2 Experimental method

The basic procedures concerning the fabrication and measurements are addressed below. The phase matching condition in the $CdSiP_2$ resonator is fulfilled through the birefringence between the ordinary and extraordinary polarizations, in relation to the signal and pump fields, respectively. The resonator is cut using a femtosecond laser operating at 2kHz repetition rate with wavelength of $\lambda = 388nm$ and the output power around $300mW$. The pre-made resonator with a radius of $560\mu m$ is further polished by the diamond slurry for the smoothness. The measurement platform is set up with a CW pump operating at $1556nm$, with the e-polarized source coupling into the resonator through a prism. At the output port, the mixture of e-polarized and o-polarized fields will be separated through a dispersive prism and recorded by two optical spectrum analyzers (OSAs). Temperature is stabilized and tuned in the mK scale during the measurements. The initial temperature is around $360K$, close to

the degeneracy point where the corresponding refractive indices for e- and o-polarized lights can be found in [19]. The measured and estimated parameters in the table [1] are taken in our studies. The nonlinearity factors are obtained from COMSOL [20]. Dispersion factors are calculated with the Sellmeier equations [21].

	Pump (1556 nm)	Signal (3112 nm)
Repetition rate	$D_{1p}/2\pi$ =27.06 GHz	$D_{1s}/2\pi$ =27.57 GHz
Dispersion	$D_{2p}/2\pi = -378$ kHz	$D_{2s}/2\pi = -164$ kHz
Linewidth	$\kappa_p/2\pi$ =55 MHz	$\kappa_s/2\pi$ =64 MHz
Nonlinearity	$\gamma_p/2\pi$ =1 GHz W$^{-1/2}$	$\gamma_s/2\pi$ =2 GHz W$^{-1/2}$

Table 4.1 Resonator parameters.

4.2 Model and methods

In this section, we map the half harmonic generation as illustrated in Fig4.1.

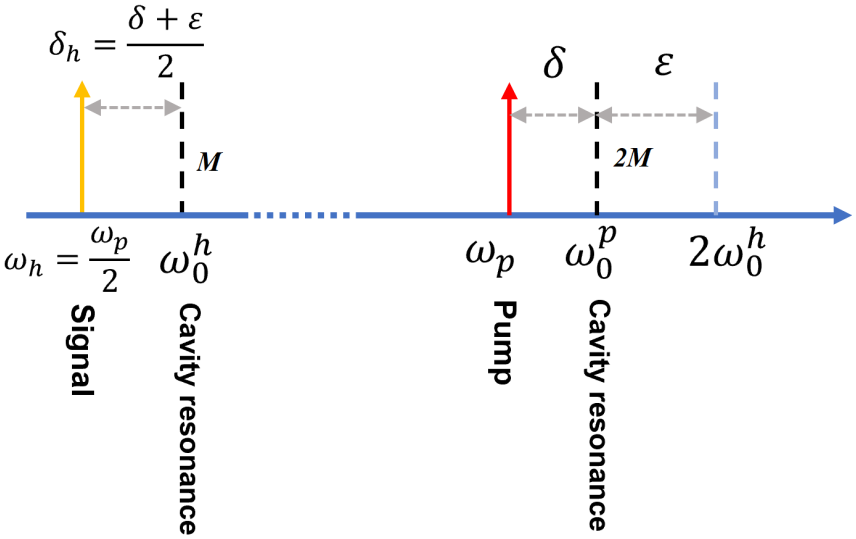

Fig. 4.1 The sketch shows half harmonic generation and the notation definitions.

We define the following notations: the pump and signal (half-harmonic) envelopes of ψ_p, ψ_h, respectively; the optical cavity modes M and $2M$ shown by the dashed black lines with frequencies of ω_0^h and ω_0^p. Note that the exact frequency for mode number M can be computed through its free-spectral range by multiplying the exact mode number, which is governed by radius and the light speed. Assume the effective refractive indices n_M, n_{2M} for

modes M and $2M$, symbol c for light speed in vacuum and R for microresonator radius, the resonances ω_0^h, ω_0^p can be written as:

$$\omega_0^h = M \times \frac{c}{Rn_M} \tag{4.1}$$

$$\omega_0^p = 2M \times \frac{c}{Rn_{2M}} \tag{4.2}$$

The phase matching condition gives $n_M = n_{2M}$, $\omega_0^h = \frac{1}{2}\omega_0^p$. The mismatch is then $\varepsilon = 2\omega_0^h - \omega_0^p$. Experimentally, ε is a controllable parameter highly dependent on temperature, see [22]. The resonator frequencies for signal and pump fields are written as (note μ is the relative mode index, distinguished from the absolute mode index M):

$$\omega_\mu^h = \omega_h + D_1^h \mu + D_2^h \mu^2 \tag{4.3}$$

$$\omega_\mu^p = \omega_p + D_1^p \mu + D_2^p \mu^2 \tag{4.4}$$

where $D_1^{h,p}/2\pi, D_2^{h,p}$ are the FSRs and dispersions for the signal and pump fields. The detuning is defined for the pump component $\delta = \omega_0^p - \omega_p$, and for the half harmonic field is $\delta_h = \frac{\delta+\varepsilon}{2}$. Given the notations above, the OPO process can be mapped by the following Lugiato-Lefever equations:

$$\begin{aligned} i\partial_t \psi_h &= \left(\frac{\delta+\varepsilon}{2} - iD_1^h \partial_\theta - \frac{1}{2}D_2^h \partial_\theta^2\right)\psi_h - \frac{i\kappa_h}{2}\psi_h - \gamma_h \psi_p \psi_h^* \\ i\partial_t \psi_p &= \left(\delta - iD_1^p \partial_\theta - \frac{1}{2}D_2^p \partial_\theta^2\right)\psi_p - \frac{i\kappa_p}{2}(\psi_p - \mathscr{H}) - \gamma_p \psi_h^2 \end{aligned} \tag{4.5}$$

The scripts of h, p mark the half harmonic and pump fields. $\kappa_{h,p}$ are the linewidth; $\gamma_{h,p}$ are the strength of the nonlinearity. $\mathscr{H}$ is the pump parameter connected to the pump power $\mathscr{W}$ through the relation [20]:

$$\mathscr{H}^2 = \frac{D_1^p \mathscr{W}}{2\pi\kappa_p} \tag{4.6}$$

The walk-off induced by the $D_1^p \neq D_1^h$ should be compensated by the nonlinearity for a steady non-homogeneous state, leading to an extra physical parameter $V = D_1^h - D_1$, where D_1 is

defined as the locked repetition rate of the pump and signal fields. It transfers the model into:

$$\begin{aligned} i\partial_t \psi_h &= \left(\frac{\delta+\varepsilon}{2} - i(D_1^h - D_1)\partial_\theta - \frac{1}{2}D_2^h\partial_\theta^2\right)\psi_h - \frac{i\kappa_h}{2}\psi_h - \gamma_h\psi_p\psi_h^* \\ i\partial_t \psi_p &= \left(\delta - i(D_1^p - D_1)\partial_\theta - \frac{1}{2}D_2^p\partial_\theta^2\right)\psi_p - \frac{i\kappa_p}{2}(\psi_p - \mathscr{H}) - \gamma_p\psi_h^2 \\ D_{off} &= D_1^p - D_1^h \end{aligned} \tag{4.7}$$

For the simplicity of the following expressions, we define the operators below:

$$\begin{aligned} \hat{L_p} &= \delta - \frac{1}{2}D_2^p\partial_\theta^2 \\ \hat{L_h} &= \frac{\delta+\varepsilon}{2} - \frac{1}{2}D_2^h\partial_\theta^2 \\ \hat{G_p} &= (D_{off}+V)\partial_\theta + \frac{\kappa_p}{2} \\ \hat{G_h} &= V\partial_\theta + \frac{\kappa_h}{2} \end{aligned} \tag{4.8}$$

With the operators, we have:

$$\begin{aligned} i\partial_t \psi_p &= \left(\hat{L_p} - i\hat{G_p}\right)\psi_p + \frac{i\kappa_p}{2}\mathscr{H} - \gamma_p\psi_h^2 \\ i\partial_t \psi_h &= \left(\hat{L_h} - i\hat{G_h}\right)\psi_h - \gamma_h\psi_p\psi_h^* \end{aligned} \tag{4.9}$$

To determine the unknown locked repetition rate V, we can set the maximal peak in the spatial form of solution at $\theta = 0$, and add the constraint of $\partial\left(Re(\psi_p)\right)|_{\theta=0}$. This condition ensures the spatial location during the convergence iterations. Physically, the moving frame with the locked velocity D_1 shows the static waveforms.

Assume the stationary solutions with small perturbations are $\psi_p = (a+ib)+(p+iq)$, $\psi_h = (c+id)+(m+in)$ and $V = V_0 + s$, where a,c and b,d are the real and imaginary parts of the stationary parts of pump and signal fields with the same definition for perturbations by p,q,m,n. V_0 is a solvable parameter with a slight deviation s. Substitute the ansatz into the stationary model ($\partial_t = 0$) and divide the model into real and imaginary parts:

$$\begin{aligned} \hat{L_p}a + \hat{G_p}b - \gamma_p(c^2 - d^2) &= 0 \\ \hat{L_p}b + \hat{G_p}a - \gamma_p(2cd) + \frac{\kappa_p}{2}\mathscr{H} &= 0 \\ \hat{L_h}c + \hat{G_h}d - \gamma_h(ac+bd) &= 0 \\ \hat{L_h}d + \hat{G_h}c - \gamma_h(bc-ad) &= 0 \\ \partial a|_{\theta=0} &= 0 \end{aligned} \tag{4.10}$$

The Jacobian $\hat{J}$ for the above equations is:

$$\hat{J}\begin{bmatrix} p \\ q \\ m \\ n \\ s \end{bmatrix} = \begin{bmatrix} \hat{L_p} & \hat{G_p} & -2\gamma_p c & 2\gamma_p d & \partial_\theta b \\ -\hat{G_p} & \hat{L_p} & -2\gamma_p d & -2\gamma_p c & -\partial_\theta a \\ -\gamma_h c & -\gamma_h d & \hat{L_h} - \gamma_h a & \hat{G_h} - \gamma_h b & \partial_\theta d \\ \hat{\gamma_h} d & -\gamma_h c & -\hat{G_h} - \gamma_h b & \hat{L_h} + \gamma_h a & -\partial_\theta c \\ \vec{Q} & \vec{0} & \vec{0} & \vec{0} & 0 \end{bmatrix} \begin{bmatrix} p \\ q \\ m \\ n \\ s \end{bmatrix} \tag{4.11}$$

Define vector $\vec{\rho} = [p, q, m, n, s]^T$ and number of modes N, the vector size is $4N+1$. Thus, the Jacobian matrix size is $(4N+1) \times (4N+1)$. Matrix kernels $\hat{J}_{i,j}$ are the size of $N \times N$ when $i, j \in [1,4]$, whereas the last column and last row are different. For example, the element $\hat{J}_{1,5}$ is a $N \times 1$ vector. And in the 5th row, the vector $\vec{0}$ is a $1 \times N$ vector with all zeros. $\vec{Q}$ is a row vector arranged for computing the derivative of vector p at index $\theta = 0$. Given 512 discrete points in the range of $\theta \in [-\pi, \pi)$, the index of 256 corresponds to the point $\theta = 0$. If the finite difference method is taken to deal with the derivative, such a vector is in form of $[0, 0, \cdots, -1/2, 0, 1/2, \cdots, 0, 0]$, where the non-zero terms should act on the p element with indices of $255, 256, 257$. With the Jacobian, Eq.4.10 can be solved by Newton's method as introduced in the appendix.

4.3 OPO comb generation

We discuss two regimes of the OPO comb generations, whose main difference is caused by the parity of the absolute pump mode index in the resonator. Both regimes present similar ordinary and staggered spectra, but the degenerate conversion only happens when pumping at even indices.

4.3.1 Pumping an even mode

In the last section, we have developed the model of resonators pumped at an even mode indices. To simulate the sideband generations, we implement numerical simulation of Eq.4.5 with the input below:

$$\psi_p = \frac{-i\frac{\kappa_p}{2}\mathscr{H}}{\delta - i\frac{\kappa_p}{2}}, \psi_h = 0 \tag{4.12}$$

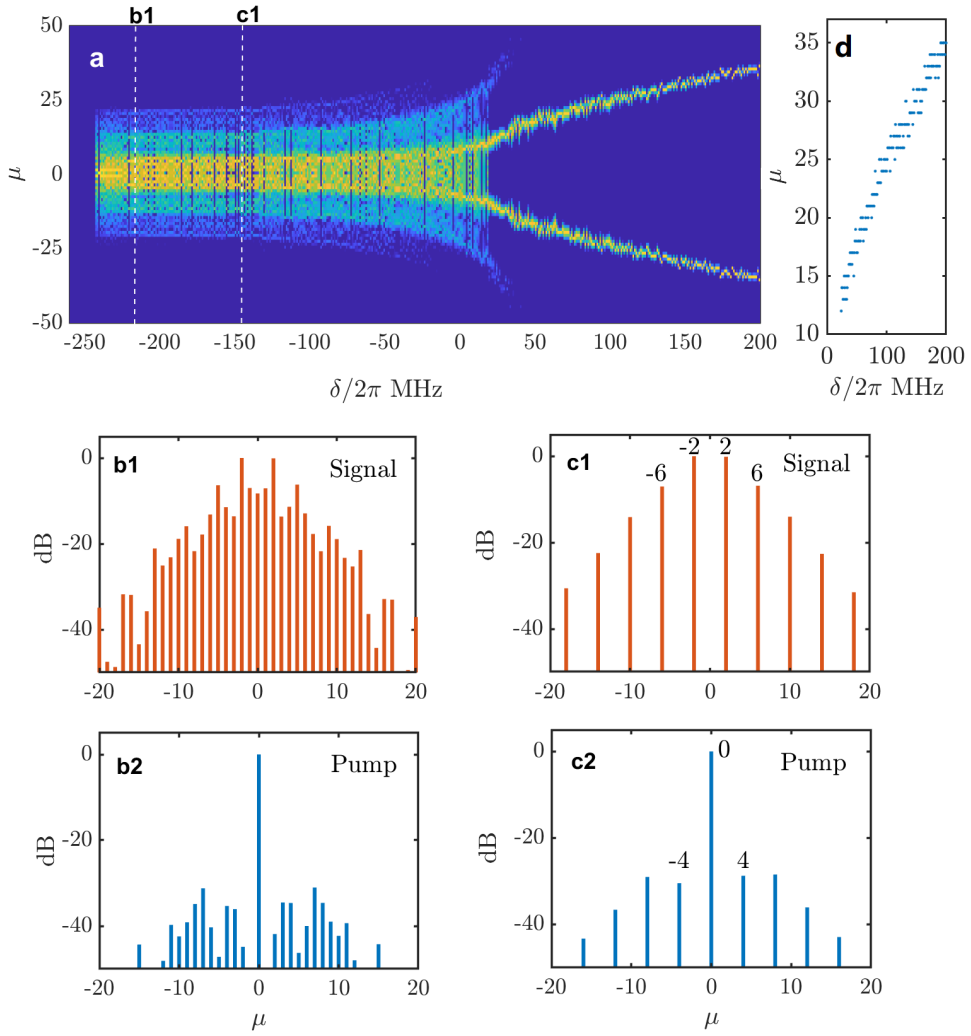

Fig. 4.2 (a) The signal component spectra carpet is displayed with resolution of 1MHz on a background (blue) level of -70dB. (b1, b2) show the ordinary spectra of the OPO comb, where the spacing in either signal and pump component is $\Delta\mu = 1$. (c1, c2) present staggered OPO spectrum with $\Delta\mu = 4$. The signal spectra are selected as marked by the white dashed lines in panel(a) with $\delta/2\pi = -216, -144MHz$, respectively. (d) presents the ladder-step transition of the sideband modes with highest intensity in the detuning range $\delta/2\pi \in [20, 200]$ MHz. Parameters: frequency mismatch $\varepsilon = 0$; Pump power $\mathscr{W} = 4mW$.

Eq.4.12 is obtained by applying $\partial_t = 0, \partial_\theta = 0$ for the homogeneous pump field circulating in the resonator. The excitation of sideband modes can be considered by adding slight perturbations to the pump field and by means of the dynamical simulations, we will find the output spectrum for each fixed detuning. In Fig.4.2 (a), we have collected hundreds of such spectral outputs for each fixed detuning on the carpet of a noise level at -70dB. The ordinary spectra in Fig.4.2 (b1,b2) show the spacing of the free spectral range $\Delta\mu = 1$. As a comparison, the staggered combs in Fig.4.2 (c1,c2) are quite unusual due to the absence of the central mode $\mu = 0$ in the signal field. Besides, Fig.4.2 (a) indicates the occurrence of the ordinary and staggered states is not deterministic. In the simulation, we found it depends on the excitations, i.e., the strength and the distribution of perturbations. Although the output spectrum for a fixed detuning is optional, the robustness of both combs is remarkable, i.e., once the comb is formed, it will stay the same distribution with continuous change in detuning for tens of MHz. Aside from the comb-like spectra, on the right side of the carpet, we observed the splitting of the excited modes with incremental detuning $\delta/2\pi \in [20, 200]$MHz. The distribution displays a ladder-like transition in panel (d). The formation of the two excited wings is associated with the tongue-like instability as we mentioned in in chapter 2. Specifically, the excitation of the mode numbers μ are moving with the tongue indices along the detuning.

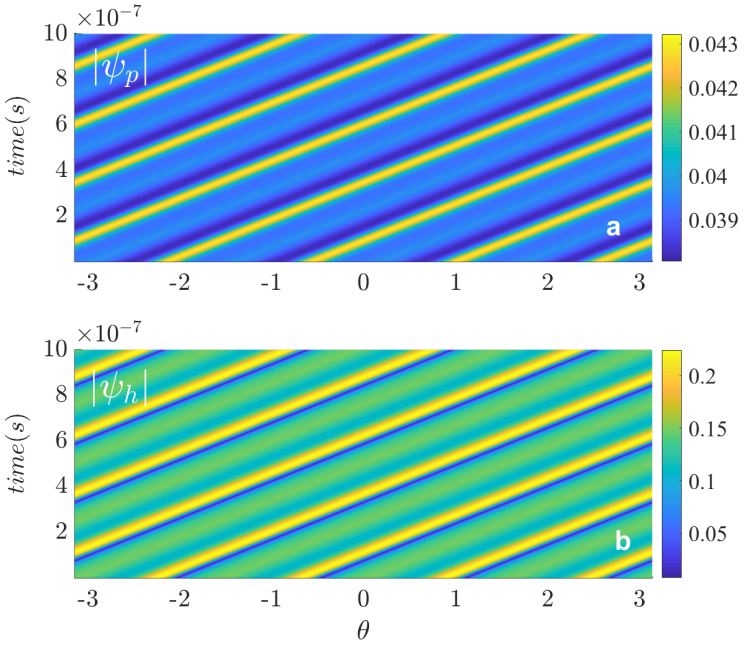

Fig. 4.3 The mode-locked dynamics relates to the case in Fig.4.2 (c1,c2). The reference frame is rotating at D_1^h and the locked repetition rates in two components reveal the locked FSR deviate from D_1^h.

In Fig.4.3, we have captured a short range of the dynamical simulation for staggered combs in relation to Fig.4.2 (c1, c2). In the spatial domain of these staggered combs, both fields are shown in the top view where the high intensity is shaded in bright yellow. Both pump and signal fields are moving in the same tilted direction with the same angle of the yellow columns, which implies their repetition rates are locked. From the modelling, we mentioned the rotation velocity of the coordinate is chosen at D_1^h. Therefore, the locked speed from the dynamics can be easily estimated by $V = -\Delta\theta/\Delta t$.

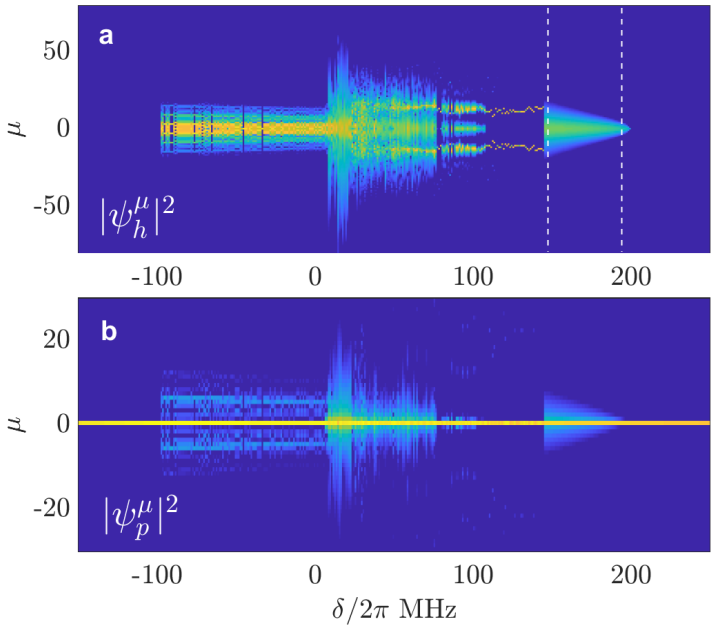

Fig. 4.4 Soliton spectra are obtained in the half harmonic field after the ladder step transition range. Parameters: $\varepsilon/2\pi = -0.5GHz$; Pump power $\mathscr{W} = 4mW$.

Fig.4.4 presents the soliton combs with non-zero mismatch ε. The staggered and ordinary combs are similar to the above observations. After the ladder-step transition between $\delta/2\pi \in (110, 140)MHz$, the soliton combs are emerging. The occurrence of solitons is understood by distict modulation instability structures under different choices of ε [23]. Here, the spectral carpet for both pump and signal are displayed. From the pump component at the bottom panel, the solid yellow line at $\mu = 0$ (compared to the weak blue wings $\mu \neq 0$) indicates the zero mode is the most dominant one. Specifically, in Fig.4.5, two cases with wide and narrow soliton profiles are given, in conjunction with the two white dashed lines in Fig.4.4 (a). The soliton comb is typical in the signal field, whereas the spectrum of pump field shows a much higher zero mode than its sidebands, implying the roughly CW-like spatial distribution as presented in Fig.4.5 (a3, b3). The flat spatial distribution (CW-like

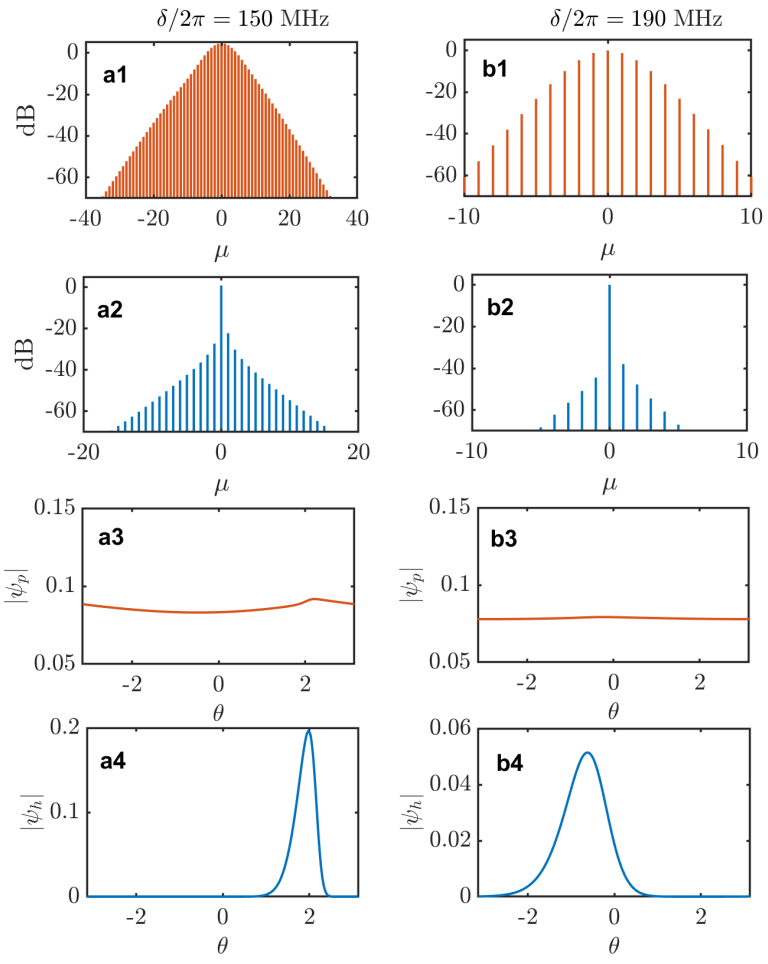

Fig. 4.5 Typical examples of soliton spectrum and spatial profiles are captured. Panels (a) and (b) show the sharp and fat soliton cases, respectively. They are related to the white line marked in Fig.4.4.

profile) of the pump field may approximately ignore the spatial derivatives in Eq.4.5, which directly links ψ_h^2 and ψ_p in the form of $\psi_p = c_1\psi_h^2 + c_2$ (c_1, c_2 are constants). This relation can effectively transform the dual-component model into one component system governed by ψ_h with Kerr nonlinearity. This hypothesis provides an estimation of inputs that used for the convergence. The triangle-shaped spectral carpet indicates the decaying sideband intensity for both fields with incremental detuning. Different from the combs generated in the negative detuning where ordinary comb and staggered comb are mixed, the soliton combs are reproducible and deterministic. In Fig.4.6, we have captured the stationary solution converged by Newton's algorithm. The numerical approach is quite straightforward, we seed any of the spectrums from the dynamical scans as well as its corresponding velocity $'V'$.

Then, the branch of stationary solutions is tracked by increasing and decreasing the detuning until both sides end with no solutions. The soliton existence range is highly matched to the dynamical outputs in Fig.4.4. Fig.4.6 (a) shows the decaying rate of mode $\mu = 1$ for both fields. $\mu = 1$ is the second largest intensity mode in the spectrum, therefore, it shows the transition of the soliton gradually decaying to the CW state with increasing detuning $\delta/2\pi$ reaching to 200MHz near the right boundary. In particular, when $\delta/2\pi > 190MHz$, the pump field can be well approximated by a single mode which coincides with our hypothesis. The width of the spectra is recorded in Fig.4.6 (b), with two background levels of -100dB and -70dB. The former level presents the finer step transitions along detuning, whereas the -70dB standard provides less resolution.

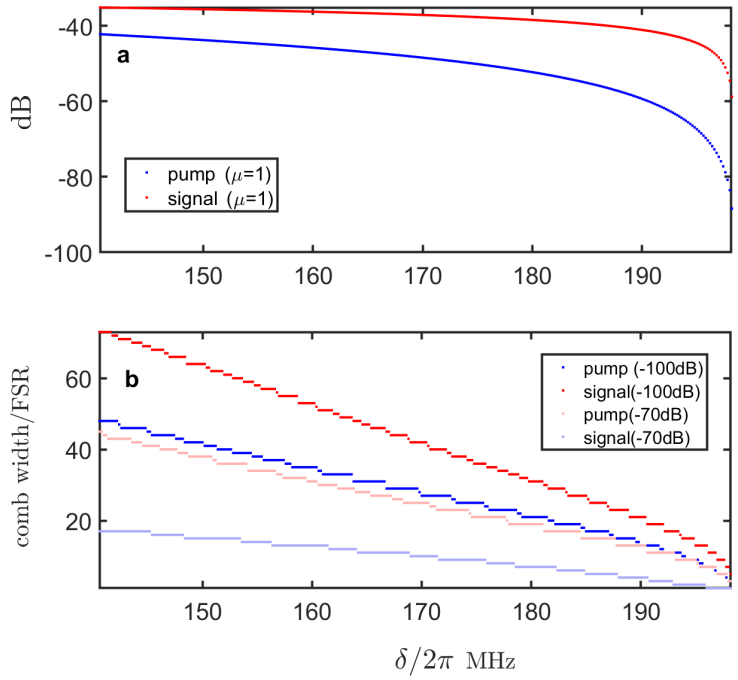

Fig. 4.6 Steady soliton solutions are computed with Newton algorithm. Panel (a) shows the decaying rate of mode $\mu = 1$. Panel (b) presents the comb widths at pump and signal fields in (faint) blue and (faint) red, respectively. The FSRs are counted by selecting noise levels at -100dB and -70dB, respectively.

4.3.2 Pumping an odd mode

When the resonator is pumped at an odd longitudinal mode, the model is mapped by the pair of equations:

$$\begin{aligned} i\partial_t \psi_h &= \left(\omega_0^h - \tfrac{1}{2}\omega_p - iD_1^h\partial_\theta - \frac{1}{2}D_2^h\partial_\theta^2\right)\psi_h - \frac{i\kappa_h}{2}\psi_h - \gamma_h\psi_p\psi_h^* \\ i\partial_t \psi_p &= \left(\omega_0^p - \omega_p - iD_1^p\partial_\theta - \frac{1}{2}D_2^p\partial_\theta^2\right)\psi_p - \frac{i\kappa_p}{2}\left(\psi_p - \mathscr{H}e^{il\theta}\right) - \gamma_p\psi_h^2 \end{aligned} \tag{4.13}$$

where l defines the index of mode to be pumped. $l = 1$ means the pump is tuned to the mode at an odd index $\mu = 1$. ω_0^h, ω_0^p are the cavity resonances at $\mu = 0$. The spectrum coordinate is centralized at $\mu = 0$, with the residual dispersion subjected to the relation $\omega_\mu^p = \omega_p + D_1^p\mu + \frac{1}{2}D_2^p\mu^2$. Therefore, if we keep the detuning defined with respect to ω_0^p, the actual detuning between the pump and ω_1^p should be:

$$\delta' = \delta + D_1^p + \frac{1}{2}D_2^p \tag{4.14}$$

where

$$\delta = \omega_0^p - \omega_p \tag{4.15}$$

$$\delta' = \omega_1^p - \omega_p \tag{4.16}$$

This relation can also be derived from the exponential phase term in Eq.4.13. The momentum conservation between pump and signal fields satisfies:

$$2M + 1 = (M + \mu) + (M + 1 - \mu) \tag{4.17}$$

where M, μ are the absolute longitudinal mode index and relative mode index. Eq.4.17 shows when the resonator is pumped in an odd mode, different from pumping the even mode, there is no degenerate mode generation.

We have implemented the dynamical scans based on Eq.4.13 in the similar approach used in the last section. In Fig.4.7, we collect the spectral outputs of six hundred independent simulations at each fixed detuning δ. The numerical scans demonstrate the existence of ordinary and staggered combs mixed in the range $\delta/2\pi \in [-150, 0]$ MHz. The typical spectral distributions are displayed in panels (b1, b2) and (c1, c2). From the numerical observation, both ordinary and staggered combs are robust in the millisecond simulations. We should mention their stability has also been demonstrated in the experiment [1]. However, we found quite noisy spectrums within the range $\delta/2\pi \in [50, 270]$ MHz where one cannot

find stable comb states. The typical dynamics is displayed in Fig.4.8 (a, b). Remember the coordinate is rotating at D_1^h, which helps to track the motion in a relatively large time scale. The dynamics present in both fields share a roughly locked repetition rate, but they are weakly unstable with irregular oscillations. We track the oscillating frequency by computing the integral energy changing with time with the formula:

$$\begin{aligned} f_{osc.} &= 10 \cdot \lg\left(|\frac{1}{N}\mathscr{F}\{P(t)\}|^2\right) \\ P(t) &= \int_0^{2\pi} |\psi_h(\theta,t)|^2 d\theta \end{aligned} \tag{4.18}$$

N is the normalization coefficient for discrete Fourier transformation, which equals the number of discrete points used for the computation. $\mathscr{F}$ is the Fourier transform operator. $f_{osc.}$ computes the oscillation frequency of integral energy $P(t)$. For the steady evolution, $P(t)$ should be a constant along time, thus the spectrum should be zero apart from the zero frequency element. In panel(c), we have calculated 46 unstable cases with the selection of the oscillating frequency in relation to the highest sideband peaks. Fig.4.8(d) presents a typical spectrum for $f_{osc.}$, and it shows there are several competing frequencies below 0.25 GHz.

4.4 Conclusion

In this chapter, we first introduced the modelling for the OPO comb generations. Aside from the ordinary spectral distribution, the staggered one is the first time demonstrated both numerically and experimentally. Next, we reported different regimes of frequency combs along the detuning, including the mixture of ordinary and staggered combs, the ladder transition of sideband excitations and the soliton combs. In particular, the soliton comb generation is deterministic and spans over 70 FSRs. The forecasting mechanism of the soliton generation is associated with the mismatch ε where it deforms the instability structure for sideband modes. We point out the mechanism of the soliton formation is vital for state-of-the-art $\chi^{(2)}$ soliton combs and is worth further investigations in an independent research. It would be crucial for efficient OPO conversions and being a steady source for integrated mid-IR devices. In the last section, we include the discussion of pumping the resonator at an odd mode index. The modified modelling has extended this topic, in particular, we found a range where the combs are weakly unstable with the integral energy oscillating in MHz to GHz level.

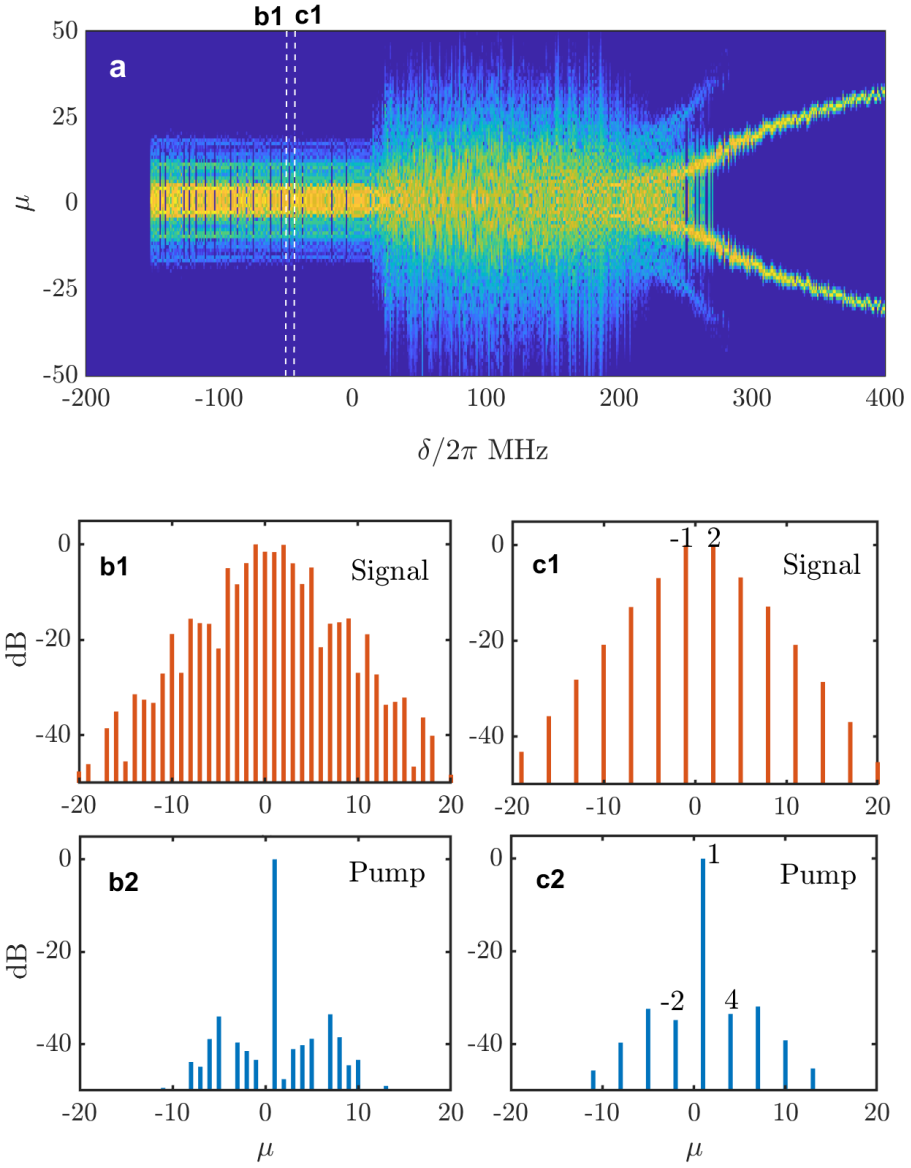

Fig. 4.7 (a) The signal component spectra carpet is displayed with resolution of 1MHz on a background (blue) level of -70dB. (b1, b2) show the ordinary spectra of the OPO comb, where the spacing in either signal and pump component is $\Delta\mu = 1$. (c1, c2) present staggered OPO spectra with $\Delta\mu = 3$. The odd case will be asymmetric and distinct from the spectra in Fig.4.2. The signal spectra are marked by the white dashed lines in panel (a) at $\delta/2\pi = -50, -44MHz$, respectively. Parameters: frequency mismatch $\varepsilon/2\pi = -0.75GHz$; Pump power $\mathscr{W} = 4mW$.

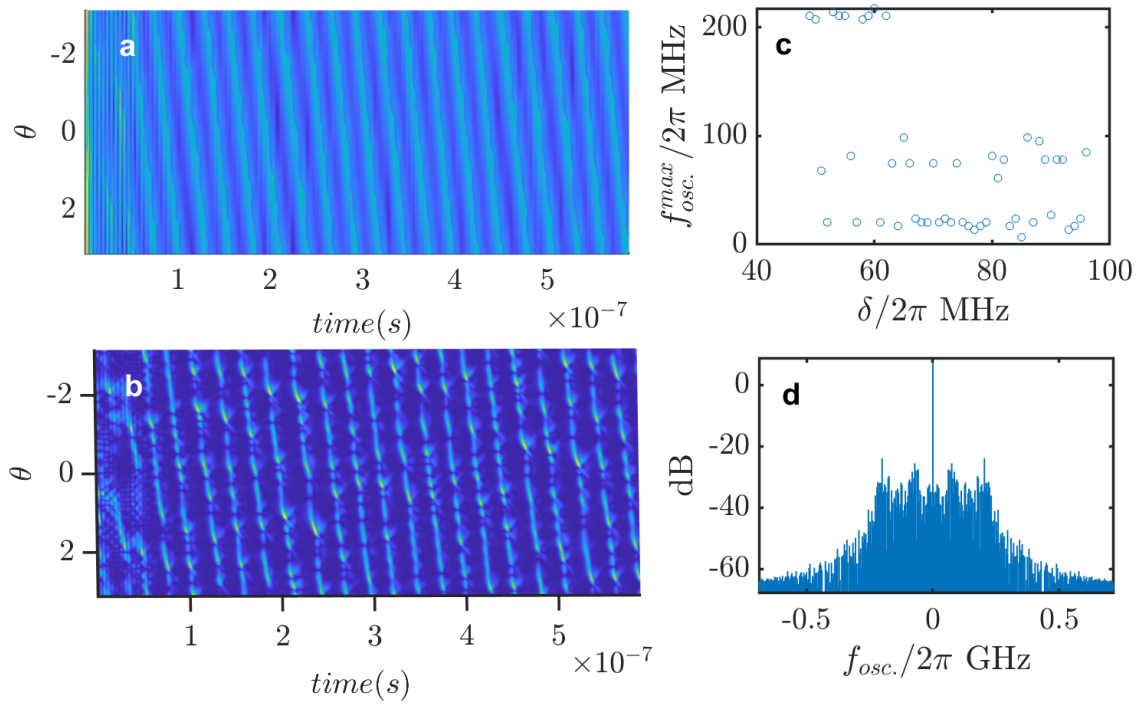

Fig. 4.8 Typical unstable combs at $\delta/2\pi = 68MHz$. Panels(a, b) show pump and signal fields, respectively. Panel(c) selects 46 cases in the unstable region with the dots marking the maximal oscillating frequency in each dynamics. Panel(d) is one typical spectrum of the oscillating frequency obtained from panel(b).

References

[1] N. Amiune, Z. Fan, V. V. Pankratov, D. N. Puzyrev, D. V. Skryabin, K. T. Zawilski, P. G. Schunemann, I. Breunig, Mid-infrared frequency combs and staggered spectral patterns in $\chi^{(2)}$ microresonators, arXiv:2205.12776 (2022).

[2] A. Shelkovnikov, R. J. Butcher, C. Chardonnet, A. A. Klein, Stability of the proton-to-electron mass ratio. Phys. Rev. Lett. 100, 150801 (2008).

[3] T. Ideguchi, A. Poisson, G. Guelachvili, N. Picqué, T. W. Hänsch, Adaptive real-time dual-comb spectroscopy. Nature Communications 5, 3375 (2014).

[4] N. S. Prasad, Optical communications in the mid-wave IR spectral band, In: Free-space laser communications. Optical and fibre communications reports, 2, 347-391 (2005).

[5] A. A. Klein, et al., Absolute frequency measurement of a SF6 two-photon line by use of a femtosecond optical comb and sum-frequency generation, Opt. Lett. 30, 33203322 (2005).

[6] M. A. Pleitez et al., Label-free metabolic imaging by mid-infrared optoacoustic microscopy in livings cells, Nature biotechnology 38, 293-296 (2019).

[7] I. Coddington, W. C. Swann, N. R. Newbury, Coherent multiheterodyne spectroscopy using stabilized optical frequency combs, Phys. Rev. Lett. 100, 013902 (2007).

[8] M. Brehm, A. Schliesser, F. Keilmann, Spectroscopic near-field microscopy using frequency combs in the mid-infrared. Opt. Express 14, 1122211233 (2006).

[9] F. K. Tittel, Mid-infrared Laser Based Gas Sensor Technologies for Environmental Monitoring, Medical Diagnostics, Industrial and Security Applications, Terahertz and Mid Infrared Radiation: Detection of Explosives and CBRN (Using Terahertz) (2014).

[10] X. Xue, X. Zheng, A. M. Weiner, Soliton trapping and comb self-referencing in a single microresonator with $\chi^{(2)}$ and $\chi^{(3)}$ nonlinearities, Opt. Lett. 42, 41474150 (2017).

[11] J. U. Furst et al., Low-threshold Optical Parametric Oscillations in a Whispering Gallery Mode Resonator, Phys. Rev. Lett. 105, 263904 (2010).

[12] V. S. Ilchenko et al., Low-threshold parametric nonlinear optics with quasi-phase-matched whispering-gallery modes, J. Opt. Soc. Am. B, 20, 1304 (2003).

[13] A. W. Bruch et al., On-chip $\chi^{(2)}$ microring optical parametric oscillator, Optica 6, 1361 (2019).

[14] P. G. Schunemann, K. T. Zawilski, T. M. Pollak, V. Petrov, D. E. Zelmon, CdSiP2: a new nonlinear optical crystal for 1- and 1.5-micron-pumped mid-IR generation, Advanced Solid-State Photonics, TuC6 (2009).

[15] P. Maddaloni, P. Malara, G. Gagliardi, P. Natale, Mid-infrared fibrebased optical comb. New J. Phys. 8, 262 (2006).

[16] E. Baumann, et al., Spectroscopy of the methane ν_3 band with an accurate mid-infrared coherent dual-comb spectrometer, Phys. Rev. A 84, 062513 (2011).

[17] A. Sell, R. Scheu, A. Leitenstorfer, R. Huber, Field-resolved detection of phase-locked infrared transients from a compact Er:fiber system tunable between 55 and 107 THz. Appl. Phys. Lett. 93, 251107 (2008).

[18] C. Erny, et al., Mid-infrared difference-frequency generation of ultrashort pulses tunable between 3.2 and 4.8 μm from a compact fiber source, Opt. Lett. 32, 11381140 (2007).

[19] J. Wei et al., Measurement of refractive indices of $CdSiP_2$ at temperatures from 90 to 450 K, Opt. Mater. Express 8, 235-244 (2018).

[20] D. V. Skryabin, Coupled-mode theory for microresonators with quadratic nonlinearity, J. Opt. Soc. Am. B 37, 2604 (2020).

[21] V. Kemlin et al.,Nonlinear, dispersive, and phase-matching properties of the new chalcopyrite $CdSiP_2$ (Invited), Opt. Mater. Express 1, 1292-1300 (2011).

[22] N. Amiune, D. N. Puzyrev, V. V. Pankratov, D. V. Skryabin, K. Buse, I. Breunig, Optical-parametric-oscillation-based $\chi^{(2)}$ frequency comb in a lithium niobate microresonator, Opt. Express 29, 41378 (2021).

[23] D. N. Puzyrev, D. V. Skryabin, Ladder of Eckhaus instabilities and parametric conversion in $\chi^{(2)}$ microresonators, Commun. Phys. 5, 138 (2022).

Chapter 5

Summary

In the above chapters, we have discussed three major cases and we put the bidirectional microresonators as the first topic as this two-component system in its original form is directly given by a pair of LLEs. The methodology introduced in this chapter, including derivations as well as mathematical analyses, are serving as the bases for other works. Unlike the unidirectional cavity, the dynamics of counter-rotating waves circulating in the high-finesse microresonator are mapped in an averaged model. The rich features of symmetric and asymmetric resonances have been observed. In particular, we found the discontinuity of the low-intensity homogeneous states along the detuning scan, which strictly forbids the existence of dissipative Kerr soliton. Further study of the blockade effect, i.e., the generation and destruction of solitons, provides the clue for controlling the frequency comb through the intracavity energy. In addition, the theory of instability mode excitations contoured by the tongue-like structures has been demonstrated to be crucial in frequency comb generations.

In the second topic, we first expanded the Kerr frequency comb discussion to the perfect soliton crystals whose spectral lines are separated by multiple integers of FSRs and spatially, they are evenly located in the ring. The relative positions of the solitons with their two neighbours can be equal and unequal, resulting in the atomic and molecular unit cells. The on-demand positioning of solitons controls the coupling strengths between molecular crystals supported by dispersive waves. We have numerically observed the topological bands formation similar to the well-known one-dimensional SSH lattice. The band structures are efficiently computed utilising the Bloch theorem. The non-trivial geometric phase has been demonstrated by taking the Berry phase formula. Moreover, the geometric phase is further confirmed in the Wannier representation. The edge states have been found by introducing proper defects into the periodic ring. When we remove an odd number of solitons, it induces the chirality between the left and right sides of the vacancy centre.

Beyond the Kerr microresonators, the OPO frequency comb generated in $\chi^{(2)}$ resonator has been studied numerically. This specific work aims to find the mid-IR combs in $CdSiP_2$ medium. We first introduced the model for the $\chi^{(2)}$ resonator, and the subsequent analyses to track the stationary solutions have been depicted in detail. The staggered spectra, distinctive from the ordinary ones, have been confirmed widely exist in a large range of offset ε, moreover, this observation has been identified with the experimental results from our colleagues for the first time. Lastly, we report the soliton combs whose spectra span over 70 FSRs with purely $\chi^{(2)}$ nonlinearity. It raises our interest to figure out the mechanism, especially to motivate further studies in experiments.

Appendix A

Numerical methods and stability analysis

The nonlinear partial differential equations (like LLE introduced above) are often very challenging to be solved analytically, except some special conditions are applied, for example, $\partial_\theta = 0, \partial_t = 0$. Numerical approaches introduced in this section are significant for modelling simulations throughout this thesis. Stability analysis, on the other hand, can provide us significant information of how the system will react to the perturbations.

A.0.1 Newton-Raphson method and Jacobian

Newton-Raphson method is a common numerical approach to searching stationary solutions for differential equations. By truncating the Taylor expansion to the first derivative:

$$f(x_{n+1}) \approx f(x_n) + f'(x_n)(x_{n+1} - x_n) = 0 \tag{A.1}$$

the iteration seeking for convergence follows:

$$x_{n+1} = x_n - \frac{f(x_n)}{f'(x_n)} \tag{A.2}$$

The iterations will stop when root x_n satisfies $f(x_n) = 0$. Sometimes the convergence is challenging due to the inaccurate initial conditions. Estimation of the inputs should be considered carefully and a good ansatz is required.

In the following, we give the example of finding the Jacobian of the model in Chapter 2. Jacobian is important in numerical analysis, especially for the Newton-Raphson method [1] and perturbation theory [2]. To find the Jacobian in this system, we assume a pair of solutions in forms of $\psi_+ = A + a, \psi_- = B + b$, where A and B are stationary solutions, $a = a(\theta, t)$ and

$b = b(\theta,t)$ are perturbations depend on time t and space θ. The following process presents the substitution in ψ_+ component:

$$i\partial_t(A+a) = \delta_+(A+a) - \frac{1}{2}D_2\partial_\theta^2(A+a) - \gamma|(A+a)|^2(A+a) \\ -i\frac{1}{2}\kappa((A+a) - \mathscr{H}_+) - \frac{\gamma}{\pi}(A+a)\int_0^{2\pi}|(B+b)|^2 d\theta'. \tag{A.3}$$

The nonlinear parts are given in detail:

$$|(A+a)|^2(A+a) = |A|^2A + |A|^2a + A^2a^* + |A|^2a = 2|A|^2a + A^2a^*$$
$$(A+a)\int_0^{2\pi}|(B+b)|^2 d\theta' = A\int_0^{2\pi}|B|^2 d\theta' + A\int_0^{2\pi}Bb^* d\theta' + A\int_0^{2\pi}B^*b d\theta' + a\int_0^{2\pi}|B|^2 d\theta'$$

The above equations are subjected to:

$$i\partial_t a = \delta_+ a - \frac{1}{2}D_2\partial_\theta^2 a - 2\gamma|A|^2a - \gamma A^2a^* - i\frac{1}{2}\kappa a - \frac{\gamma}{\pi}a\int_0^{2\pi}|B|^2 d\theta' \\ -\frac{\gamma}{\pi}A\int_0^{2\pi}Bb^* d\theta' - \frac{\gamma}{\pi}A\int_0^{2\pi}B^*b d\theta'. \tag{A.4}$$

Note the conjugation sign in nonlinear part, in order to have the form in matrix, the complex conjugation is applied to both sides:

$$i\partial_t a^* = -\delta_+ a^* + \frac{1}{2}D_2\partial_\theta^2 a^* + 2\gamma|A|^2a^* + \gamma A^{2*}a - i\frac{1}{2}\kappa a^* + \frac{\gamma}{\pi}a^*\int_0^{2\pi}|B|^2 d\theta' \\ +\frac{\gamma}{\pi}A^*\int_0^{2\pi}B^*b d\theta' + \frac{\gamma}{\pi}A^*\int_0^{2\pi}Bb^* d\theta'. \tag{A.5}$$

Take the same approach, we have a pair of equations for ψ_- component:

$$i\partial_t b = \delta_- b - \frac{1}{2}D_2\partial_\theta^2 b - 2\gamma|B|^2b - \gamma B^2b^* - i\frac{1}{2}\kappa b - \frac{\gamma}{\pi}b\int_0^{2\pi}|A|^2 d\theta' \\ -\frac{\gamma}{\pi}B\int_0^{2\pi}Aa^* d\theta' - \frac{\gamma}{\pi}B\int_0^{2\pi}A^*a d\theta'. \tag{A.6}$$

$$i\partial_t b^* = -\delta_- b^* + \frac{1}{2}D_2\partial_\theta^2 b^* + 2\gamma|B|^2 b^* + \gamma B^{2*} b - i\frac{1}{2}\kappa b^* + \frac{\gamma}{\pi}b^*\int_0^{2\pi}|A|^2 d\theta' + \frac{\gamma}{\pi}B^*\int_0^{2\pi}A^* a d\theta' + \frac{\gamma}{\pi}B^*\int_0^{2\pi}A a^* d\theta'. \tag{A.7}$$

The variables in the first raw can be easily extracted, and the discretization should be applied to the second row of the nonlinear terms: for instance, we define subscript 'j' in order to mark the index j for the variable spanning from index 1 to n (n is the total discretization points). With this notation, we have the following:

$$i\partial_t a_j = \delta_+ a_j - \frac{1}{2}D_2\partial_\theta^2 a_j - 2\gamma|A_j|^2 a_j - \gamma A_j^2 a_j^* - i\frac{1}{2}\kappa a_j - \frac{\gamma}{\pi}a_j\int_0^{2\pi}|B|^2 d\theta' - \frac{\gamma}{\pi}A_j\int_0^{2\pi}Bb^* d\theta' - \frac{\gamma}{\pi}A_j\int_0^{2\pi}B^* b d\theta'. \tag{A.8}$$

$$A_j\int_0^{2\pi}Bb^* d\theta' = A_j d\theta\sum_{n=1}^{N}(B_1 b_1^* + B_2 b_2^* + B_3 b_3^* + ... + B_j b_j^* + ... + B_n b_n^*) \tag{A.9}$$

Arrange them into matrix:

$$i\partial_t\begin{bmatrix} a \\ a^* \\ b \\ b^* \end{bmatrix} = \begin{bmatrix} \Delta_a - i\frac{\kappa}{2} & -\gamma A^2 & -d\theta\frac{\gamma}{\pi}M_{13} & -d\theta\frac{\gamma}{\pi}M_{14} \\ \gamma A^{2*} & -\Delta_a - i\frac{\kappa}{2} & d\theta\frac{\gamma}{\pi}M_{23} & d\theta\frac{\gamma}{\pi}M_{24} \\ -d\theta\frac{\gamma}{\pi}M_{31} & -d\theta\frac{\gamma}{\pi}M_{32} & \Delta_b - i\frac{\kappa}{2} & -\gamma B^2 \\ d\theta\frac{\gamma}{\pi}M_{41} & d\theta\frac{\gamma}{\pi}M_{42} & \gamma B^{2*} & -\Delta_b - i\frac{\kappa}{2} \end{bmatrix}\begin{bmatrix} a \\ a^* \\ b \\ b^* \end{bmatrix} \tag{A.10}$$

where $\Delta_a = \delta_+ - \frac{1}{2}D_2\partial_\theta^2 - 2\gamma|A|^2 - \frac{\gamma}{\pi}\int_0^{2\pi}|B|^2 d\theta'$, $\Delta_b = \delta_- - \frac{1}{2}D_2\partial_\theta^2 - 2\gamma|B|^2 - \frac{\gamma}{\pi}\int_0^{2\pi}|A|^2 d\theta'$.

a, a^*, b, b^* are column $N\times 1$ vector, thus, the size of M is $4N\times 4N$ and each element inside M is $N\times N$ matrix. $M_{11,22,33,44}$ and $M_{12,21,34,43}$ should be $N\times N$ diagonal matrix (apart from the second derivative). The expansion of $M_{13,14,23,24,31,32,41,42}$ will be:

$$M_{13}b = \begin{bmatrix} A_1B_1^* & A_1B_2^* & \dots & A_1B_N^* \\ A_2B_1^* & A_2B_2^* & \dots & A_2B_N^* \\ \vdots & \vdots & \ddots & \vdots \\ A_NB_1^* & A_NB_1^* & \dots & A_NB_N^* \end{bmatrix} \begin{bmatrix} b_1 \\ b_2 \\ \vdots \\ b_N \end{bmatrix}; M_{14}b^* = \begin{bmatrix} A_1B_1 & A_1B_2 & \dots & A_1B_N \\ A_2B_1 & A_2B_2 & \dots & A_2B_N \\ \vdots & \vdots & \ddots & \vdots \\ A_NB_1 & A_NB_2 & \dots & A_NB_N \end{bmatrix} \begin{bmatrix} b_1^* \\ b_2^* \\ \vdots \\ b_N^* \end{bmatrix} \tag{A.11}$$

$$M_{23}b = \begin{bmatrix} A_1^*B_1^* & A_1^*B_2^* & \dots & A_1^*B_N^* \\ A_2^*B_1^* & A_2^*B_2^* & \dots & A_2^*B_N^* \\ \vdots & \vdots & \ddots & \vdots \\ A_N^*B_1^* & A_N^*B_2^* & \dots & A_N^*B_N^* \end{bmatrix} \begin{bmatrix} b_1 \\ b_2 \\ \vdots \\ b_N \end{bmatrix}; M_{24}b^* = \begin{bmatrix} A_1^*B_1 & A_1^*B_2 & \dots & A_1^*B_N \\ A_2^*B_1 & A_2^*B_2 & \dots & A_2^*B_N \\ \vdots & \vdots & \ddots & \vdots \\ A_N^*B_1 & A_N^*B_2 & \dots & A_N^*B_N \end{bmatrix} \begin{bmatrix} b_1^* \\ b_2^* \\ \vdots \\ b_N^* \end{bmatrix} \tag{A.12}$$

$$M_{31}a = \begin{bmatrix} B_1A_1^* & B_1A_2^* & \dots & B_1A_N^* \\ B_2A_1^* & B_2A_2^* & \dots & B_2A_N^* \\ \vdots & \vdots & \ddots & \vdots \\ B_NA_1^* & B_NA_2^* & \dots & B_NA_N^* \end{bmatrix} \begin{bmatrix} a_1 \\ a_2 \\ \vdots \\ a_N \end{bmatrix}; M_{32}a^* = \begin{bmatrix} B_1A_1 & B_1A_2 & \dots & B_1A_N \\ B_2A_1 & B_2A_2 & \dots & B_2A_N \\ \vdots & \vdots & \ddots & \vdots \\ B_NA_1 & B_NA_2 & \dots & B_NA_N \end{bmatrix} \begin{bmatrix} a_1^* \\ a_2^* \\ \vdots \\ a_N^* \end{bmatrix}; \tag{A.13}$$

$$M_{41}a = \begin{bmatrix} B_1^*A_1^* & B_1^*A_2^* & \dots & B_1^*A_N^* \\ B_2^*A_1^* & B_2^*A_2^* & \dots & B_2^*A_N^* \\ \vdots & \vdots & \ddots & \vdots \\ B_N^*A_1^* & B_N^*A_2^* & \dots & B_N^*A_N^* \end{bmatrix} \begin{bmatrix} a_1 \\ a_2 \\ \vdots \\ a_N \end{bmatrix}; M_{42}a^* = \begin{bmatrix} B_1^*A_1 & B_1^*A_2 & \dots & B_1^*A_N \\ B_2^*A_1 & B_2^*A_2 & \dots & B_2^*A_N \\ \vdots & \vdots & \ddots & \vdots \\ B_N^*A_1 & B_N^*A_2 & \dots & B_N^*A_N \end{bmatrix} \begin{bmatrix} a_1^* \\ a_2^* \\ \vdots \\ a_N^* \end{bmatrix}; \tag{A.14}$$

Define $\vec{\alpha} = [a, a^*, b, b^*]^T$, the above matrices are arranged below:

$$\partial_t \vec{\alpha} = -i\hat{M}\vec{\alpha}. \tag{A.15}$$

The eigenvalue λ of the matrix $(-i\hat{M})$ should be discussed by real and imaginary parts. The real part features the exponential growth of perturbations with time. Therefore the positive real part is in relation to the instability growth rate in time, whereas the negative real λ implies the stabilization. The imaginary part of λ shows the oscillating frequency of the

wave impacted by the perturbations when the dynamical wave propagation is considered in the time domain.

A.0.2 Modulation instability

The modulation instability is crucial when considering the frequency comb generation pumped by continuous wave lasers. The cascaded process starts with two photons at pump frequency breaking into two sideband modes under momentum conservation. In the following, we present the analysis in the coupled-mode representation for this process:

$$i(\partial_t + i\delta + i\frac{D_2}{2}\mu^2)A_\mu^+ + i\tfrac{1}{2}\kappa\left(A_\mu^+ - \hat{\delta}_{\mu,0}\mathscr{H}_+\right) \tag{A.16}$$
$$= -\gamma \sum_{\mu_1\mu_2\mu_3} \delta_{\mu_1+\mu_2,\mu_3+\mu} A_{\mu_1}^+ A_{\mu_2}^+ A_{\mu_3}^{+*} - 2\gamma \sum_{\mu_1\mu_2} \delta_{\mu_1,\mu} |A_{\mu_2}^-|^2 A_{\mu_1}^+,$$

$$i(\partial_t + i\delta + +i\frac{D_2}{2}\mu^2)A_\mu^- + i\tfrac{1}{2}\kappa\left(A_\mu^- - \hat{\delta}_{\mu,0}\mathscr{H}_-\right) \tag{A.17}$$
$$= -\gamma \sum_{\mu_1\mu_2\mu_3} \delta_{\mu_1+\mu_2,\mu_3+\mu} A_{\mu_1}^- A_{\mu_2}^- A_{\mu_3}^{-*} - 2\gamma \sum_{\mu_1\mu_2} \delta_{\mu_1,\mu} |A_{\mu_2}^+|^2 A_{\mu_1}^-$$

Assume the pump mode 0 is perturbed by a pair of sideband photons at modes $\mu, -\mu$:

$$
\begin{aligned}
i\partial_t A_0^+ &= \delta A_0^+ - i\frac{\kappa}{2}A_0^+ + i\frac{\kappa}{2}\mathscr{H}_+ \\
&- \gamma(A_0^+A_0^+A_0^{+*} + A_0^+A_\mu^+A_\mu^{+*} + A_0^+A_{-\mu}^+A_{-\mu}^{+*} + A_\mu^+A_{-\mu}^+A_0^{+*} + A_\mu^+A_0^+A_\mu^{+*} \\
&+ A_{-\mu}^+A_0^+A_{-\mu}^{+*} + A_{-\mu}^+A_\mu^+A_0^{+*}) \\
&- 2\gamma(|A_0^-|^2A_0^+ + |A_\mu^-|^2A_0^+ + |A_{-\mu}^-|^2A_0^+)
\end{aligned}
\tag{A.18}
$$

$$
\begin{aligned}
i\partial_t A_\mu^+ &= \delta A_\mu^+ - i\frac{\kappa}{2}A_\mu^+ + \frac{1}{2}D_2\mu^2A_\mu^+ \\
&- \gamma(A_0^+A_0^+A_{-\mu}^{+*} + A_0^+A_\mu^+A_0^{+*} + A_\mu^+A_0^+A_0^{+*} + A_\mu^+A_\mu^+A_\mu^{+*} + A_\mu^+A_{-\mu}^+A_{-\mu}^{+*} + A_{-\mu}^+A_\mu^+A_{-\mu}^{+*}) \\
&- 2\gamma(|A_0^-|^2A_\mu^+ + |A_\mu^-|^2A_\mu^+ + |A_{-\mu}^-|^2A_\mu^+)
\end{aligned}
\tag{A.19}
$$

$$
\begin{aligned}
i\partial_t A_{-\mu}^+ &= \delta A_{-\mu}^+ - i\frac{\kappa}{2}A_{-\mu}^+ + \frac{1}{2}D_2\mu^2A_{-\mu}^+ \\
&- \gamma(A_0^+A_0^+A_\mu^{+*} + A_0^+A_{-\mu}^+A_0^{+*} + A_\mu^+A_{-\mu}^+A_\mu^{+*} + A_{-\mu}^+A_0^+A_0^{+*} + A_{-\mu}^+A_\mu^+A_\mu^{+*} + A_{-\mu}^+A_{-\mu}^+A_{-\mu}^{+*}) \\
&- 2\gamma(|A_0^-|^2A_{-\mu}^+ + |A_\mu^-|^2A_{-\mu}^+ + |A_{-\mu}^-|^2A_{-\mu}^+)
\end{aligned}
\tag{A.20}
$$

$$
\begin{aligned}
i\partial_t A_0^- &= \delta A_0^- - i\frac{\kappa}{2}A_0^- + i\frac{\kappa}{2}\mathscr{H}_- \\
&- \gamma(A_0^-A_0^-A_0^{-*} + A_0^-A_\mu^-A_\mu^{-*} + A_0^-A_{-\mu}^-A_{-\mu}^{-*} + A_\mu^-A_{-\mu}^-A_0^{-*} + A_\mu^-A_0^-A_\mu^{-*} + \\
&A_{-\mu}^-A_0^-A_{-\mu}^{-*} + A_{-\mu}^-A_\mu^-A_0^{-*}) \\
&- 2\gamma(|A_0^+|^2A_0^- + |A_\mu^+|^2A_0^- + |A_{-\mu}^+|^2A_0^-)
\end{aligned}
\tag{A.21}
$$

$$
\begin{aligned}
i\partial_t A_\mu^- &= \delta A_\mu^- - i\frac{\kappa}{2}A_\mu^- + \frac{1}{2}D_2\mu^2A_\mu^- \\
&- \gamma(A_0^-A_0^-A_{-\mu}^{-*} + A_0^-A_\mu^-A_0^{-*} + A_\mu^-A_0^-A_0^{-*} + A_\mu^-A_\mu^-A_\mu^{-*} + A_\mu^-A_{-\mu}^-A_{-\mu}^{-*} + A_{-\mu}^-A_\mu^-A_{-\mu}^{-*}) \\
&- 2\gamma(|A_0^+|^2A_\mu^- + |A_\mu^+|^2A_\mu^- + |A_{-\mu}^+|^2A_\mu^-)
\end{aligned}
\tag{A.22}
$$

$$
\begin{aligned}
i\partial_t A_{-\mu}^- &= \delta A_{-\mu}^- - i\frac{\kappa}{2}A_{-\mu}^- + \frac{1}{2}D_2\mu^2A_{-\mu}^- \\
&- \gamma(A_0^-A_0^-A_\mu^{-*} + A_0^-A_{-\mu}^-A_0^{-*} + A_\mu^-A_{-\mu}^-A_\mu^{-*} + A_{-\mu}^-A_0^-A_0^{-*} + A_{-\mu}^-A_\mu^-A_\mu^{-*} + A_{-\mu}^-A_{-\mu}^-A_{-\mu}^{-*}) \\
&- 2\gamma(|A_0^+|^2A_{-\mu}^- + |A_\mu^+|^2A_{-\mu}^- + |A_{-\mu}^+|^2A_{-\mu}^-)
\end{aligned}
\tag{A.23}
$$

Keep only the first order of perturbation from side bands number $\pm\mu$:

$$\begin{aligned} i\partial_t A_0^+ &= \delta A_0^+ - i\frac{\kappa}{2}A_0^+ + i\frac{\kappa}{2}\mathscr{H}_+ \\ &- \gamma(A_0^+ A_0^+ A_0^{+*}) \\ &- 2\gamma(|A_0^-|^2 A_0^+) \end{aligned} \tag{A.24}$$

$$\begin{aligned} i\partial_t A_\mu^+ &= \delta A_\mu^+ - i\frac{\kappa}{2}A_\mu^+ + \frac{1}{2}D_2\mu^2 A_\mu^+ \\ &- \gamma(A_0^+ A_0^+ A_{-\mu}^{+*} + A_0^+ A_\mu^+ A_0^{+*} + A_\mu^+ A_0^+ A_0^{+*}) \\ &- 2\gamma(|A_0^-|^2 A_\mu^+) \end{aligned} \tag{A.25}$$

$$\begin{aligned} i\partial_t A_{-\mu}^+ &= \delta A_{-\mu}^+ - i\frac{\kappa}{2}A_{-\mu}^+ + \frac{1}{2}D_2\mu^2 A_{-\mu}^+ \\ &- \gamma(A_0^+ A_0^+ A_\mu^{+*} + A_0^+ A_{-\mu}^+ A_0^{+*} + A_{-\mu}^+ A_0^+ A_0^{+*}) \\ &- 2\gamma(|A_0^-|^2 A_{-\mu}^+) \end{aligned} \tag{A.26}$$

$$\begin{aligned} i\partial_t A_0^- &= \delta A_0^- - i\frac{\kappa}{2}A_0^- + i\frac{\kappa}{2}\mathscr{H}_- \\ &- \gamma(A_0^- A_0^- A_0^{-*}) \\ &- 2\gamma(|A_0^+|^2 A_0^-) \end{aligned} \tag{A.27}$$

$$\begin{aligned} i\partial_t A_\mu^- &= \delta A_\mu^- - i\frac{\kappa}{2}A_\mu^- + \frac{1}{2}D_2\mu^2 A_\mu^- \\ &- \gamma(A_0^- A_0^- A_{-\mu}^{-*} + A_0^- A_\mu^- A_0^{-*} + A_\mu^- A_0^- A_0^{-*}) \\ &- 2\gamma(|A_0^+|^2 A_\mu^-) \end{aligned} \tag{A.28}$$

$$\begin{aligned} i\partial_t A_{-\mu}^- &= \delta A_{-\mu}^- - i\frac{\kappa}{2}A_{-\mu}^- + \frac{1}{2}D_2\mu^2 A_{-\mu}^- \\ &- \gamma(A_0^- A_0^- A_\mu^{-*} + A_0^- A_{-\mu}^- A_0^{-*} + A_{-\mu}^- A_0^- A_0^{-*}) \\ &- 2\gamma(|A_0^+|^2 A_{-\mu}^-) \end{aligned} \tag{A.29}$$

The matrix for the MI of pump mode is shown below by substituting $A_0^\pm = A_0^\pm + \rho_\pm$:

$$i\partial_t \begin{bmatrix} \rho_+ \\ \rho_+^* \\ \rho_- \\ \rho_-^* \end{bmatrix} = \begin{bmatrix} \Delta - i\frac{\kappa}{2} & -\gamma(A_0^+)^2 & -2\gamma A_0^+ A_0^{-*} & -2\gamma A_0^+ A_0^- \\ \gamma(A_0^{+*})^2 & -\Delta - i\frac{\kappa}{2} & 2\gamma A_0^{+*} A_0^{-*} & 2\gamma A_0^{+*} A_0^- \\ -2\gamma A_0^{+*} A_0^- & -2\gamma A_0^+ A_0^- & \Delta - i\frac{\kappa}{2} & -\gamma(A_0^-)^2 \\ 2\gamma A_0^{+*} A_0^{-*} & 2\gamma A_0^+ A_0^{-*} & \gamma(A_0^{-*})^2 & -\Delta - i\frac{\kappa}{2} \end{bmatrix} \begin{bmatrix} \rho_+ \\ \rho_+^* \\ \rho_- \\ \rho_-^* \end{bmatrix} \tag{A.30}$$

where $\Delta = \delta + \frac{1}{2}D_2\mu^2 - 2\gamma(|A_0^+|^2 + |A_0^-|^2)$. MI for the sidebands modes ($\mu \neq 0$) are:

$$i\partial_t \begin{bmatrix} A_\mu^+ \\ A_{-\mu}^{+*} \\ A_\mu^- \\ A_{-\mu}^{-*} \end{bmatrix} = \begin{bmatrix} \Delta - i\frac{\kappa}{2} & -\gamma(A_0^+)^2 & 0 & 0 \\ \gamma(A_0^{+*})^2 & -\Delta - i\frac{\kappa}{2} & 0 & 0 \\ 0 & 0 & \Delta - i\frac{\kappa}{2} & -\gamma(A_0^-)^2 \\ 0 & 0 & \gamma(A_0^{-*})^2 & -\Delta - i\frac{\kappa}{2} \end{bmatrix} \begin{bmatrix} A_\mu^+ \\ A_{-\mu}^{+*} \\ A_\mu^- \\ A_{-\mu}^{-*} \end{bmatrix} \tag{A.31}$$

The eigenvalues can be analytical obtained:

$$\lambda_{A_\mu^+, A_{-\mu}^{+*}} = -\frac{\kappa}{2} \pm \sqrt{\gamma^2|A_0^+|^4 - \Delta^2} \qquad \lambda_{A_\mu^-, A_{-\mu}^{-*}} = -\frac{\kappa}{2} \pm \sqrt{\gamma^2|A_0^-|^4 - \Delta^2}$$

This section provides the essential way to find the Jacobian of the dual-component system and also the way targeting at the stability. Similar approaches have been used in the whole thesis.

A.0.3 References

[1] E. Süli, D. Mayers, An Introduction to Numerical Analysis. Cambridge University Press, (2003).

[2] M. H. Holmes, Introduction to perturbation methods (2nd ed.). New York: Springer. ISBN 978-1-4614-5477-9 (2013).

Appendix B

Publications

[1] Z. Fan, D. N. Puzyrev, D. V. Skryabin, Soliton metacrystals: topology and chirality, Commun. Phys. 5, 248 (2022).

[2] N. Amiune, Z. Fan, V. V. Pankratov, D. N. Puzyrev, D. V. Skryabin, K. T. Zawilski, P. G. Schunemann, I. Breunig, Mid-infrared frequency combs and staggered spectral patterns in $\chi^{(2)}$ microresonators, arXiv:2205.12776 (under review).

[3] D. V. Skryabin, Z. Fan, A. Villois, D. N. Puzyrev, Threshold of complexity and Arnold tongues in Kerr-ring microresonators, Phys. Rev. A, 103 (1) L011502 (2021).

[4] Z. Fan, D. V. Skryabin, Controlling microresonator solitons with the counter-propagating pump, Photonics 8 (7) 239 (2021).

[5] Z. Fan, D. V. Skryabin, Soliton blockade in bidirectional microresonators, Opt. Lett., 45 (23) 6446 (2020).

[6] Z. Fan, D. N. Puzyrev, M. Johansson, D. V. Skryabin, Soliton blockade and symmetry breaking in microresonators CLEO: QELS_Fundamental Science, JW1A. 6 (2021).

[7] D. N. Puzyrev, Z. Fan, A. Villois, D. V. Skryabin, Four-wave mixing and Arnold tongues in high finesse Kerr ring microresonators, CLEO/Europe-EQEC, IEEE (2021).

[8] Z. Fan, D. V. Skryabin, Soliton blockade in bi-directional Kerr microresonators, CLEO/Europe-EQEC, IEEE (2021).